

1 SEARCH FOR PRODUCTION OF A HIGGS BOSON AND A SINGLE TOP
2 QUARK IN MULTILEPTON FINAL STATES IN pp COLLISIONS AT $\sqrt{s} = 13$
3 TeV.

4 by

5 Jose Andres Monroy MontaÑez

6 A DISSERTATION

7 Presented to the Faculty of

8 The Graduate College at the University of Nebraska

In Partial Fulfilment of Requirements

10 For the Degree of Doctor of Philosophy

11 Major: Physics and Astronomy

12 Under the Supervision of Kenneth Bloom and Aaron Dominguez

13 Lincoln, Nebraska

14 July, 2018

15 SEARCH FOR PRODUCTION OF A HIGGS BOSON AND A SINGLE TOP
16 QUARK IN MULTILEPTON FINAL STATES IN pp COLLISIONS AT $\sqrt{s} = 13$
17 TeV.

18 Jose Andres Monroy Montañez, Ph.D.

19 University of Nebraska, 2018

20 Adviser: Kenneth Bloom and Aaron Dominguez

²¹ Table of Contents

²² Table of Contents	iii
²³ List of Figures	vi
²⁴ List of Tables	ix
²⁵ 1 INTRODUCTION	1
²⁶ 2 Theoretical approach	2
27 2.1 Introduction	2
28 2.2 Standard model of particle physics	3
29 2.2.1 Fermions	5
30 2.2.1.1 Leptons	6
31 2.2.1.2 Quarks	8
32 2.2.2 Fundamental interactions	12
33 2.2.3 Gauge bosons	18
34 2.3 Electroweak unification and the Higgs mechanism	20
35 2.3.1 Spontaneous symmetry breaking (SSB)	28
36 2.3.2 Higgs mechanism	32
37 2.3.3 Masses of the gauge bosons	34

38	2.3.4	Masses of the fermions	35
39	2.3.5	The Higgs field	36
40	2.3.6	Production of Higgs bosons at LHC	37
41	2.3.7	Higgs boson decay channels	41
42	2.4	Associated production of a Higgs boson and a single Top quark.	42
43	2.5	The CP-mixing in tH processes	47
44	2.6	Experimantal status of the anomalous Higg-fermion coupling.	51
45	3	The CMS experiment at the LHC	53
46	3.1	Introduction	53
47	3.2	The LHC	54
48	3.3	The CMS experiment	63
49	3.3.1	Coordinate system	65
50	3.3.2	Pixels detector	67
51	3.3.3	Silicon strip tracker	69
52	3.3.4	Electromagnetic calorimeter	70
53	3.3.5	Hadronic calorimeter	72
54	3.3.6	Superconducting solenoid magnet	73
55	3.3.7	Muon system	75
56	3.3.8	CMS trigger system	76
57	3.3.9	CMS computing	78
58	4	Event generation, simulation and reconstruction	82
59	4.1	Event generation	83
60	4.2	Monte Carlo Event Generators.	87
61	4.3	CMS detector simulation.	88
62	4.4	Event reconstruction.	90

63	4.5	MVA methods, NN, BDT, boosting, overtraining, variable ranking	91
64	4.6	statistical inference, likelihood parametrization	91
65	4.7	nuisance paraeters	91
66	4.8	exclusion limits	91
67	4.9	asymptotic limits	91
68	5	Search for production of a Higgs boson and a single top quark in multilepton final states in pp collisions at $\sqrt{s} = 13$ TeV	92
70	5.1	Introduction	92
71	5.2	Data and MC Samples	94
72	5.2.1	Full 2016 dataset and MC samples	94
73	5.2.2	Triggers	97
74	5.2.2.1	Trigger efficiency scale factors	97
75	5.3	Object Identification and event selection	98
76	5.3.1	Jets and b tagging	98
77	5.3.2	Lepton selection	99
78	5.3.3	Lepton selection efficiency	100
79	5.4	Background predictions	101
80	5.5	Signal discrimination	102
81	5.5.1	Classifiers response	106
82	5.6	Additional discriminating variables	109
83	Bibliography		110
84	References		112

⁸⁵ List of Figures

86	2.1	Standard model of particle physics.	4
87	2.2	Transformations between quarks	12
88	2.3	Fundamental interactions in nature.	13
89	2.4	SM interactions diagrams	14
90	2.5	Neutral current processes	21
91	2.6	Spontaneous symmetry breaking mechanism	28
92	2.7	SSB Potential form	29
93	2.8	Potential for complex scalar field	30
94	2.9	SSB mechanism for complex scalar field	31
95	2.10	Proton-Proton collision	38
96	2.11	Higgs boson production mechanism Feynman diagrams	39
97	2.12	Higgs boson production cross section and decay branching ratios	40
98	2.13	Associated Higgs boson production mechanism Feynman diagrams	43
99	2.14	Cross section for tHq process as a function of κ_t	45
100	2.15	Cross section for tHW process as a function of κ_{Htt}	46
101	2.16	NLO cross section for tX_0 and $t\bar{t}X_0$.	49
102	2.17	NLO cross section for tWX_0 , $t\bar{t}X_0$.	50

103	2.18 Two dimentional κ_t - κ_V plot of the coupling modifiers. ATLAS and CMS 104 combination.	51
105	3.1 CERN accelerator complex	54
106	3.2 LHC protons source. First acceleration stage.	55
107	3.3 The LINAC2 accelerating system at CERN.	56
108	3.4 LHC layout and RF cavities module.	57
109	3.5 LHC dipole magnet.	59
110	3.6 Integrated luminosity delivered by LHC and recorded by CMS during 2016	61
111	3.7 LHC interaction points	62
112	3.8 Multiple pp collision bunch crossing at CMS.	64
113	3.9 Layout of the CMS detector	65
114	3.10 CMS detector coordinate system	66
115	3.11 CMS pixel detector schematic view.	68
116	3.12 SST Schematic view.	69
117	3.13 CMS ECAL schematic view	71
118	3.14 CMS HCAL schematic view	72
119	3.15 CMS solenoid magnet	74
120	3.16 CMS Muon system schematic view	75
121	3.17 CMS Level-1 trigger architecture	77
122	3.18 WLCG structure	78
123	3.19 Data flow from CMS detector through hardware Tiers	81
124	4.1 Event generation process.	83
125	5.1 The two leading-order diagrams of tHq production.	93
126	5.2 Input variables to the BDT for signal discrimination normalized.	103

127	5.3	Input variables to the BDT for signal discrimination not normalized.	105
128	5.4	BDT inputs as seen by TMVA against $t\bar{t}$.	106
129	5.5	BDT inputs as seen by TMVA against $t\bar{t}V$.	107
130	5.6	Correlation matrices for the input variables in the TMVA.	108
131	5.7	MVA classifiers performance.	108
132	5.8	Additional discriminating variables distributions.	110

¹³³ List of Tables

134	2.1	Fermions of the SM.	5
135	2.2	Fermion masses.	6
136	2.3	Leptons properties.	9
137	2.4	Quarks properties.	9
138	2.5	Fermion weak isospin and weak hypercharge multiplets.	11
139	2.6	Fundamental interactions features.	15
140	2.7	SM gauge bosons.	19
141	2.8	Higgs boson properties.	37
142	2.9	Predicted branching ratios for a SM Higgs boson with $m_H = 125 \text{ GeV}/c^2$	42
143	2.10	Predicted SM cross sections for tH production at $\sqrt{s} = 13 \text{ TeV}$	44
144	2.11	Predicted enhancement of the tHq and tHW cross sections at LHC	47
145	5.1	Signal samples and their cross section and branching fraction.	94
146	5.2	κ_V and κ_t combinations.	95
147	5.3	List of background samples used in this analysis (CMSSW 80X).	96
148	5.4	Leading-order $t\bar{t}W$ and $t\bar{t}Z$ samples used in the signal BDT training. . . .	96
149	5.5	Table of high-level triggers that we consider in the analysis.	97
150	5.6	Trigger efficiency scale factors and associated uncertainties.	98
151	5.7	Requirements on each of the three muon selections.	99

152	5.8 Criteria for each of the three electron selections.	100
153	5.9 MVA input discriminating variables	104
154	5.10 TMVA input variables ranking for BDTA_GRAD method	109
155	5.11 TMVA configuration used in the BDT training.	109
156	5.12 ROC-integral for all the testing cases.	111

¹⁵⁷ Chapter 1

¹⁵⁸ INTRODUCTION

¹⁵⁹ **Chapter 2**

¹⁶⁰ **Theoretical approach**

¹⁶¹ **2.1 Introduction**

¹⁶² The physical description of the universe is a challenge that physicists have faced by
¹⁶³ making theories that refine existing principles and proposing new ones in an attempt
¹⁶⁴ to embrace emerging facts and phenomena.

¹⁶⁵

¹⁶⁶ At the end of 1940s Julian Schwinger [1] and Richard P. Feynman [2], based in the
¹⁶⁷ work of Sin-Itiro Tomonaga [3], developed an electromagnetic theory consistent with
¹⁶⁸ special relativity and quantum mechanics that describes how matter and light inter-
¹⁶⁹ act; the so-called “quantum eletrodynamics” (QED) had born.

¹⁷⁰

¹⁷¹ QED has become the guide in the development of theories that describe the universe.
¹⁷² It was the first example of a quantum field theory (QFT), which is the theoretical
¹⁷³ framework for building quantum mechanical models that describes particles and their
¹⁷⁴ interactions. QFT is composed of a set of mathematical tools that combines classical
¹⁷⁵ fields, special relativity and quantum mechanics, while keeping the quantum point

176 particles and locality ideas.

177 This chapter gives an overview of the standard model of particle physics, starting
 178 with a description of the particles and interactions that compose it, followed by a
 179 description of the electroweak interaction, the Higgs boson and the associated pro-
 180 duction of Higgs boson and a single top quark (tH). The description contained in
 181 this chapter is based on references [4–6].

182 2.2 Standard model of particle physics

183 Particle physics at the fundamental level is modeled in terms of a collection of in-
 184 teracting particles and fields in a theory known as the “standard model of particle
 185 physics (SM)”¹.

186

187 The full picture of the SM is composed of three fields², whose excitations are inter-
 188 preted as particles called mediators or force-carriers; a set of fields, whose excitations
 189 are interpreted as elementary particles, interacting through the exchange of those
 190 mediators and a field that gives the mass to elementary particles. Figure 2.1 shows
 191 an scheme of the SM particles organization. In addition to the particles in the scheme
 192 (but not listed in it), their corresponding anti-particles, with opposite quantum num-
 193 bers, are also part of the picture; some particles are their own anti-particles, like
 194 photon or Higgs, or anti-particle is already listed like in the W^+ and W^- case.

195

196 The mathematical formulation of the SM is based on group theory and the use of
 197 Noether’s theorem [8] which states that for a physical system modeled by a Lagrangian

¹ The formal and complete treatment of the SM is out of the scope of this document, however a plenty of textbooks describing it at several levels are available in the literature. The treatment in references [?] is quite comprehensive and detailed.

² Note that gravitational field is not included in the standard model formulation

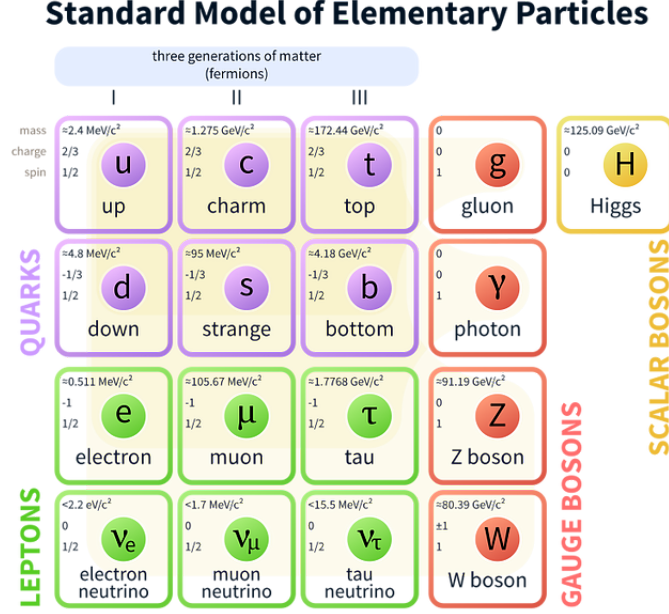


Figure 2.1: Schematic representation of the Standard model of particle physics. SM is a theoretical model intended to describe three of the four fundamental forces of the universe in terms of a set of particles and their interactions. [7].

198 that is invariant under a group of transformations a conservation law is expected. For
 199 instance, a system described by a time-independent Lagrangian is invariant (symmet-
 200 ric) under time changes (transformations) with the total energy conservation law as
 201 the expected conservation law. In QED, the charge operator (Q) is the generator of
 202 the $U(1)$ symmetry which according to the Noether's theorem means that there is a
 203 conserved quantity; this conserved quantity is the electric charge and thus the law
 204 conservation of electric charge is established.

205

206 In the SM, the symmetry group $SU(3)_C \otimes SU(2)_L \otimes U(1)_Y$ describes three of the
 207 four fundamental interactions in nature(see section 2.2.2): strong interaction(SI),
 208 weak interaction(WI) and electromagnetic interactions (EI) in terms of symmetries
 209 associated to physical quantities:

- 210 • Strong: $SU(3)_C$ associated to color charge
- 211 • Weak: $SU(2)_L$ associated to weak isospin and chirality
- 212 • Electromagnetic: $U(1)_Y$ associated to weak hypercharge and electric charge
- 213 It will be shown that the electromagnetic and weak interactions are combined in
 214 the so-called electroweak interaction where chirality, hypercharge, weak isospin and
 215 electric charge are the central concepts.

216 **2.2.1 Fermions**

217 The basic constituents of the ordinary matter at the lowest level, which form the set
 218 of elementary particles in the SM formulation, are quarks and leptons. All of them
 219 have spin 1/2, therefore they are classified as fermions since they obey Fermi-Dirac
 220 statistics. There are six “flavors” of quarks and three of leptons organized in three
 221 generations, or families, as shown in table 2.1.

222

		Generation		
		1st	2nd	3rd
Leptons	Charged	Electron (e)	Moun(μ)	Tau (τ)
	Neutral	Electron neutrino (ν_e)	Muon neutrino (ν_μ)	Tau neutrino (ν_τ)
Quarks	Up-type	Up (u)	Charm (c)	Top (t)
	Down-type	Down (d)	Strange (s)	Bottom (b)

Table 2.1: Fermions of the SM. There are six flavors of quarks and three of leptons, organized in three generations, or families, composed of two pairs of closely related particles. The close relationship is motivated by the fact that WI between leptons is limited to the members of the same generation; WI between quarks is not limited but greatly favoured, to same generation members.

223

224 There is a mass hierarchy between generations (see table 2.2), where the higher gener-
 225 ation particles decays to the lower one, which can explain why the ordinary matter is

made of particles in the first generation. In the SM, neutrinos are modeled as massless particles so they are not subject to this mass hierarchy; however, today it is known that neutrinos are massive so the hierarchy could be restated. The reason behind this mass hierarchy is one of the most important open questions in particle physics, and it becomes more puzzling when noticing that the mass difference between first and second generation fermions is small compared to the mass difference with respect to the third generation.

Lepton	Mass (MeV/c ²)	Quark	Mass (MeV/c ²)
e	0.51	u	2.2
μ	105.65	c	1.28×10^3
τ	1776.86	t	173.1×10^3
ν_e	Unknown	d	4.7
ν_μ	Unknown	s	96
τ_μ	Unknown	b	4.18×10^3

Table 2.2: Fermion masses [9]. Generations differ by mass in a way that have been interpreted as a masss hierarchy. Approximate values with no uncertainties are used, for comparison purpose.

233

Usually, the second and third generation fermions are produced in high energy processes, like the ones recreated in particle accelerators.

236 2.2.1.1 Leptons

A lepton is an elementary particle that is not subject to the SI. As seen in table 2.1, there are two types of leptons, the charged ones (electron, muon and tau) and the neutral ones (the three neutrinos). The electric charge (Q) is the property that gives leptons the ability to participate in the EI. From the classical point of view, Q plays a central role determining, among others, the strength of the electric field through which the electromagnetic force is exerted. It is clear that neutrinos are not affected

243 by EI because they don't carry electric charge.

244

245 Another feature of the leptons that is fundamental in the mathematical description
246 of the SM is the chirality, which is closely related to spin and helicity. Helicity defines
247 the handedness of a particle by relating its spin and momentum such that if they
248 are parallel then the particle is right-handed; if spin and momentum are antiparallel
249 the particle is said to be left-handed. The study of parity conservation (or viola-
250 tion) in β -decay has shown that only left-handed electrons/neutrinos or right-handed
251 positrons/anti-neutrinos are created [10]; the inclusion of that feature in the theory
252 was achieved by using projection operators for helicity, however, helicity is frame de-
253 pendent for massive particles which makes it not Lorentz invariant and then another
254 related attribute has to be used: *chirality*.

255

256 Chirality is a purely quantum attribute which makes it not so easy to describe in
257 graphical terms but it defines how the wave function of a particle transforms under
258 certain rotations. As with helicity, there are two chiral states, left-handed chiral (L)
259 and right-handed chiral (R). In the highly relativistic limit where $E \approx p \gg m$ helicity
260 and chirality converge, becoming exactly the same for massless particles.

261

262 In the following, when referring to left-handed (right-handed) it will mean left-handed
263 chiral (right-handed chiral). The fundamental fact about chirality is that while EI
264 and SI are not sensitive to chirality, in WI left-handed and right-handed fermions are
265 treated asymmetrically, such that only left handed fermions and right-handed anti-
266 fermions are allowed to couple to WI mediators, which is a violation of parity. The
267 way to translate this statement in a formal mathematical formulation is based on the
268 isospin symmetry group $SU(2)_L$.

269

270 Each generation of leptons is seen as a weak isospin doublet.³ The left-handed charged
 271 lepton and its associated left-handed neutrino are arranged in doublets of weak isospin
 272 T=1/2 while their right-handed partners are singlets:

$$\begin{pmatrix} \nu_l \\ l \end{pmatrix}_L, l_R := \begin{pmatrix} \nu_e \\ e \end{pmatrix}_L, \begin{pmatrix} \nu_\mu \\ \mu \end{pmatrix}_L, \begin{pmatrix} \nu_\tau \\ \tau \end{pmatrix}_L, e_R, \mu_R, \tau_R, \nu_{eR}, \nu_{\mu R}, \nu_{\tau R} \quad (2.1)$$

273 The isospin third component refers to the eigenvalues of the weak isospin operator
 274 which for doublets is $T_3 = \pm 1/2$, while for singlets it is $T_3 = 0$. The physical meaning
 275 of this doublet-singlet arrangement falls in that the WI couples the two particles in
 276 the doublet by exchanging the interaction mediator while the singlet member is not
 277 involved in WI. The main properties of the leptons are summarized in table 2.3.

278

279 Altough all three flavor neutrinos have been observed, their masses remain unknown
 280 and only some estimations have been made [11]. The main reason is that the fla-
 281 vor eigenstates are not the same as the mass eigenstates which implies that when
 282 a neutrino is created its mass state is a linear combination of the three mass eigen-
 283 states and experiments can only probe the squared difference of the masses. The
 284 Pontecorvo-Maki-Nakagawa-Sakata (PMNS) mixing matrix encode the relationship
 285 between flavor and mass eigenstates.

286

287 2.2.1.2 Quarks

288 Quarks are the basic constituents of protons and neutrons. The way quarks join to
 289 form bound states, called “hadrons”, is through the SI. Quarks are affected by all the

³ The weak isospin is an analogy of the isospin symmetry in strong interaction where neutron and proton are affected equally by strong force but differ in their charge.

Lepton	Q(e)	T_3	L_e	L_μ	L_τ	Lifetime (s)
Electron (e)	-1	-1/2	1	0	0	Stable
Electron neutrino(ν_e)	0	1/2	1	0	0	Unknown
Muon (μ)	-1	-1/2	0	1	0	2.19×10^{-6}
Muon neutrino (ν_μ)	0	1/2	0	1	0	Unknown
Tau (τ)	-1	-1/2	0	0	1	290.3×10^{-15}
Tau neutrino (τ_μ)	0	1/2	0	0	1	Unknown

Table 2.3: Leptons properties [9]. Q: electric charge, T_3 : weak isospin. Only left-handed leptons and right-handed anti-leptons participate in the WI. Anti-particles with inverted T_3 , Q and lepton number complete the leptons set but are not listed. Right-handed leptons and left-handed anti-leptons, neither listed, form weak isospin singlets with $T_3 = 0$ and do not take part in the weak interaction.

290 fundamental interactions which means that they carry all the four types of charges:
291 color, electric charge, weak isospin and mass.

Flavor	Q(e)	I_3	T_3	B	C	S	T	B'	Y	Color
Up (u)	2/3	1/2	1/2	1/3	0	0	0	0	1/3	r,b,g
Charm (c)	2/3	0	1/2	1/3	1	0	0	0	4/3	r,b,g
Top(t)	2/3	0	1/2	1/3	0	0	1	0	4/3	r,b,g
Down(d)	-1/3	-1/2	-1/2	1/3	0	0	0	0	1/3	r,b,g
Strange(s)	-1/3	0	-1/2	1/3	0	-1	0	0	-2/3	r,b,g
Bottom(b)	-1/3	0	-1/2	1/3	0	0	0	-1	-2/3	r,b,g

Table 2.4: Quarks properties [9]. Q: electric charge, I_3 : isospin, T_3 : weak isospin, B: baryon number, C: charmness, S: strangeness, T: topness, B' : bottomness, Y: hypercharge. Anti-quarks posses the same mass and spin as quarks but all charges (color, flavor numbers) have opposite sign.

292
293 Table 2.4 summarizes the features of quarks, among which the most particular is
294 their fractional electric charge. Note that fractional charge is not a problem, given
295 that quarks are not found isolated, but serves to explain how composed particles are
296 formed out of two or more valence quarks⁴.

297

⁴ Hadrons can contain an indefinite number of virtual quarks and gluons, known as the quark and gluon sea, but only the valence quarks determine hadrons' quantum numbers.

298 Color charge is the responsible for the SI between quarks and is the symmetry
 299 ($SU(3)_C$) that defines the formalism to describe SI. There are three colors: red (r),
 300 blue(b) and green(g) and their corresponding three anti-colors; thus each quark carries
 301 one color unit while anti-quarks carries one anti-color unit. As said above, quarks are
 302 not allowed to be isolated due to the color confinement effect, therefore their features
 303 have been studied indirectly by observing their bound states created when:

- 304 • one quark with a color charge is attracted by an anti-quark with the correspond-
 305 ing anti-color charge forming a colorless particle called a “meson.”
- 306 • three quarks (anti-quarks) with different color (anti-color) charges are attracted
 307 among them forming a colorless particle called a “baryon(anti-baryon).”

308 In the first version of the quark model (1964), M. Gell-Mann [12] and G. Zweig
 309 [13, 14] developed a consistent way to classify hadrons according to their properties.
 310 Only three quarks (u, d, s) were involved in a scheme in which all baryons have
 311 baryon number $B=1$ and therefore quarks have $B=1/3$; non-baryons have $B=0$. The
 312 scheme organizes baryons in a two-dimensional space ($I_3 - Y$); Y (hypercharge) and I_3
 313 (isospin) are quantum numbers related by the Gell-Mann-Nishijima formula [15, 16]:

$$Q = I_3 + \frac{Y}{2} \quad (2.2)$$

314 where $Y = B + S + C + T + B'$ are the quantum numbers listed in table 2.4. Baryon
 315 number is conserved in SI and EI which means that single quarks cannot be created
 316 but in pairs $q - \bar{q}$.

317

318 There are six quark flavors organized in three generations (see table 2.1) following a
 319 mass hierarchy which, again, implies that higher generations decay to first generation

320 quarks.

	Quarks			T_3	Y_W	Leptons			T_3	Y_W
Doublets	$(\frac{u}{d'})_L$	$(\frac{c}{s'})_L$	$(\frac{t}{b'})_L$	$(\frac{1/2}{-1/2})$	1/3	$(\nu_e)_L$	$(\nu_\mu)_L$	$(\nu_\tau)_L$	$(\frac{1/2}{-1/2})$	-1
Singlets	u_R	c_R	t_R	0	4/3	ν_{eR}	$\nu_{\mu R}$	$\nu_{\tau R}$	0	-2

Table 2.5: Fermion weak isospin and weak hypercharge multiplets. Weak hypercharge is calculated through the Gell-Mann-Nishijima formula 2.2 but using the weak isospin and charge for quarks.

321

322 Isospin doublets of quarks are also defined (see table 2.5) and as for neutrinos, the
 323 mass eigenstates are not the same as the WI eigenstates which means that members of
 324 different quark generations are connected by the WI mediator; thus, up-type quarks
 325 are coupled not to down-type quarks directly but to a superposition of down-type
 326 quarks (q'_d) via WI according to:

$$q'_d = V_{CKM} q_d$$

327

$$\begin{pmatrix} d' \\ s' \\ b' \end{pmatrix} = \begin{pmatrix} V_{ud} & V_{us} & V_{ub} \\ V_{cd} & V_{cs} & V_{cb} \\ V_{td} & V_{ts} & V_{tb} \end{pmatrix} \begin{pmatrix} d \\ s \\ b \end{pmatrix} \quad (2.3)$$

328 where V_{CKM} is known as Cabibbo-Kobayashi-Maskawa (CKM) mixing matrix [17,18].
 329 The weak decays of quarks are represented in the diagram of figure 2.2; again the
 330 CKM matrix plays a central role since it contains the probabilities for the different
 331 quark decay channels, in particular, note that quark decays are greatly favored be-
 332 tween generation members.

333

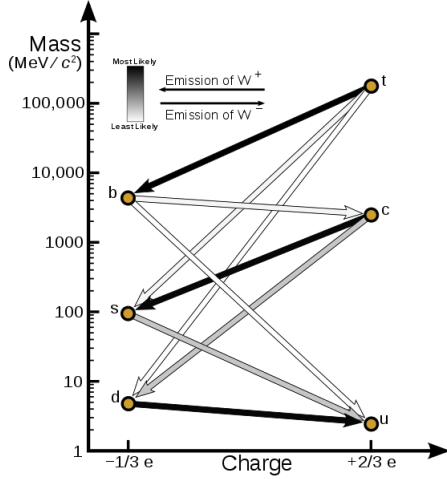


Figure 2.2: Transformations between quarks through the exchange of a WI. Higher generations quarks decay to first generation quarks by emitting a W boson. The arrow color indicates the likelihood of the transition according to the grey scale in the top left side which represent the CKM matrix parameters [19].

334 CKM matrix is a 3×3 unitary matrix parametrized by three mixing angles and
 335 the *CP-mixing phase*; the latter is the parameter responsible for the Charge-Parity
 336 symmetry violation (CP-violation) in the SM. The fact that the b quark decays almost
 337 all the times to a top quark is exploited in this thesis when making the selection of
 338 the signal events by requiring the presence of a jet tagged as a jet coming from a
 339 b quark in the final state. The effect of the *CP-mixing phase* on the cross section of
 340 associated production of Higgs boson and a single top process is also explored in this
 341 thesis.

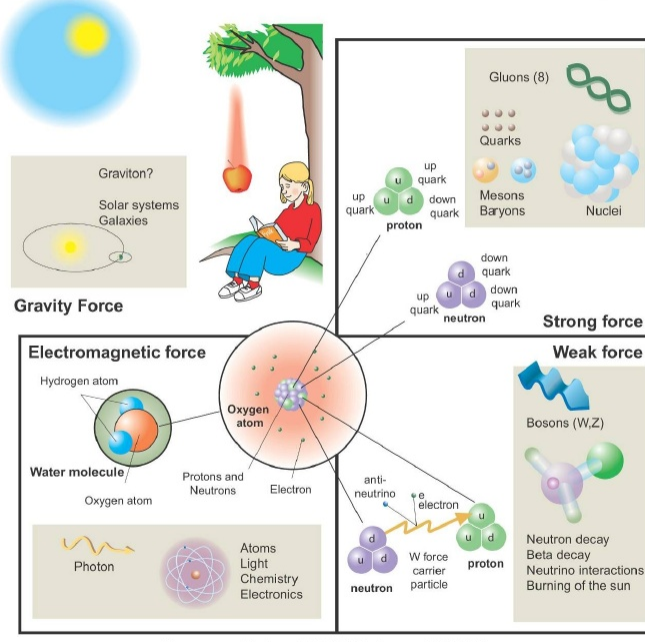
342 2.2.2 Fundamental interactions

343 Even though there are many manifestations of force in nature, like the ones repre-
 344 sented in figure 2.3, we can classify all of them into one of four fundamental interac-
 345 tions:

- 346 • *Electromagnetic interaction (EI)* affects particles that are “electrically charged,”

Fundamental interactions.

Illustration: Typoform



Summer School KPI 15 August 2009

Figure 2.3: Fundamental interactions in nature. Despite the many manifestations of forces in nature, we can track all of them back to one of the fundamental interactions. The most common forces are gravity and electromagnetic given that all of us are subject and experience them in everyday life.

347 like electrons and protons. It is described by QED combining quantum mechan-
 348 ics, special relativity and electromagnetism in order to explain how particles
 349 with electric charge interact through the exchange of photons, therefore, one
 350 says that “Electromagnetic Force” is mediated by “photons”. Figure 2.4a. shows
 351 a graphical representation, known as “feynman diagram”, of electron-electron
 352 scattering.

- 353 • *Strong interaction (SI)* described by Quantum Chromodynamics (QCD). Hadrons
 354 like proton and neutron have internal structure given that they are composed
 355 of two or more valence quarks⁵. Quarks have fractional electric charge which
 356 means that they are subject to electromagnetic interaction and in the case of the

⁵ particles made of four and five quarks are exotic states not so common.

357 proton they should break apart due to electrostatic repulsion; however, quarks
 358 are held together inside the hadrons against their electrostatic repulsion by the
 359 “Strong Force” through the exchange of “gluons.” The analog to the electric
 360 charge is the “color charge”. Electrons and photons are elementary particles
 361 as quarks but they don’t carry color charge, therefore they are not subject to
 362 SI. The feynman diagram for gluon exchange between quarks is shown in figure
 363 2.4b.

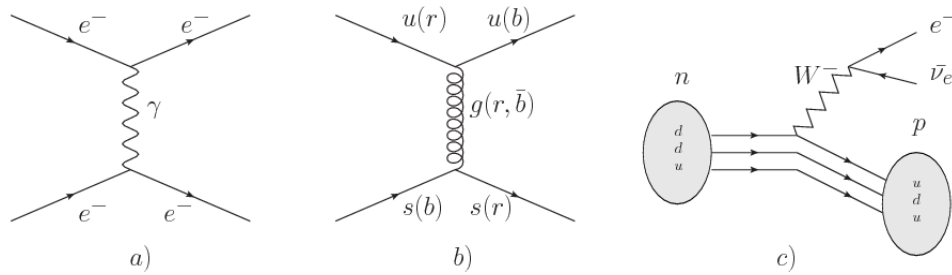


Figure 2.4: Feynman diagrams representing the interactions in SM; a) EI: e^- - e^- scattering; b) SI: gluon exchange between quarks ; c) WI: β -decay

364 • *Weak interaction (WI)* described by the weak theory (WT), is responsible, for
 365 instance, for the radioactive decay in atoms and proton-proton (pp) fusion
 366 within the sun. Quarks and leptons are the particles affected by the weak
 367 interaction; they possess a property called “flavor charge” (see 2.2.1) which can
 368 be changed by emitting or absorbing one weak force mediator. There are three
 369 mediators of the “weak force” known as “Z” boson in the case of electrically
 370 neutral changes and “ W^\pm ” bosons in the case of electrically charged changes.
 371 The “weak isospin” is the WI analog to electric charge in EI, and color charge
 372 in SI, and defines how quarks and leptons are affected by the weak force. Figure
 373 2.4c. shows the feynman diagram of β -decay where a newtron (n) is transformed
 374 in a proton (p) by emmiting a W^- particle. Since this thesis is in the frame
 375 of the electroweak interaction, a more detailed description of it will be given in

376 section 2.3

- 377 • *Gravitational interaction (GI)* described by General Theory of Relativity (GR).
 378 It is responsible for the structure of galaxies and black holes as well as the
 379 expansion of the universe. As a classical theory, in the sense that it can be for-
 380 mulated without even appeal to the concept of quantization, it implies that the
 381 spacetime is a continuum and predictions can be made without limitation to the
 382 precision of the measurement tools. The latter represent a direct contradiction
 383 of the quantum mechanics principles. Gravity is deterministic while quantum
 384 mechanics is probabilistic; despite that, efforts to develop a quantum theory of
 385 gravity have predicted the “graviton” as mediator of the Gravitational force⁶.

Interaction	Acts on	Relative strength	Range (m)	Mediators
Electromagnetic (QED)	Electrically charged particles	10^{-2}	Infinite	Photon
Strong (QCD)	Quarks and gluons	1	10^{-15}	Gluon
Weak (WI)	Leptons and quarks	10^{-6}	10^{-18}	W^\pm, Z
Gravitational (GI)	Massive particles	10^{-39}	Infinite	Graviton

Table 2.6: Fundamental interactions features [20].

386

387 Table 2.6 summarizes the main features of the fundamental interactions. The rela-
 388 tive strength of the fundamental forces reveals the meaning of strong and weak; in
 389 a context where the relative strength of the SI is 1, the EI is about hundred times
 390 weaker and WI is about million times weaker than the SI. A good description on
 391 how the relative strength and range of the fundamental interactions are calculated
 392 can be found in references [20, 21]. In the everyday life, only EI and GI are explicitly
 393 experienced due to the range of these interactions; i.e., at the human scale distances

⁶ Actually a wide variety of theories have been developed in an attempt to describe gravity; some famous examples are string theory and supergravity.

394 only EI and GI have appreciable effects, in contrast to SI which at distances greater
 395 than 10^{-15} m become negligible.

396

397 QED was built successfully on the basis of the classical electrodynamics theory (CED)
 398 of Maxwell and Lorentz, following theoretical and experimental requirements imposed
 399 by

- 400 • lorentz invariance: independence on the reference frame.
- 401 • locallity: interacting fields are evaluated at the same space-time point to avoid
 402 action at a distance.
- 403 • renormalizability: physical predictions are finite and well defined
- 404 • particle spectrum, symmetries and conservation laws already known must emerge
 405 from the theory.
- 406 • gauge invariance.

407 The gauge invariance requirement reflects the fact that the fundamental fields cannot
 408 be directly measured but associated fields which are the observables. Electric (“**E**”)
 409 and magnetic (“**B**”) fields in CED are associated with the electric scalar potential
 410 “**V**” and the vector potential “**A**”. In particular, **E** can be obtained by measuring
 411 the change in the space of the scalar potential (ΔV); however, two scalar potentials
 412 differing by a constant “f” correspond to the same electric field. The same happens in
 413 the case of the vector potential “**A**”; thus, different configurations of the associated
 414 fields result in the same set of values of the observables. The freedom in choosing
 415 one particular configuration is known as “gauge freedom”; the transformation law con-
 416 necting two configurations is known as “gauge transformation” and the fact that the

417 observables are not affected by a gauge transformation is called “gauge invariance”.

418

419 When the gauge transformation:

$$\begin{aligned}\mathbf{A} &\rightarrow \mathbf{A} - \Delta f \\ V &\rightarrow V - \frac{\partial f}{\partial t}\end{aligned}\tag{2.4}$$

420 is applied to Maxwell equations, they are still satisfied and the fields remain invariant.

421 Thus, CED is invariant under gauge transformations and is called a “gauge theory”.

422 The set of all gauge transformations form the “symmetry group” of the theory, which

423 according to the group theory, has a set of “group generators”. The number of group

424 generators determine the number of “gauge fields” of the theory.

425

426 As mentioned in the first lines of section 2.2, QED has one symmetry group ($U(1)$)

427 with one group generator (the Q operator) and one gauge field (the electromagnetic

428 field A^μ). In CED there is not a clear definition, beyond the historical convention, of

429 which fields are the fundamental and which are the associated, but in QED it is clear

430 that the fundamental field is A^μ . When a gauge theory is quantized, the gauge field

431 is quantized and its quanta is called “gauge boson”. The word boson characterizes

432 particles with integer spin which obvey Bose-einstein statistics.

433

434 As will be detailed in section 2.3, interactions between particles in a system can be

435 obtained by considering first the Lagrangian density of free particles in the system,

436 which of course is incomplete because the interaction terms have been left out, and

437 demanding global phase transformation invariance. Global phase transformation in-

438 variance means that a gauge transformation is performed identically to every point
 439 in the space⁷ and the Lagrangian remains invariant. Then, the global transformation
 440 is promoted to a local phase transformation (this time the gauge transformation de-
 441 pends on the position in space) and again invariance is required.

442

443 Due to the space dependence of the local tranformation, the Lagrangian density is
 444 not invariant anymore. In order to restate the gauge invariance, the gauge covariant
 445 derivative is introduced in the Lagrangian and with it the gauge field responsible for
 446 the interaction between particles in the system. The new Lagrangian density is gauge
 447 invariant, includes the interaction terms needed to account for the interactions and
 448 provides a way to explain the interaction between particles through the exchange of
 449 the gauge boson.

450 This recipe was used to build QED and the theories that aim to explain the funda-
 451 mental interactions.

452 **2.2.3 Gauge bosons**

453 The importance of the gauge bosons comes from the fact that they are the force
 454 mediators or force carriers. The features of the gauge bosons reflect those of the
 455 fields they represent and they are extracted from the Lagrangian density used to
 456 describe the interactions. In section 2.3, it will be shown how the gauge bosons of the
 457 EI and WI emerge from the electroweak Lagrangian. The SI gauge bosons features
 458 are also extracted from the SI Lagrangian but it is not detailed in this document. The
 459 main features of the SM gauge bosons will be briefly presented below and summarized
 460 in table 2.7.

⁷ Here space corresponds to the 4-dimensional space i.e. space-time.

- 461 • **Photon.** EI occurs when the photon couples to (is exchanged between) particles
 462 carrying electric charge; however, the photon itself does not carry electric charge,
 463 therefore, there is no coupling between photons. Given that the photon is
 464 massless the EI is of infinite range, i.e., electrically charged particles interact
 465 even if they are located far away one from each other; this also implies that
 466 photons always move with the speed of light.
- 467 • **Gluon.** SI is mediated by gluons which, same as photons, are massless. They
 468 carry one unit of color charge and one unit of anticolor charge which means that
 469 gluons couple to other gluons. As a result, the range of the SI is not infinite
 470 but very short due to the attraction between gluons, giving rise to the “color
 471 confinement” which explains why color charged particles cannot be isolated but
 472 live within composited particles, like quarks inside protons.
- 473 • **W, Z.** The WI mediators, W^\pm and Z, are massive which explains their short-
 474 range. Given that the WI is the only interaction that can change the flavor
 475 of the interacting particles, the W boson is the responsible for the nuclear
 476 transmutation where a neutron is converted in a proton or vice versa with the
 477 involvement of an electron and a neutrino (see figure 2.4c). The Z boson is the
 478 responsible of the neutral weak processes like neutrino elastic scattering where
 479 no electric charge but momentum transference is involved. WI gauge bosons
 480 carry isospin charge which makes possible the interaction between them.

Interaction	Mediator	Electric charge (e)	Color charge	Weak Isospin	mass (GeV/c ²)
Electromagnetic	Photon (γ)	0	No	0	0
Strong	Gluon (g)	0	Yes -octet	No	0
Weak	W^\pm	± 1	No	± 1	80.385 ± 0.015
	Z	0	No	0	91.188 ± 0.002

Table 2.7: SM gauge bosons main features [9].

482 2.3 Electroweak unification and the Higgs

483 mechanism

484 Physicists dream of building a theory that contains all the interactions in one single
 485 interaction, i.e., showing that at some scale in energy all the four fundamental in-
 486 teractions are unified and only one interaction emerges in a “Theory of everything”.
 487 The first sign of the feasibility of such unification comes from success in the con-
 488 struction of the CED. Einstein spent years trying to reach that dream, which by
 489 1920 only involved electromagnetism and gravity, with no success; however, a new
 490 partial unification was achieved in the 1960’s, when S.Glashow [22], A.Salam [23] and
 491 S.Weinberg [24] independently proposed that electromagnetic and weak interactions
 492 are two manifestations of a more general interaction called “electroweak interaction
 493 (EWT)”. Both, QCD and EWT, were developed in parallel and following the useful
 494 prescription provided by QED and the gauge invariance principles.

495

496 The theory of weak interactions was capable of explaining the β -decay and in general
 497 the processes mediated by W^\pm bosons. However, there were some processes like the
 498 “ $\nu_\mu - e$ scattering” which would require the exchange of two W bosons (see figure 2.5
 499 top diagrams) giving rise to divergent loop integrals and then non finite predictions.
 500 By including neutral currents involving fermions via the exchange of neutral bosons
 501 Z, those divergences are compensated and the predictions become realistic.

502

503 Neutral weak interaction vertices conserve flavor in the same way as the electromag-
 504 netic vertices do, but additionally, the Z boson can couple to neutrinos which implies
 505 that processes involving charged fermions can proceed through EI or WI but processes
 506 involving neutrinos can proceed only through WI.

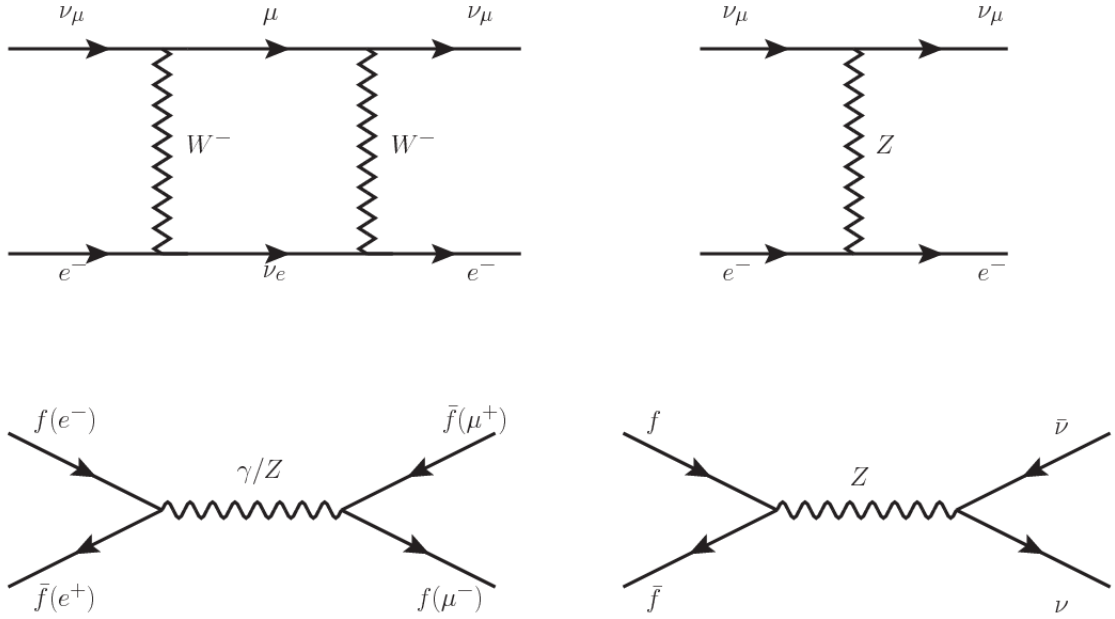


Figure 2.5: Top: $\nu_\mu - e^-$ scattering going through charged currents (left) and neutral currents (right). Bottom: neutral current processes for charged fermions (left) and involving neutrinos (right). While neutral current processes involving only charged fermions can proceed through EI or WI, those involving neutrinos can only proceed via WI.

507

508 The prescription to build a gauge theory of the WI consists of proposing a free field
 509 Lagrangian density that includes the particles involved; next, by requesting invari-
 510 ance under global phase transformations first and generalizing to local phase trans-
 511 formations invariance later, the conserved currents are identified and interactions are
 512 generated by introducing gauge fields. Given that the goal is to include the EI and
 513 WI in a single theory, the group symmetry considered should be a combination of
 514 $SU(2)_L$ and $U(1)_{em}$, however the latter cannot be used directly because the EI treats
 515 left and right-handed particles indistinctly in contrast to the former. Fortunately, the
 516 weak hypercharge, which is a combination of the weak isospin and the electric charge
 517 (eqn 2.2) is suitable to be used since it is conserved by the EI and WI. Thus, the
 518 symmetry group to be considered is

$$G \equiv SU(2)_L \otimes U(1)_Y \quad (2.5)$$

519 The following treatment applies to any of the fermion generations, but for simplicity
 520 the first generation of leptons will be considered [5, 6, 25, 26].

521

522 Given the first generation of leptons

$$\psi_1 = \begin{pmatrix} \nu_e \\ e^- \end{pmatrix}_L, \quad \psi_2 = \nu_{eR}, \quad \psi_3 = e_R^- \quad (2.6)$$

523 the charged fermionic currents are given by

$$J_\mu \equiv J_\mu^+ = \bar{\nu}_{eL} \gamma_\mu e_L, \quad J_\mu^\dagger \equiv J_\mu^- = \bar{e}_L \gamma_\mu \nu_{eL} \quad (2.7)$$

524 and the free Lagrangian is given by

$$\mathcal{L}_0 = \sum_{j=1}^3 i\bar{\psi}_j(x) \gamma^\mu \partial_\mu \psi_j(x). \quad (2.8)$$

525 Mass terms are included directly in the QED and QCD free Lagrangians since they
 526 preserve the invariance under the symmetry transformations involved which treat
 527 left-handed and right-handed similarly, however mass terms of the form

$$m_W^2 W_\mu^\dagger(x) W^\mu(x) + \frac{1}{2} m_Z^2 Z_\mu(x) Z^\mu(x) - m_e \bar{\psi}_e(x) \psi_e(x) \quad (2.9)$$

528 which represent the mass of W^\pm , Z and electrons, are not invariant under G trans-
 529 formations, therefore the gauge fields described by the EWI are in principle massless.

530

531 Experiments have shown that the gauge fields are not massless; however, they have

532 to acquire mass through a mechanism compatible with the gauge invariance; that
 533 mechanism is known as the “Higgs mechanism” and will be considered later in this
 534 section. The global transformations in the combined symmetry group G can be
 535 written as

$$\begin{aligned}\psi_1(x) &\xrightarrow{G} \psi'_1(x) \equiv U_Y U_L \psi_1(x), \\ \psi_2(x) &\xrightarrow{G} \psi'_2(x) \equiv U_Y \psi_2(x), \\ \psi_3(x) &\xrightarrow{G} \psi'_3(x) \equiv U_Y \psi_3(x)\end{aligned}\tag{2.10}$$

536 where U_L represent the $SU(2)_L$ transformation acting only on the weak isospin dou-
 537 blet and U_Y represent the $U(1)_Y$ transformation acting on all the weak isospin mul-
 538 tiplets. Explicitly

$$U_L \equiv \exp\left(i\frac{\sigma_i}{2}\alpha^i\right), \quad U_Y \equiv \exp(iy_i\beta) \quad (i = 1, 2, 3)\tag{2.11}$$

539 with σ_i the Pauli matrices and y_i the weak hypercharges. In order to promote the
 540 transformations from global to local while keeping the invariance, it is required that
 541 $\alpha^i = \alpha^i(x)$, $\beta = \beta(x)$ and the replacement of the ordinary derivatives by the covariant
 542 derivatives

$$\begin{aligned}D_\mu \psi_1(x) &\equiv [\partial_\mu + ig\sigma_i W_\mu^i(x)/2 + ig'y_1 B_\mu(x)] \psi_1(x) \\ D_\mu \psi_2(x) &\equiv [\partial_\mu + ig'y_2 B_\mu(x)] \psi_2(x) \\ D_\mu \psi_3(x) &\equiv [\partial_\mu + ig'y_3 B_\mu(x)] \psi_3(x)\end{aligned}\tag{2.12}$$

543 introducing in this way four gauge fields, $W_\mu^i(x)$ and $B_\mu(x)$, in the process. The
 544 covariant derivatives (eqn 2.12) are required to transform in the same way as fermion
 545 fields $\psi_i(x)$ themselves, therefore, the gauge fields transform as:

$$\begin{aligned} B_\mu(x) &\xrightarrow{G} B'_\mu(x) \equiv B_\mu(x) - \frac{1}{g'} \partial_\mu \beta(x) \\ W_\mu^i(x) &\xrightarrow{G} W_\mu^{i\prime}(x) \equiv W_\mu^i(x) - \frac{i}{g} \partial_\mu \alpha_i(x) - \varepsilon_{ijk} \alpha_i(x) W_\mu^j(x). \end{aligned} \quad (2.13)$$

546 The G invariant version of the Lagrangian density 2.8 can be written as

$$\mathcal{L}_0 = \sum_{j=1}^3 i \bar{\psi}_j(x) \gamma^\mu D_\mu \psi_j(x) \quad (2.14)$$

547 where free massless fermion and gauge fields and fermion-gauge boson interactions
 548 are included. The EWI Lagrangian density must additionally include kinetic terms
 549 for the gauge fields (\mathcal{L}_G) which are built from the field strengths, according to

$$B_{\mu\nu}(x) \equiv \partial_\mu B_\nu - \partial_\nu B_\mu \quad (2.15)$$

$$W_{\mu\nu}^i(x) \equiv \partial_\mu W_\nu^i(x) - \partial_\nu W_\mu^i(x) - g \varepsilon^{ijk} W_\mu^j W_\nu^k \quad (2.16)$$

550 the last term in eqn. 2.16 is added in order to hold the gauge invariance; therefore,

$$\mathcal{L}_G = -\frac{1}{4} B_{\mu\nu}(x) B^{\mu\nu}(x) - \frac{1}{4} W_{\mu\nu}^i(x) W_i^{\mu\nu}(x) \quad (2.17)$$

551 which contains not only the free gauge fields contributions, but also the gauge fields
 552 self-interactions and interactions among them.

554 The three weak isospin conserved currents resulting from the $SU(2)_L$ symmetry are
 555 given by

$$J_\mu^i(x) = \frac{1}{2} \bar{\psi}_1(x) \gamma_\mu \sigma^i \psi_1(x) \quad (2.18)$$

556 while the weak hypercharge conserved current resulting from the $U(1)_Y$ symmetry is
 557 given by

$$J_\mu^Y = \sum_{j=1}^3 \bar{\psi}_j(x) \gamma_\mu y_j \psi_j(x) \quad (2.19)$$

558 In order to evaluate the electroweak interactions modeled by an isovector field W_μ^i
 559 which couples to isospin currents J_μ^i with strength g and additionally the singlet
 560 field B_μ which couples to the weak hypercharge current J_μ^Y with strength $g'/2$. The
 561 interaction Lagrangian density to be considered is

$$\mathcal{L}_I = -g J^{i\mu}(x) W_\mu^i(x) - \frac{g'}{2} J^{Y\mu}(x) B_\mu(x) \quad (2.20)$$

562 Note that the weak isospin currents are not the same as the charged fermionic currents
 563 that were used to describe the WI (eqn 2.7), since the weak isospin eigenstates are
 564 not the same as the mass eigenstates, but they are closely related

$$J_\mu = \frac{1}{2} (J_\mu^1 + i J_\mu^2), \quad J_\mu^\dagger = \frac{1}{2} (J_\mu^1 - i J_\mu^2). \quad (2.21)$$

565 The same happens with the gauge fields W_μ^i which are related to the mass eigenstates
 566 W^\pm by

$$W_\mu^+ = \frac{1}{\sqrt{2}} (W_\mu^1 - i W_\mu^2), \quad W_\mu^- = \frac{1}{\sqrt{2}} (W_\mu^1 + i W_\mu^2). \quad (2.22)$$

567 The fact that there are three weak isospin conserved currents is an indication that in
 568 addition to the charged fermionic currents, which couple charged to neutral leptons,
 569 there should be a neutral fermionic current that does not involve electric charge
 570 exchange; therefore, it couples neutral fermions or fermions of the same electric charge.
 571 The third weak isospin current contains a term that is similar to the electromagnetic
 572 current (j_μ^{em}), indicating that there is a relation between them and resembling the
 573 Gell-Mann-Nishijima formula 2.2 adapted to electroweak interactions

$$Q = T_3 + \frac{Y_W}{2}. \quad (2.23)$$

574 Just as Q generates the $U(1)_{em}$ symmetry, the weak hypercharge generates the $U(1)_Y$
 575 symmetry as said before. It is possible to write the relationship in terms of the currents
 576 as

$$j_\mu^{em} = J_\mu^3 + \frac{1}{2}J_\mu^Y. \quad (2.24)$$

577 The neutral gauge fields W_μ^3 and B_μ cannot be directly identified with the Z and the
 578 photon fields since the photon interacts similarly with left and right-handed fermions;
 579 however, they are related through a linear combination given by

$$\begin{aligned} A_\mu &= B_\mu \cos \theta_W + W_\mu^3 \sin \theta_W \\ Z_\mu &= -B_\mu \sin \theta_W + W_\mu^3 \cos \theta_W \end{aligned} \quad (2.25)$$

580 where θ_W is known as the “Weinberg angle.” The interaction Lagrangian is now given

581 by

$$\mathcal{L}_I = -\frac{g}{\sqrt{2}}(J^\mu W_\mu^+ + J^{\mu\dagger} W_\mu^-) - \left(g \sin \theta_W J_\mu^3 + g' \cos \theta_W \frac{J_\mu^Y}{2}\right) A^\mu - \left(g \cos \theta_W J_\mu^3 - g' \sin \theta_W \frac{J_\mu^Y}{2}\right) Z^\mu \quad (2.26)$$

582 the first term is the weak charged current interaction, while the second term is the
583 electromagnetic interaction under the condition

$$g \sin \theta_W = g' \cos \theta_W = e, \quad \frac{g'}{g} = \tan \theta_W \quad (2.27)$$

584 contained in the eqn.2.24; the third term is the neutral weak current.

585

586 Note that the neutral fields transformation given by the eqn. 2.25 can be written in
587 terms of the coupling constants g and g' as:

$$A_\mu = \frac{g' W_\mu^3 + g B_\mu}{\sqrt{g^2 + g'^2}}, \quad Z_\mu = \frac{g W_\mu^3 - g' B_\mu}{\sqrt{g^2 + g'^2}} \quad (2.28)$$

588 So far, the Lagrangian density describing the non-massive EWI is:

$$\mathcal{L}_{nmEWI} = \mathcal{L}_0 + \mathcal{L}_G \quad (2.29)$$

589 where fermion and gauge fields have been considered massless because their regular
590 mass terms are manifestly non invariant under G transformations; therefore, masses
591 have to be generated in a gauge invariant way. The mechanism by which this goal is
592 achieved is known as the “Higgs mechanism” and is closely connected to the concept
593 of “spontaneous symmetry breaking.”

594 2.3.1 Spontaneous symmetry breaking (SSB)

595 Figure 2.6 left shows a steel nail (top) which is subject to an external force; the form
 596 of the potential energy is also shown (bottom).

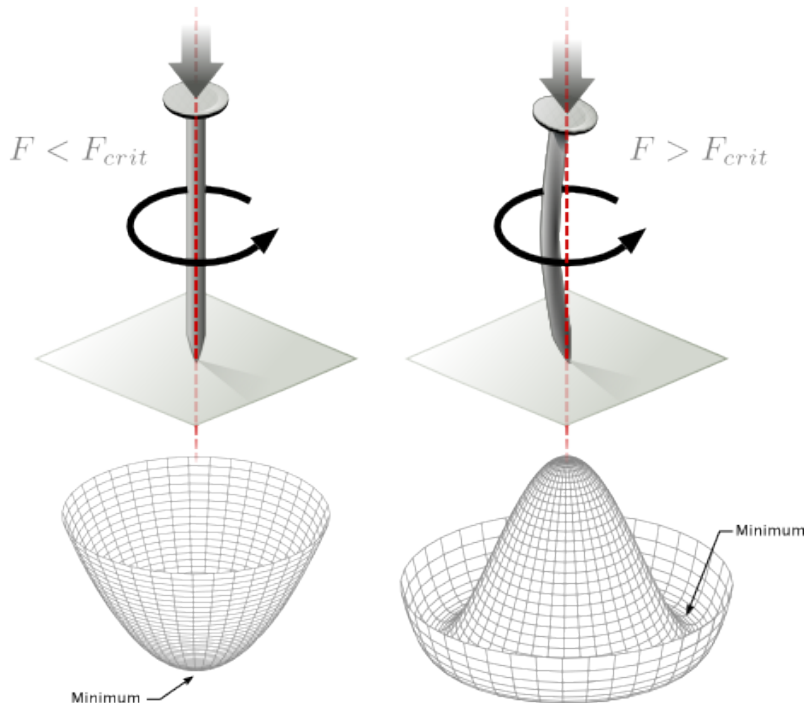


Figure 2.6: Spontaneous symmetry breaking mechanism. The steel nail, subject to an external force (top left), has rotational symmetry with respect to its axis. When the external force overcomes a critical value the nail buckles (top right) choosing a minimal energy state (ground state) and thus “*breaking spontaneously the rotational symmetry*”. The potential energy (bottom) changes but holds the rotational symmetry; however, an infinite number of asymmetric ground states are generated and circularly distributed in the bottom of the potential [27].

597

598 Before reaching the critical force value, the system has rotational symmetry with re-
 599 spect to the nail axis; however, after the critical force value is reached the nail buckles
 600 (top right). The form of the potential energy (bottom right) changes, preserving its
 601 rotational symmetry although its minima does not exhibit that rotational symmetry
 602 any longer. Right before the nail buckles there is no indication of the direction the

603 nail will bend because any of the directions are equivalent, but once the nail bends,
 604 choosing a direction, an arbitrary minimal energy state (ground state) is selected and
 605 it does not share the system's rotational symmetry. This mechanism for reaching an
 606 asymmetric ground state is known as "*spontaneous symmetry breaking*".

607 The lesson from this analysis is that the way to introduce the SSB mechanism into a
 608 system is by adding the appropriate potential to it.

609

610 Figure 2.7 shows a plot of the potential $V(\phi)$ in the case of a scalar field ϕ

$$V(\phi) = \mu^2 \phi^\dagger \phi + \lambda (\phi^\dagger \phi)^2 \quad (2.30)$$

611 If $\mu^2 > 0$ the potential has only one minimum at $\phi = 0$ and describes a scalar field
 612 with mass μ . If $\mu^2 < 0$ the potential has a local maximum at $\phi = 0$ and two minima
 613 at $\phi = \pm\sqrt{-\mu^2/\lambda}$ which enables the SSB mechanism to work.

614

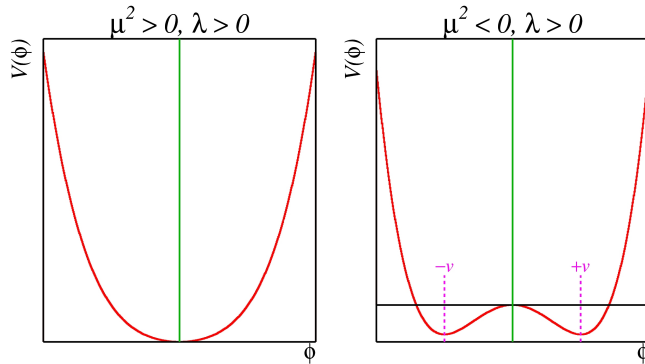


Figure 2.7: Shape of the potential $V(\phi)$ for $\lambda > 0$ and: $\mu^2 > 0$ (left) and $\mu^2 < 0$ (right). The case $\mu^2 < 0$ corresponds to the potential suitable for introducing the SSB mechanism by choosing one of the two ground states which are connected via reflection symmetry. [27].

615 In the case of a complex scalar field $\phi(x)$

$$\phi(x) = \frac{1}{\sqrt{2}}(\phi_1 + i\phi_2) \quad (2.31)$$

616 the Lagrangian (invariant under global $U(1)$ transformations) is given by

$$\mathcal{L} = (\partial_\mu \phi)^\dagger (\partial^\mu \phi) - V(\phi), \quad V(\phi) = \mu^2 \phi^\dagger \phi + \lambda (\phi^\dagger \phi)^2 \quad (2.32)$$

617 where an appropriate potential has been added in order to introduce the SSB.

618

619 As seen in figure 2.8, the potential has now an infinite number of minima circularly
 620 distributed along the ξ -direction which makes possible the occurrence of the SSB by
 621 choosing an arbitrary ground state; for instance, $\xi = 0$, i.e. $\phi_1 = v, \phi_2 = 0$

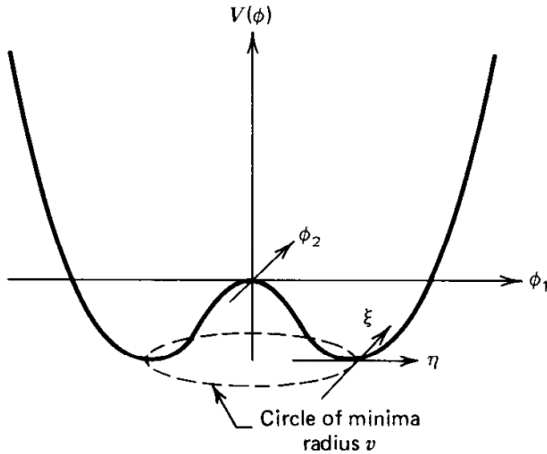


Figure 2.8: Potential for complex scalar field. There is a circle of minima of radius v along the ξ -direction [6].

$$\phi_0 = \frac{v}{\sqrt{2}} \exp(i\xi) \xrightarrow{SSB} \phi_0 = \frac{v}{\sqrt{2}} \quad (2.33)$$

622 As usual, excitations over the ground state are studied by making an expansion about

623 it; thus, the excitation can be parametrized as:

$$\phi(x) = \frac{1}{\sqrt{2}}(v + \eta(x) + i\xi(x)) \quad (2.34)$$

624 which when substituted into eqn. 2.32 produces a Lagrangian in terms of the new
625 fields η and ξ

$$\mathcal{L}' = \frac{1}{2}(\partial_\mu\xi)^2 + \frac{1}{2}(\partial_\mu\eta)^2 + \mu^2\eta^2 - V(\phi_0) - \lambda v\eta(\eta^2 + \xi^2) - \frac{\lambda}{4}(\eta^2 + \xi^2)^2 \quad (2.35)$$

626 where the last two terms represent the interactions and self-interaction between the
627 two fields η and ξ . The particular feature of the SSB mechanism is revealed when
628 looking to the first three terms of \mathcal{L}' . Before the SSB, only the massless ϕ field is
629 present in the system; after the SSB there are two fields of which the η -field has
630 acquired mass $m_\eta = \sqrt{-2\mu^2}$ while the ξ -field is still massless (see figure 2.9).

631

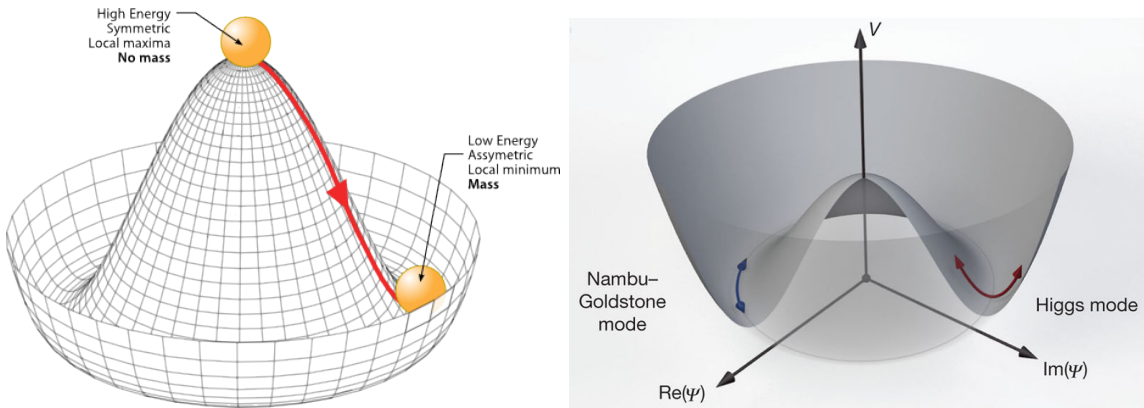


Figure 2.9: SSB mechanism for a complex scalar field [27, 28].

632 Thus, the SSB mechanism serves as a method to generate mass but as a side effect a
633 massless field is introduced in the system. This fact is known as the Goldstone theorem

and states that a massless scalar field appears in the system for each continuous symmetry spontaneously broken. Another version of the Goldstone theorem states that “*if a Lagrangian is invariant under a continuous symmetry group G , but the vacuum is only invariant under a subgroup $H \subset G$, then there must exist as many massless spin-0 particles (Nambu-Goldstone bosons) as broken generators.*” [26] The Nambu-Goldstone boson can be understood considering that the potential in the ξ -direction is flat so excitations in that direction are not energy consuming and thus represent a massless state.

2.3.2 Higgs mechanism

When the SSB mechanism is introduced in the formulation of the EWI in an attempt to generate the mass of the so far massless gauge bosons and fermions, an interesting effect is revealed. In order to keep the G symmetry group invariance and generate the mass of the EW gauge bosons, a G invariant Lagrangian density (\mathcal{L}_S) has to be added to the non massive EWI Lagrangian (eqn. 2.29)

$$\mathcal{L}_S = (D_\mu \phi)^\dagger (D^\mu \phi) - \mu^2 \phi^\dagger \phi - \lambda (\phi^\dagger \phi)^2, \quad \lambda > 0, \mu^2 < 0 \quad (2.36)$$

$$D_\mu \phi = \left(i\partial_\mu - g \frac{\sigma_i}{2} W_\mu^i - g' \frac{Y}{2} B_\mu \right) \phi \quad (2.37)$$

ϕ has to be an isospin doublet of complex scalar fields so it preserves the G invariance; thus ϕ can be defined as:

$$\phi = \begin{pmatrix} \phi^+ \\ \phi^0 \end{pmatrix} \equiv \frac{1}{\sqrt{2}} \begin{pmatrix} \phi_1 + i\phi_2 \\ \phi_3 + i\phi_4 \end{pmatrix}. \quad (2.38)$$

The minima of the potential are defined by

$$\phi^\dagger \phi = \frac{1}{2}(\phi_1^2 + \phi_2^2 + \phi_3^2 + \phi_4^2) = -\frac{\mu^2}{2\lambda}. \quad (2.39)$$

651 The choice of the ground state is critical. By choosing a ground state, invariant under
 652 $U(1)_{em}$ gauge symmetry, the photon will remain massless and the W^\pm and Z bosons
 653 masses will be generated which is exactly what is needed. In that sense, the best
 654 choice corresponds to a weak isospin doublet with $T_3 = -1/2$, $Y_W = 1$ and $Q = 0$
 655 which defines a ground state with $\phi_1 = \phi_2 = \phi_4$ and $\phi_3 = v$:

$$\phi_0 \equiv \frac{1}{\sqrt{2}} \begin{pmatrix} 0 \\ v \end{pmatrix}, \quad v^2 \equiv -\frac{\mu^2}{\lambda}. \quad (2.40)$$

656 where the vacuum expectation value v is fixed by the Fermi coupling G_F according
 657 to $v = (\sqrt{2}G_F)^{1/2} \approx 246$ GeV.

658

659 The G symmetry has been broken and three Nambu-Goldstone bosons will appear.
 660 The next step is to expand ϕ about the chosen ground state as:

$$\phi(x) = \frac{1}{\sqrt{2}} \exp\left(\frac{i}{v} \sigma_i \theta^i(x)\right) \begin{pmatrix} 0 \\ v + H(x) \end{pmatrix} \approx \frac{1}{\sqrt{2}} \begin{pmatrix} \theta_1(x) + i\theta_2(x) \\ v + H(x) - i\theta_3(x) \end{pmatrix} \quad (2.41)$$

661 to describe fluctuations from the ground state ϕ_0 . The fields $\theta_i(x)$ represent the
 662 Nambu-Goldstone bosons while $H(x)$ is known as “higgs field.” The fundamental
 663 feature of the parametrization used is that the dependence on the $\theta_i(x)$ fields is
 664 factored out in a global phase that can be eliminated by taking the physical “unitary
 665 gauge” $\theta_i(x) = 0$. Therefore the expansion about the ground state is given by:

$$\phi(x) \frac{1}{\sqrt{2}} \begin{pmatrix} 0 \\ v + H(x) \end{pmatrix} \quad (2.42)$$

666 which when substituted into \mathcal{L}_S (eqn. 2.36) results in a Lagrangian containing the now
 667 massive three gauge bosons W^\pm, Z , one massless gauge boson (photon) and the new
 668 Higgs field (H). The three degrees of freedom corresponding to the Nambu-Goldstone
 669 bosons are now integrated into the massive gauge bosons as their longitudinal po-
 670 larizations which were not available when they were massless particles. The effect
 671 by which vector boson fields acquire mass after an spontaneous symmetry breaking,
 672 but without an explicit gauge invariance breaking is known as the “*Higgs mechanism*”.

673

674 The mechanism was proposed by three independent groups: F.Englert and R.Brout
 675 in August 1964 [29], P.Higgs in October 1964 [30] and G.Guralnik, C.Hagen and
 676 T.Kibble in November 1964 [31]; however, its importance was not realized until
 677 S.Glashow [22], A.Salam [23] and S.Weinberg [24], independently, proposed that elec-
 678 tromagnetic and weak interactions are two manifestations of a more general interac-
 679 tion called “electroweak interaction” in 1967.

680 2.3.3 Masses of the gauge bosons

681 The mass of the gauge bosons is extracted by evaluating the kinetic part of Lagrangian
 682 \mathcal{L}_S in the ground state (known also as the vacuum expectation value), i.e.,

$$\left| \left(\partial_\mu - ig \frac{\sigma_i}{2} W_\mu^i - i \frac{g'}{2} B_\mu \right) \phi_0 \right|^2 = \left(\frac{1}{2} v g \right)^2 W_\mu^+ W^{-\mu} + \frac{1}{8} v^2 (W_\mu^3, B_\mu) \begin{pmatrix} g^2 & -gg' \\ -gg' & g'^2 \end{pmatrix} \begin{pmatrix} W^{3\mu} \\ B^\mu \end{pmatrix} \quad (2.43)$$

683 comparing with the typical mass term for a charged boson $M_W^2 W^+ W^-$

$$M_W = \frac{1}{2} v g. \quad (2.44)$$

The second term in the right side of the eqn.2.43 comprises the masses of the neutral

bosons, but it needs to be written in terms of the gauge fields Z_μ and A_μ in order to be compared to the typical mass terms for neutral bosons, therefore using eqn. 2.28

$$\begin{aligned} \frac{1}{8}v^2[g^2(W_\mu^3)^2 - 2gg'W_\mu^3B^\mu + g'^2B_\mu^2] &= \frac{1}{8}v^2[gW_\mu^3 - g'B_\mu]^2 + 0[g'W_\mu^3 + gB_\mu]^2 \\ &= \frac{1}{8}v^2[\sqrt{g^2 + g'^2}Z_\mu]^2 + 0[\sqrt{g^2 + g'^2}A_\mu]^2 \end{aligned} \quad (2.45)$$

684 and then

$$M_Z = \frac{1}{2}v\sqrt{g^2 + g'^2}, \quad M_A = 0 \quad (2.46)$$

685 2.3.4 Masses of the fermions

686 The lepton mass terms can be generated by introducing a gauge invariant Lagrangian
687 term describing the Yukawa coupling between the lepton field and the Higgs field

$$\mathcal{L}_{Yl} = -G_l \left[(\bar{\nu}_l, \bar{l})_L \begin{pmatrix} \phi^+ \\ \phi^0 \end{pmatrix} l_R + \bar{l}_R (\phi^-, \bar{\phi}^0) \begin{pmatrix} \nu_l \\ l \end{pmatrix}_L \right], \quad l = e, \mu, \tau. \quad (2.47)$$

688 After the SSB and replacing the usual field expansion about the ground state (eqn.2.40)
689 into \mathcal{L}_{Yl} , the mass term arises

$$\mathcal{L}_{Yl} = -m_l(\bar{l}_L l_R + \bar{l}_R l_L) - \frac{m_l}{v}(\bar{l}_L l_R + \bar{l}_R l_L)H = -m_l \bar{l} \left(1 + \frac{H}{v} \right) \quad (2.48)$$

690

$$m_l = \frac{G_l}{\sqrt{2}}v \quad (2.49)$$

691 where the additional term represents the lepton-Higgs interaction. The quark masses
692 are generated in a similar way as lepton masses but for the upper member of the

693 quark doublet a different Higgs doublet is needed:

$$\phi_c = -i\sigma_2\phi^* = \begin{pmatrix} -\bar{\phi}^0 \\ \phi^- \end{pmatrix}. \quad (2.50)$$

694 Additionally, given that the quark isospin doublets are not constructed in terms of
 695 the mass eigenstates but in terms of the flavor eigenstates, as shown in table 2.5, the
 696 coupling parameters will be related to the CKM matrix elements; thus the quark
 697 Lagrangian is given by:

$$\mathcal{L}_{Yq} = -G_d^{i,j}(\bar{u}_i, \bar{d}_i)_L \begin{pmatrix} \phi^+ \\ \phi^0 \end{pmatrix} d_{jR} - G_u^{i,j}(\bar{u}_i, \bar{d}_i)_L \begin{pmatrix} -\bar{\phi}^0 \\ \phi^- \end{pmatrix} u_{jR} + h.c. \quad (2.51)$$

698 with $i,j=1,2,3$. After SSB and expansion about the ground state, the diagonal form
 699 of \mathcal{L}_{Yq} is:

$$\mathcal{L}_{Yq} = -m_d^i \bar{d}_i d_i \left(1 + \frac{H}{v} \right) - m_u^i \bar{u}_i u_i \left(1 + \frac{H}{v} \right) \quad (2.52)$$

700 Fermion masses depend on arbitrary couplings G_l and $G_{u,d}$ and are not predicted by
 701 the theory.

702 2.3.5 The Higgs field

703 After the characterization of the fermions and gauge bosons as well as their interac-
 704 tions, it is necessary to characterize the Higgs field itself. The Lagrangian \mathcal{L}_S in eqn.
 705 2.3.6 written in terms of the gauge bosons is given by

$$\mathcal{L}_S = \frac{1}{4}\lambda v^4 + \mathcal{L}_H + \mathcal{L}_{HV} \quad (2.53)$$

706

$$\mathcal{L}_H = \frac{1}{2}\partial_\mu H \partial^\mu H - \frac{1}{2}m_H^2 H^2 - \frac{1}{2v}m_H^2 H^3 - \frac{1}{8v^2}m_H^2 H^4 \quad (2.54)$$

707

$$\mathcal{L}_{HV} = m_H^2 W_\mu^+ W^{\mu-} \left(1 + \frac{2}{v}H + \frac{2}{v^2}H^2 \right) + \frac{1}{2}m_Z^2 Z_\mu Z^\mu \left(1 + \frac{2}{v}H + \frac{2}{v^2}H^2 \right) \quad (2.55)$$

708 The mass of the Higgs boson is deduced as usual from the mass term in the Lagrangian
 709 resulting in:

$$m_H = \sqrt{-2\mu^2} = \sqrt{2\lambda}v \quad (2.56)$$

710 however, it is not predicted by the theory either. The experimental efforts to find
 711 the Higgs boson, carried out by the “Compact Muon Solenoid (CMS)” experiment
 712 and the “A Toroidal LHC AppartuS (ATLAS)” experiments at the “Large Hadron
 713 Collider(LHC)”, gave great results by July of 2012 when the discovery of a new
 714 particle compatible with the Higgs boson predicted by the electroweak theory [32, 33]
 715 was announced. Although at the announcement time there were some reservations
 716 about calling the new particle the “Higgs boson”, today this name is widely accepted.
 717 The Higgs mass measurement, reported by both experiments [34], is in table 2.8.

Property	Value
Electric charge	0
Colour charge	0
Spin	0
Weak isospin	-1/2
Weak hypercharge	1
Parity	1
Mass (GeV/c ²)	125.09±0.21 (stat.)±0.11 (syst.)

Table 2.8: Higgs boson properties. Higgs mass is not predicted by the theory and the value here corresponds to the experimental measurement.

718

719 2.3.6 Production of Higgs bosons at LHC

720 At LHC, Higgs boson is produced as a result of the collision of two counter-rotating
 721 protons beams. A detailed description of the LHC machine will be presented in
 722 chapter 3. “The total cross section” is a parameter that quantifies the number of pp
 723 collisions that happen when a number of protons are fired at each other. Different
 724 results can be obtained after a pp collision and for each one the “cross section” is

defined as the number of pp collisions that conclude in that particular result with respect to the number of protons fired at each other.

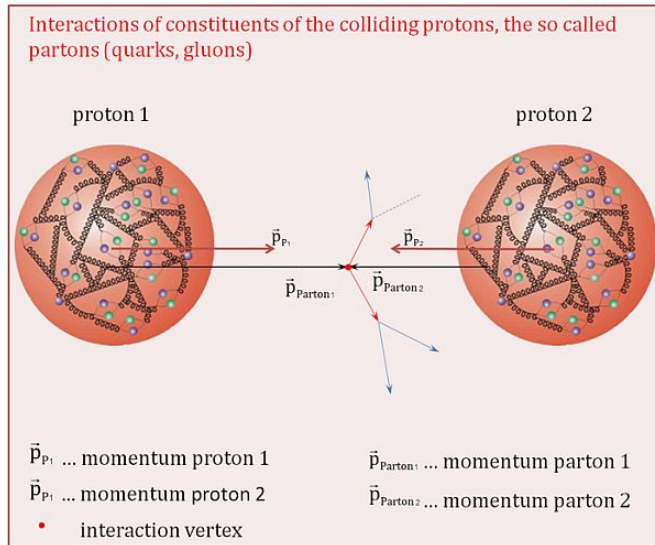


Figure 2.10: Proton-proton collision. Protons are composed of 3 valence quarks, a sea of quarks and gluons; therefore in a proton-proton collision, quarks and gluons are those who collide. [35].

726

727 Protons are composed of quarks and these quarks are bound by gluons; however,
728 what is commonly called the quark content of the proton makes reference to the
729 valence quarks. A sea of quarks and gluons is also present inside the proton as repre-
730 sented in figure 2.10. In a proton-proton (pp) collision, the constituents (quarks and
731 gluons) are those who collide. The pp cross section depends on the momentum of
732 the colliding particles, reason for which it is needed to know how the momentum is
733 distributed inside the proton. Quarks and gluons are known as partons and the func-
734 tions that describe how the proton momentum is distributed among partons inside it
735 are called “parton distribution functions (PDFs)”; PDFs are determined from experi-
736 mental data obtained in experiments where the internal structure of hadrons is tested.

737

⁷³⁸ In addition, in physics, a common approach to study complex systems consists in

739 starting with a simpler version of them, for which a well known description is avail-
 740 able, and add an additional “perturbation” which represents a small deviation from
 741 the known behavior. If the perturbation is small enough, the physical quantities as-
 742 sociated with the perturbed system are expressed as a series of corrections to those
 743 of the simpler system; therefore, the more terms are considered in the series (the
 744 higher order in the perturbation series), the more precise is the the description of the
 745 complex system.

746

747 This thesis explores the Higgs production at LHC; therefore the overview presented
 748 here will be oriented specifically to the production mechanisms after pp collisions at
 749 LHC.

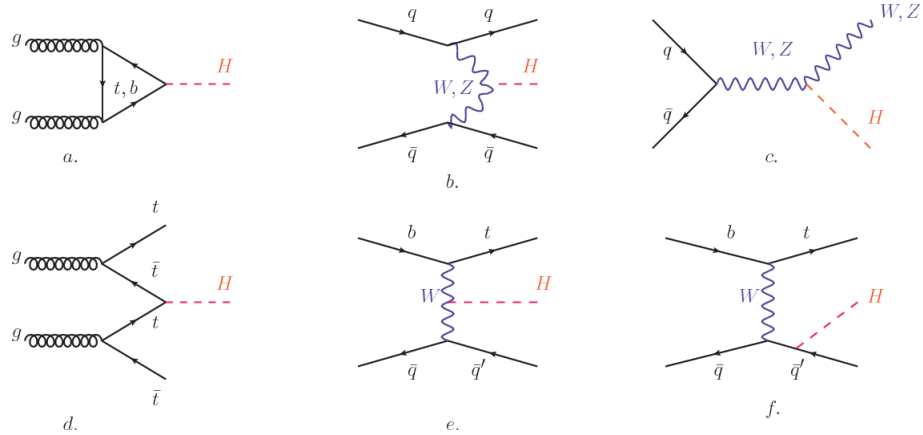


Figure 2.11: Main Higgs boson production mechanism Feynman diagrams. a. gluon-gluon fusion, b. vector boson fusion (VBF), c. Higgs-strahlung, d. Associated production with a top or bottom quark pair, e-f. associated production with a single top quark.

750 Figure 2.11 shows the Feynman diagrams for the leading order (first order) Higgs
 751 production processes at LHC, while the cross section for Higgs production as a func-
 752 tion of the center of mass-energy (\sqrt{s}) for pp collisions is showed in figure 2.12 left.
 753 The tags NLO (next to leading order), NNLO (next to next to leading order) and
 754 N3LO (next to next to next to leading order) make reference to the order at which

755 the perturbation series have been considered.

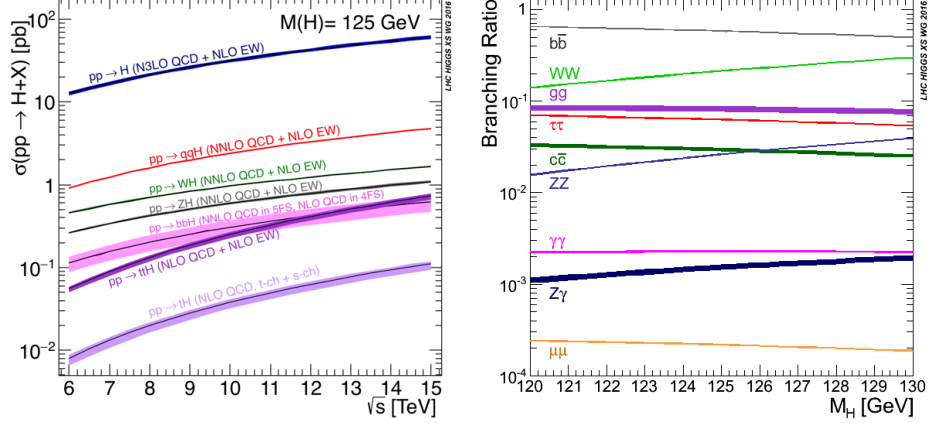


Figure 2.12: Higgs boson production cross sections (left) and decay branching ratios (right) for the main mechanisms. The VBF is indicated as $q\bar{q}H$ [36].

756 As shown in eqns 2.47, 2.51 and 2.55, the strength of the Higgs-fermion interaction
 757 is proportional to the fermion mass while the strength of the Higgs-gauge boson
 758 interaction is proportional to the square of the gauge boson mass, which implies
 759 that the Higgs production and decay mechanisms are dominated by couplings $H -$
 760 (W, Z, t, b, τ) .

761 The main production mechanism is the gluon fusion (figure 2.11a and $pp \rightarrow H$ in figure
 762 2.12) given that gluons carry the highest fraction of momentum of the protons in pp
 763 colliders. Since the Higgs boson does not couple to gluons, the mechanism proceeds
 764 through the exchange of a virtual top-quark loop given that for it the coupling is
 765 the biggest. Note that in this process, the Higgs boson is produced alone, which
 766 makes this mechanism experimentally clean when combined with the two-photon or
 767 the four-lepton decay channels (see section 2.3.7).

768 Vector boson fusion (figure 2.11b and $pp \rightarrow q\bar{q}H$ in figure 2.12) has the second largest
 769 production cross section. The scattering of two fermions is mediated by a weak
 770 gauge boson which later emits a Higgs boson. In the final state, the two fermions

771 tend to be located in a particular region of the detector which is used as a signature
 772 when analyzing the datasets provided by the experiments. More details about how
 773 to identify events of interest in an analysis will be given in chapter 5.

774 The next production mechanism is Higgs-strahlung (figure 2.11c and $pp \rightarrow WH, pp \rightarrow$
 775 ZH in figure 2.12) where two fermions annihilate to form a weak gauge boson. If the
 776 initial fermions have enough energy, the emergent boson eventually will emit a Higgs
 777 boson.

778 The associated production with a top or bottom quark pair and the associated pro-
 779 duction with a single top quark (figure 2.11d-f and $pp \rightarrow bbH, pp \rightarrow t\bar{t}H, pp \rightarrow tH$
 780 in figure 2.12) have a smaller cross section than the main three mechanisms above,
 781 but they provide a good opportunity to test the Higgs-top coupling. The analysis
 782 reported in this thesis is developed using these production mechanisms. A detailed
 783 description of the tH mechanism will be given in section 2.4.

784 2.3.7 Higgs boson decay channels

785 When a particle can decay through several modes, also known as channels, the
 786 probability of decaying through a given channel is quantified by the “branching ratio
 787 (BR)” of the decay channel; thus, the BR is defined as the ratio of number of decays
 788 going through that given channel to the total number of decays. In regard to the
 789 Higgs boson decay, the BR can be predicted with accuracy once the Higgs mass is
 790 known [37, 38]. In figure 2.12 right, a plot of the BR as a function of the Higgs mass
 791 is presented. The largest predicted BR corresponds to the $b\bar{b}$ pair decay channel (see
 792 table 2.9).

Decay channel	Branching ratio	Rel. uncertainty
$H \rightarrow bb$	5.84×10^{-1}	+3.2% – 3.3%
$H \rightarrow W^+W^-$	2.14×10^{-1}	+4.3% – 4.2%
$H \rightarrow \tau^+\tau^-$	6.27×10^{-2}	+5.7% – 5.7%
$H \rightarrow ZZ$	2.62×10^{-2}	+4.3% – 4.1%
$H \rightarrow \gamma\gamma$	2.27×10^{-3}	+5.0% – 4.9%
$H \rightarrow Z\gamma$	1.53×10^{-3}	+9.0% – 8.9%
$H \rightarrow \mu^+\mu^-$	2.18×10^{-4}	+6.0% – 5.9%

Table 2.9: Predicted branching ratios and the relative uncertainty for a SM Higgs boson with $m_H = 125 GeV/c^2$. [9]

794 **2.4 Associated production of a Higgs boson and a
795 single Top quark.**

796 Associated production of Higgs boson has been extensively studied [39–43]. While
797 measurements of the main Higgs production mechanisms rates are sensitive to the
798 strength of the Higgs coupling to W boson or top quark, they are not sensitive to the
799 relative sign between the two couplings. In this thesis, the Higgs boson production
800 mechanism explored is the associated production with a single top quark (*th*) which
801 offers sensitiveness to the relative sign of the Higgs couplings to W boson and to top
802 quark. The description given here is based on the reference [41]

803

804 A process where two incoming particles interact and produce a final state with two
805 particles can proceed in three ways also called channels (see, for instance, figure 2.13
806 ommiting the red line). The t-channel represents processes where an intermediate
807 particle is emitted by one of the incoming particles and absorbed by the other. The
808 s-channel represents processes where the two incoming particles merge into an inter-
809 mediate particle which eventually will split into the particles in the final state. The
810 third channel, u-channel, is similar to the t-channel but the two outgoing particles

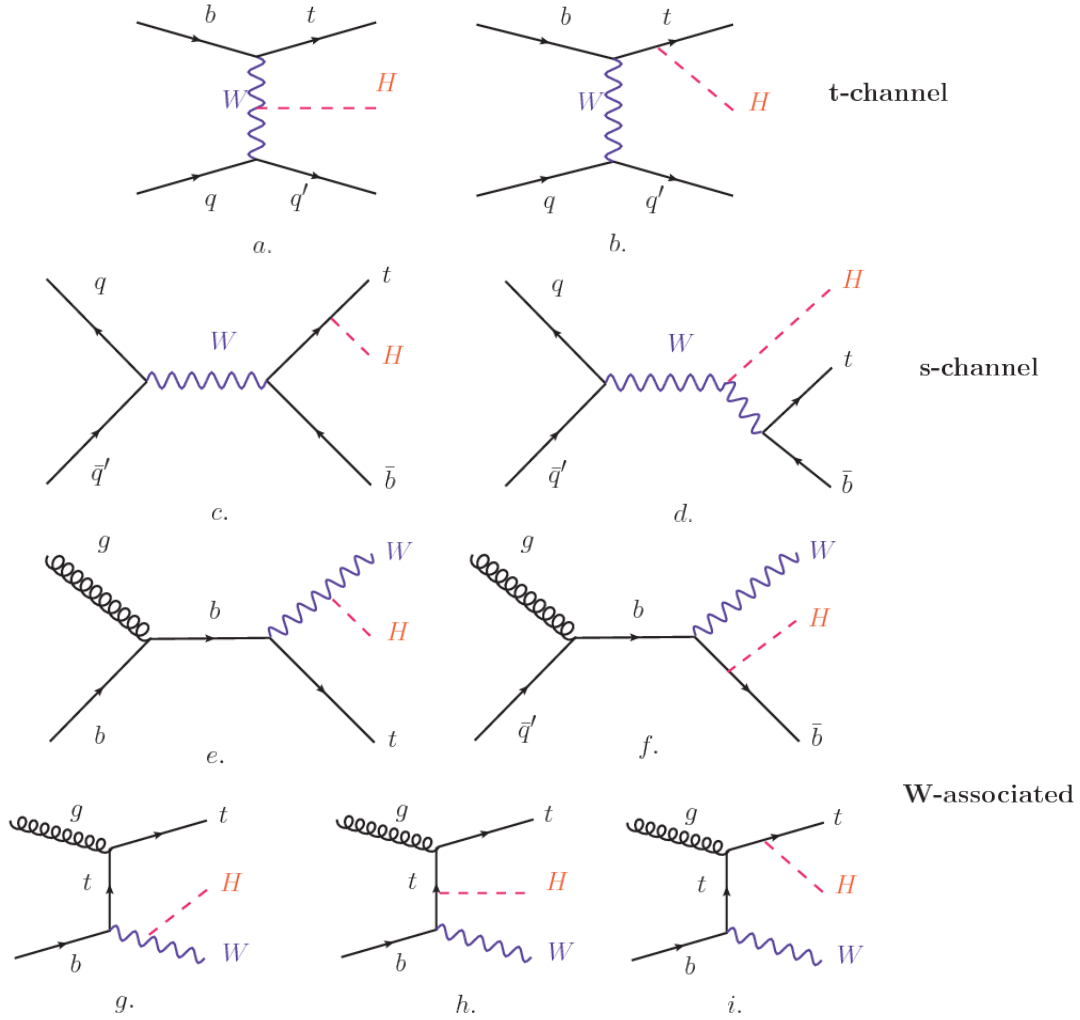


Figure 2.13: Associated Higgs boson production mechanism Feynman diagrams. a.,b. t-channel (tHq), c.,d. s-channel (tHb), e-i. W-associated.

811 interchange their roles.

812

813 The th production, where Higgs boson can be radiated either from the top quark or
 814 from the W boson, is represented by the leading order Feynman diagrams in figure
 815 2.13. The cross section for the th process is calculated, as usual, summing over
 816 the contributions from the different feynman diagrams; therefore it depends on the
 817 interference between the contributions. In the SM, the interference for t-channel (tHq

process) and W-associated (tHW process) production is destructive [39] resulting in the small cross sections presented in table 2.10.

tH production channel	Cross section (fb)
t-channel ($pp \rightarrow tHq$)	$70.79^{+2.99}_{-4.80}$
W-associated ($pp \rightarrow tHW$)	$15.61^{+0.83}_{-1.04}$
s-channel($pp \rightarrow tHb$)	$2.87^{+0.09}_{-0.08}$

Table 2.10: Predicted SM cross sections for tH production at $\sqrt{s} = 13$ TeV [44, 45].

820

821 While the s-channel contribution can be neglected, it will be shown that a deviation
 822 from the SM destructive interference would result in an enhancement of the th cross
 823 section compared to that in SM, which could be used to get information about the
 824 sign of the Higgs-top coupling [41, 42]. In order to describe th production processes,
 825 Feynman diagram 2.13b will be considered; there, the W boson is radiated by a
 826 quark in the proton and eventually it will interact with the b quark. In the high
 827 energy regime, the effective W approximation [46] allows to describe the process as
 828 the emmision of an approximately on-shell W and its hard scattering with the b
 829 quark; i.e. $Wb \rightarrow th$. The scattering amplitude for the process is given by

$$\mathcal{A} = \frac{g}{\sqrt{2}} \left[(\kappa_t - \kappa_V) \frac{m_t \sqrt{s}}{m_W v} A \left(\frac{t}{s}, \varphi; \xi_t, \xi_b \right) + \left(\kappa_V \frac{2m_W s}{v} \frac{1}{t} + (2\kappa_t - \kappa_V) \frac{m_t^2}{m_W v} \right) B \left(\frac{t}{s}, \varphi; \xi_t, \xi_b \right) \right], \quad (2.57)$$

830 where $\kappa_V \equiv g_{HVV}/g_{HVV}^{SM}$ and $\kappa_t \equiv g_{Ht}/g_{Ht}^{SM} = y_t/y_t^{SM}$ are scaling factors that quan-
 831 tify possible deviations of the couplings, Higgs-Vector boson (H-W) and Higgs-top
 832 (H-t) respectively, from the SM couplings; $s = (p_W + p_b)^2$, $t = (p_W - p_H)^2$, φ is the
 833 Higgs azimuthal angle around the z axis taken parallel to the direction of motion of
 834 the incoming W; A and B are funtions describing the weak interaction in terms of

835 the chiral states of the quarks b and t . Terms that vanish in the high energy limit
 836 have been neglected as well as the Higgs and b quark masses⁸.

837

838 The scattering amplitude grows with energy like \sqrt{s} for $\kappa_V \neq \kappa_t$, in contrast to
 839 the SM ($\kappa_t = \kappa_V = 1$), where the first term in 2.57 cancels out and the amplitude
 840 is constant for large s ; therefore, a deviation from the SM predictions represents an
 841 enhancement in the tHq cross section. In particular, for a SM H-W coupling and a H-t
 842 coupling of inverted sign with respect to the SM ($\kappa_V = -\kappa_t = 1$) the tHq cross section
 843 is enhanced by a factor greater 10 as seen in the figure 2.14 taken from reference [41];
 844 reference [47] has reported similar enhancement results.

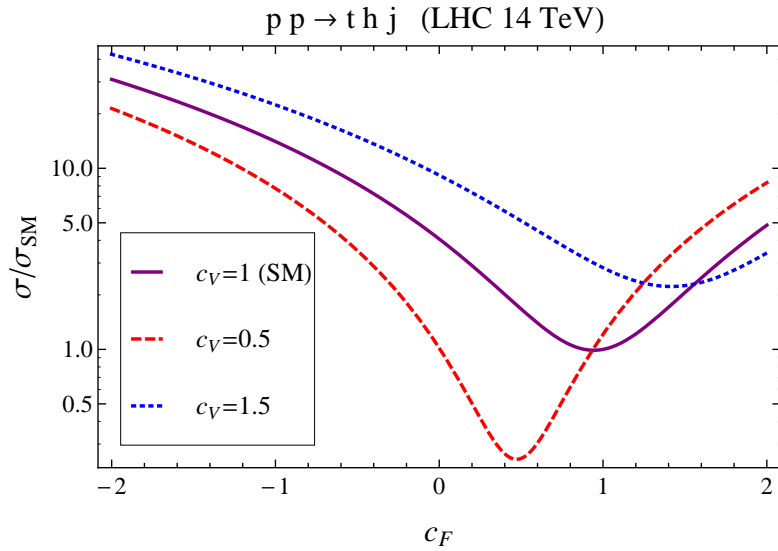


Figure 2.14: Cross section for tHq process as a function of κ_t , normalized to the SM, for three values of κ_V . In the plot c_f refers to the Higgs-fermion coupling which is dominated by the H-t coupling and represented here by κ_t . Solid, dashed and dotted lines correspond to $c_V \rightarrow \kappa_V = 1, 0.5, 1.5$ respectively. Note that for the SM ($\kappa_V = \kappa_t = 1$), the destructive effect of the interference is maximal.

845 A similar analysis is valid for the W-associated channel but, in that case, the inter-
 846 ference is more complicated since there are more than two contributions and an ad-

⁸ A detailed explanation of the structure and approximations used to derive \mathcal{A} can be found in reference [41]

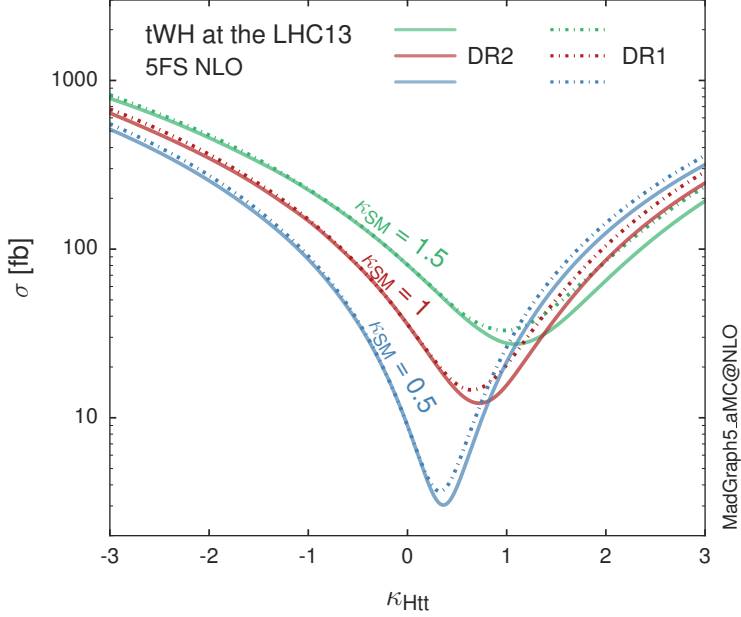


Figure 2.15: Cross section for tHW process as a function of κ_{Htt} , for three values of κ_{SM} at $\sqrt{s} = 13$ TeV. $\kappa_{Htt}^2 = \sigma_{Htt}/\sigma_{Htt}^{SM}$ is a simple rescaling of the SM Higgs interactions.

ditional interference with the production of Higgs boson and a top pair process($t\bar{t}H$).
 The calculations are made using the so-called Diagram Removal (DR) technique where
 interfering diagrams are removed (or added) from the calculations in order to evaluate
 the impact of the removed contributions. DR1 was defined to neglect $t\bar{t}H$ interference
 while DR2 was defined to take $t\bar{t}H$ interference into account [48]. As shown in figure
 2.15, the tHW cross section is enhanced from about 15 fb (SM: $\kappa_{Htt} = 1$) to about
 150 fb ($\kappa_{Htt} = -1$). Differences between curves for DR1 and DR2 help to gauge the
 impact of the interference with $t\bar{t}H$.
 Results of the calculations of the tHq and tHW cross sections at $\sqrt{s} = 13$ TeV can be
 found in reference [49] and a summary of the results is presented in table 2.11.

	\sqrt{s} TeV	$\kappa_t = 1$	$\kappa_t = -1$
$\sigma^{LO}(tHq)(\text{fb})$ [41]	8	≈ 17.4	≈ 252.7
	14	≈ 80.4	≈ 1042
$\sigma^{NLO}(tHq)(\text{fb})$ [41]	8	$18.28^{+0.42}_{-0.38}$	$233.8^{+4.6}_{-0.0}$
	14	$88.2^{+1.7}_{-0.0}$	$982.8^{+28}_{-0.0}$
$\sigma^{LO}(tHq)(\text{fb})$ [47]	14	≈ 71.8	≈ 893
$\sigma^{LO}(tHW)(\text{fb})$ [47]	14	≈ 16.0	≈ 139
$\sigma^{NLO}(tHq)(\text{fb})$ [49]	8	$18.69^{+8.62\%}_{-17.13\%}$	-
	13	$74.25^{+7.48\%}_{-15.35\%}$	$848^{+7.37\%}_{-13.70\%}$
	14	$90.10^{+7.34\%}_{-15.13\%}$	$1011^{+7.24\%}_{-13.39\%}$
$\sigma^{LO}(tHW)(\text{fb})$ [48]	13	$15.77^{+15.91\%}_{-15.76\%}$	-
$\sigma^{NLO}DR1(tHW)(\text{fb})$ [48]	13	$21.72^{+6.52\%}_{-5.24\%}$	≈ 150
$\sigma^{NLO}DR2(tHW)(\text{fb})$ [48]	13	$16.28^{+7.34\%}_{-15.13\%}$	≈ 150

Table 2.11: Predicted enhancement of the tHq and tHW cross sections at LHC for $\kappa_V = 1$ and $\kappa_t = \pm 1$ at LO and NLO; the cross section enhancement of more than a factor of 10 is due to the flippling in the sign of the H-t coupling with respect to the SM one.

858 2.5 The CP-mixing in tH processes

859 In addition to the sensitivity to sign of the H-t coupling, tHq and tHW processes have
860 been proposed as a tool to investigate the possibility of a H-t coupling that does not
861 conserve CP [43, 48, 50]. Current experimental results are consistent with SM H-V
862 and H-t couplings; however, negative H-t coupling is not excluded completely [52].

863

864 In this thesis, the sensitivity of th processes to CP-mixing is also studied in the
865 effective field theory framework and based in references [43, 48]; a generic particle
866 (X_0) of spin-0 and a general CP violating interaction with the top quark, can couple
867 to scalar and pseudoscalar fermionic densities. The H-W interaction is assumed to
868 be SM-like. The Lagrangian modeling the H-t interaction is given by

$$\mathcal{L}_0^t = -\bar{\psi}_t (c_\alpha \kappa_{Htt} g_{Htt} + i s_\alpha \kappa_{Att} g_{Att} \gamma_5) \psi_t X_0, \quad (2.58)$$

869 where α is the CP-mixing phase, $c_\alpha \equiv \cos \alpha$ and $s_\alpha \equiv \sin \alpha$, κ_{Htt} and κ_{Att} are real
 870 dimensionless rescaling parameters⁹, $g_{Htt} = g_{Att} = m_t/v = y_t/\sqrt{2}$ and $v \sim 246$ GeV is
 871 the Higgs vacuum expectation value. In this parametrization, it is easy to recover
 872 three special cases

873 • CP-even coupling $\rightarrow \alpha = 0^\circ$

874 • CP-odd coupling $\rightarrow \alpha = 90^\circ$

875 • SM coupling $\rightarrow \alpha = 0^\circ$ and $\kappa_{Htt} = 1$

876 The loop induced X_0 coupling to gluons can also be described in terms of the
 877 parametrization above, according to

$$\mathcal{L}_0^g = -\frac{1}{4} \left(c_\alpha \kappa_{Hgg} g_{Hgg} G_{\mu\nu}^a G^{a,\mu\nu} + s_\alpha \kappa_{Agg} g_{Agg} G_{\mu\nu}^a \tilde{G}^{a,\mu\nu} \right) X_0. \quad (2.59)$$

878 where $g_{Hgg} = -\alpha_s/3\pi v$ and $g_{Agg} = \alpha_s/2\pi v$. Under the assumption that the top quark
 879 dominates the gluon-fusion process at LHC energies, $\kappa_{Hgg} \rightarrow \kappa_{Htt}$ and $\kappa_{Agg} \rightarrow \kappa_{Att}$,
 880 so that the ratio between the gluon-gluon fusion cross section for X_0 and for the SM
 881 Higgs prediction can be written as

$$\frac{\sigma_{NLO}^{gg \rightarrow X_0}}{\sigma_{NLO,SM}^{gg \rightarrow H}} = c_\alpha^2 \kappa_{Htt}^2 + s_\alpha^2 \left(\kappa_{Att} \frac{g_{Agg}}{g_{Hgg}} \right)^2. \quad (2.60)$$

882 If the rescaling parameters are set to

$$\kappa_{Htt} = 1, \quad \kappa_{Att} = \left| \frac{g_{Hgg}}{g_{Agg}} \right| = \frac{2}{3}. \quad (2.61)$$

883 the gluon-fusion SM cross section is reproduced for every value of the CP-mixing
 884 angle α ; therefore, by imposing that condition to the Lagrangian density 2.58, the

⁹ analog to κ_t and κ_V

CP-mixing angle is not constrained by current data. Figure 2.16 shows the NLO cross sections for t-channel tX_0 (blue) and $t\bar{t}X_0$ (red) associated production processes as a function of the CP-mixing angle α . X_0 is a generic spin-0 particle with top quark CP-violating coupling. Rescaling factors κ_{Htt} and κ_{Att} have been set to reproduce the SM gluon-fusion cross sections.

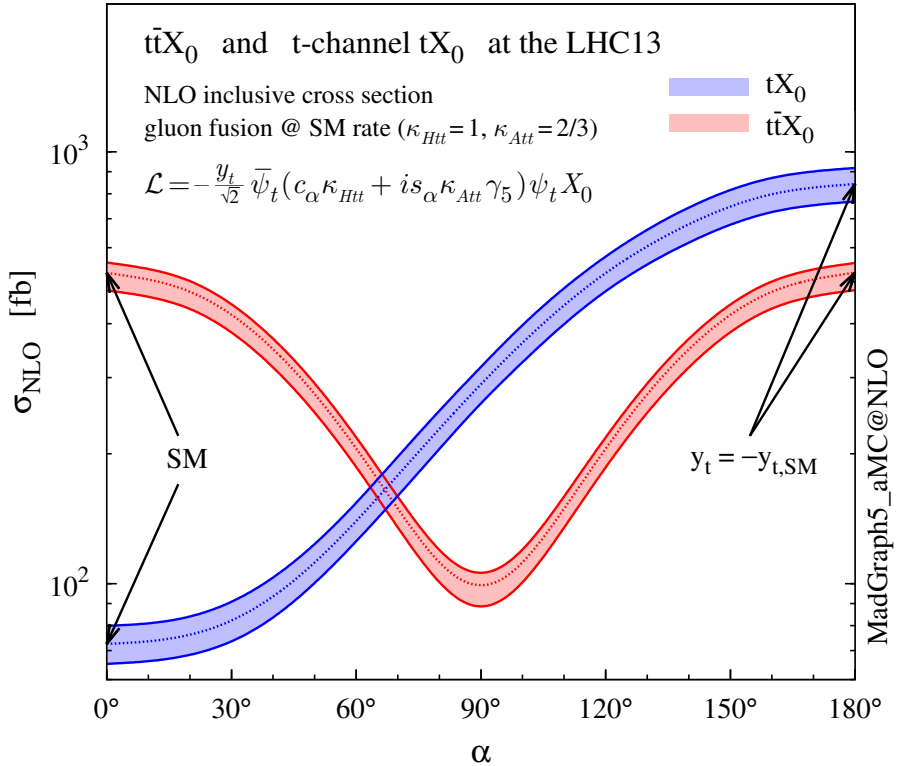


Figure 2.16: NLO cross sections for t-channel tX_0 (blue) and $t\bar{t}X_0$ (red) associated production processes as a function of the CP-mixing angle α . X_0 is a generic spin-0 particle with top quark CP-violating coupling [43].

It is interesting to notice that the tX_0 cross section is enhanced, by a factor of about 10, when a continuous rotation in the scalar-pseudoscalar plane is applied; this enhancement is similar to the enhancement produced when the H-t coupling is flipped in sign with respect to the SM ($y_t = -y_{t,SM}$ in the plot), as showed in section 2.4. In contrast, the degeneracy in the $t\bar{t}X_0$ cross section is still present given that it depends

quadratically on the H-t coupling, but more interesting is to notice that $t\bar{t}X_0$ cross section is exceeded by tX_0 cross section after $\alpha \sim 60^\circ$.

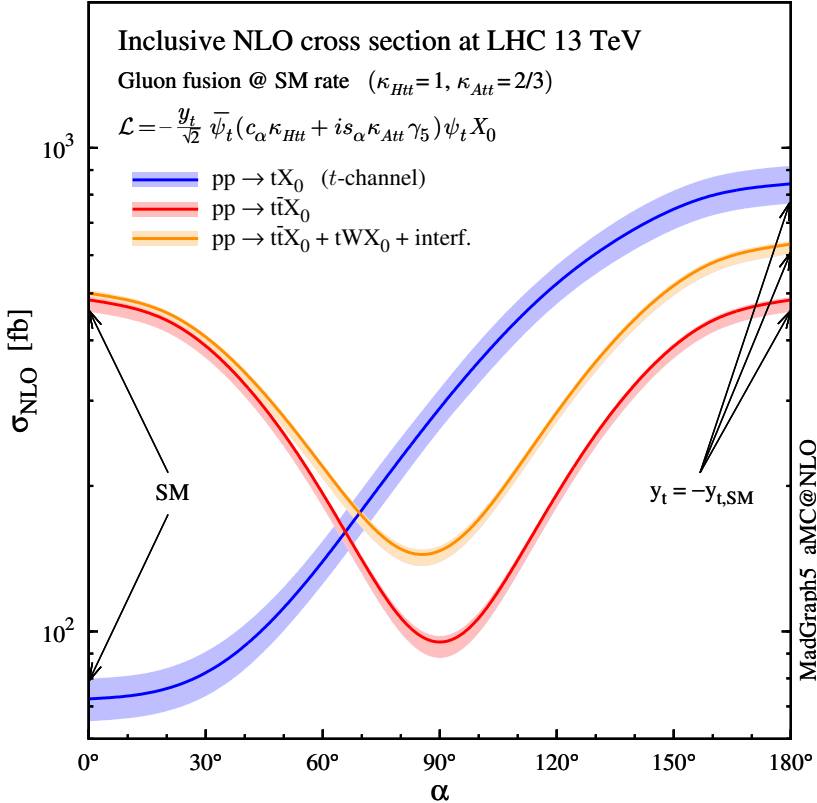


Figure 2.17: NLO cross sections for t-channel tX_0 (blue), $t\bar{t}X_0$ (red) associated production processes and combined $tWX_0 + t\bar{t}X_0$ (including interference) production as a function of the CP-mixing angle α [43].

896

897 A similar parametrization can be used to investigate the tHW process sensitivity to
 898 CP-violating H-t coupling. As said in 2.4, the interference in the W-associated chan-
 899 nel is more complicated because there are more than two contributions and also there
 900 is interference with the $t\bar{t}H$ production process.

901

902 Figure 2.17 shows the NLO cross sections for t-channel tX_0 (blue), $t\bar{t}X_0$ (red) asso-
 903 ciated production and for the combined $tWX_0 + t\bar{t}X_0 +$ interference (orange) as a
 904 function of the CP-mixing angle. It is clear that the effect of the interference in the

905 combined case is the lifting of the degeneracy present in the $t\bar{t}X_0$ production. The
 906 constructive interference enhances the cross section from about 500 fb at SM ($\alpha = 0$)
 907 to about 600 fb ($\alpha = 180^\circ \rightarrow y_t = -y_{t,SM}$).
 908 An analysis combining tHq and tHW processes will be made in this thesis taking
 909 advantage of the sensitivity improvement.

910 **2.6 Experimantal status of the anomalous**
 911 **Higg-fermion coupling.**

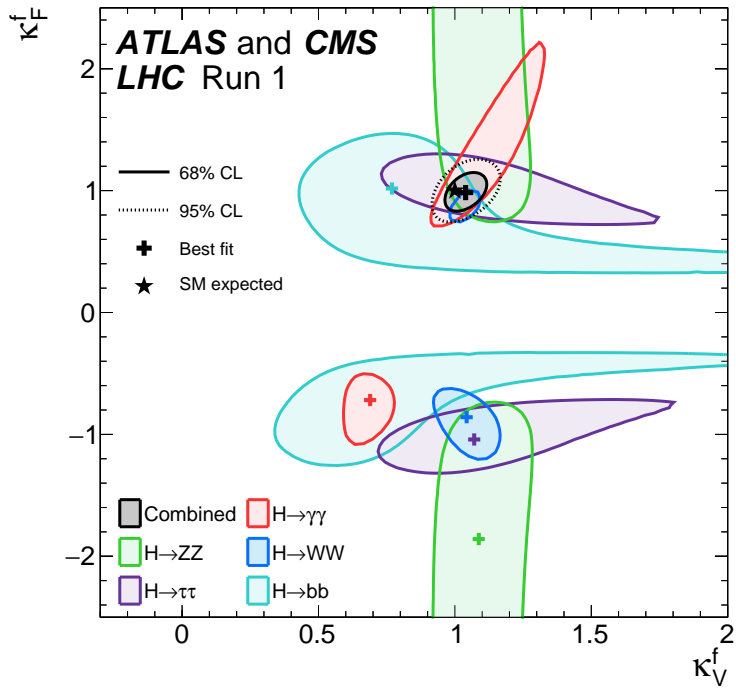


Figure 2.18: Combination of the ATLAS and CMS fits for coupling modifiers κ_t - κ_V ; also shown the individual decay channels combination and their global combination. No assumptions have been made on the sign of the coupling modifiers [52].

912 ATLAS and CMS have performed analysis of the anomalous H-f coupling by making
 913 likelihood scans for the two coupling modifiers, κ_t and κ_V , under the assumption that

914 $\kappa_Z = \kappa_W = \kappa_V$ and $\kappa_t = \kappa_\tau = \kappa_b = \kappa_f$. Figure 2.18 shows the result of the combination
915 of ATLAS and CMS fits; also the individual decay channels combination and the
916 global combination results are shown.

917 While all the channels are compatible for positive values of the modifiers, for negative
918 values of κ_t there is no compatibility. The best fit for individual channels is compatible
919 with negative values of κ_t except for the $H \rightarrow bb$ channel which is expected to be the
920 most sensitive channel; therefore, the best fit for the global fit yields $\kappa_t \geq 0$. Thus,
921 the anomalous H-t coupling cannot be excluded completely.

₉₂₂ **Chapter 3**

₉₂₃ **The CMS experiment at the LHC**

₉₂₄ **3.1 Introduction**

₉₂₅ Located on the Swiss-French border, the European Council for Nuclear Research
₉₂₆ (CERN) is the largest scientific organization leading the particle physics research.
₉₂₇ About 13000 people in a broad range of fields including users, students, scientists,
₉₂₈ engineers among others, contribute to the data taking and analysis, with the goal
₉₂₉ of unveiling the secrets of nature and revealing the fundamental structure of the
₉₃₀ universe. CERN is also the home of the Large Hadron Collider (LHC), the largest
₉₃₁ circular particle accelerator around the world, where protons (or heavy ions) traveling
₉₃₂ close to the speed of light, are made to collide. These collisions open a window
₉₃₃ to investigate how particles (and their constituents if they are composite) interact
₉₃₄ with each other, providing clues about the laws of nature. This chapter presents an
₉₃₅ overview of the LHC structure and operation. A detailed description of the CMS
₉₃₆ detector is offered, given that the data used in this thesis have been taken with this
₉₃₇ detector.

938 3.2 The LHC

939 With 27 km of circumference, the LHC is currently the largest and most powerful
 940 circular accelerator in the world. It is installed in the same tunnel where the Large
 941 Electron-Positron (LEP) collider was located, taking advantage of the existing infras-
 942 tructure. The LHC is also the larger accelerator in the CERN's accelerator complex
 943 and is assisted by several successive accelerating stages before the particles are in-
 944 jected into the LHC ring where they reach their maximum energy (see figure 3.1).

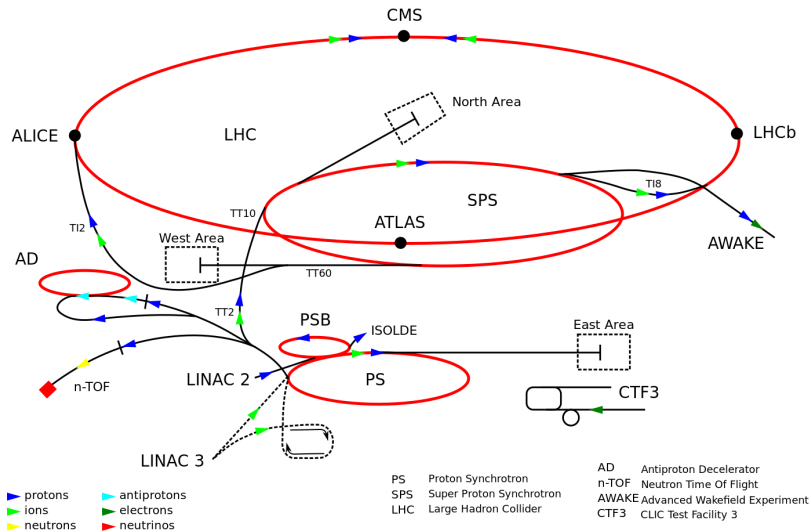


Figure 3.1: CERN accelerator complex. Blue arrows show the path followed by protons along the acceleration process [53].

945 LHC runs in three modes depending on the particles being accelerated

- 946 ● Proton-Proton collisions (pp) for multiple physics experiments.
- 947 ● Lead-Lead collisions (Pb-Pb) for heavy ion experiments.
- 948 ● Proton-Lead collisions (p-Pb) for quark-gluon plasma experiments.

949 In this thesis pp collisions will be considered.

950

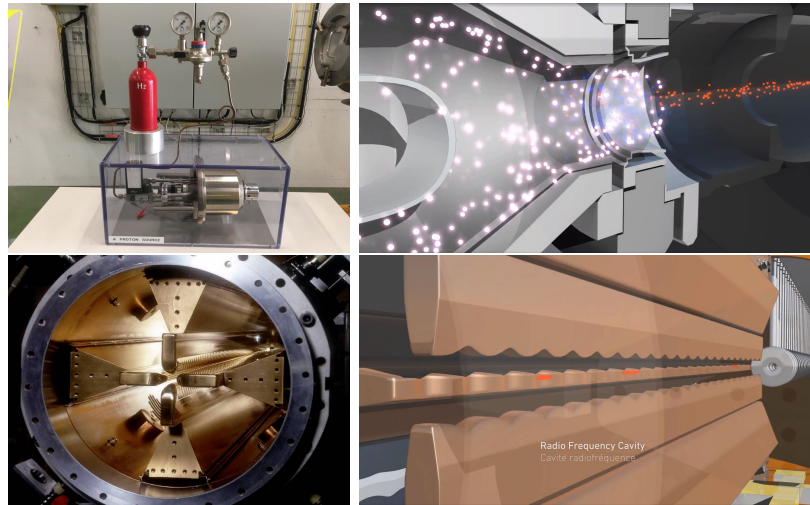


Figure 3.2: LHC protons source and the first acceleration stage. Top: the bottle contains hydrogen gas (white dots) which is injected into the metal cylinder to be broken down into electrons(blue dots) and protons(red dots); Bottom: the obtained protons are directed towards the radio frequency quadrupole which perform the first acceleration, focus the beam and create the bunches of protons. [57, 58]

951 Collection of protons starts with hydrogen atoms taken from a bottle, containing hy-
 952 drogen gas, and injecting them in a metal cylinder; hydrogen atoms are broken down
 953 into electrons and protons by an intense electric field (see figure3.2 top). The result-
 954 ing protons leave the metal cylinder towards a radio frequency quadrupole (RFQ)
 955 that focus the beam, accelerates the protons and creates the packets of protons called
 956 bunches. In the RFQ, an electric field is generated by a RF wave at a frequency that
 957 matches the resonance frequency of the cavity where the electrodes are contained.
 958 The beam of protons traveling on the RFQ axis experiences an alternating electric
 959 field gradient that generates the focusing forces.

960

961 In order to accelerate the protons, a longitudinal time-varying electric field component
 962 is added to the system; it is done by giving the electrodes a sinus-like profile as shown
 963 in figure 3.2 bottom. By matching the speed and phase of the protons with the
 964 longitudinal electric field the bunching is performed; protons synchronized with the

965 RFQ (synchronous proton) do not feel an accelerating force, but those protons in the
 966 beam that have more (or less) energy than the synchronous proton (asynchronous
 967 protons) will feel a decelerating (accelerating) force; therefore, asynchronous protons
 968 will oscillate around the synchronous ones forming bunches of protons [55]. From the
 969 RFQ protons emerge with energy 750 keV in bunches of about 1.15×10^{11} protons [56].

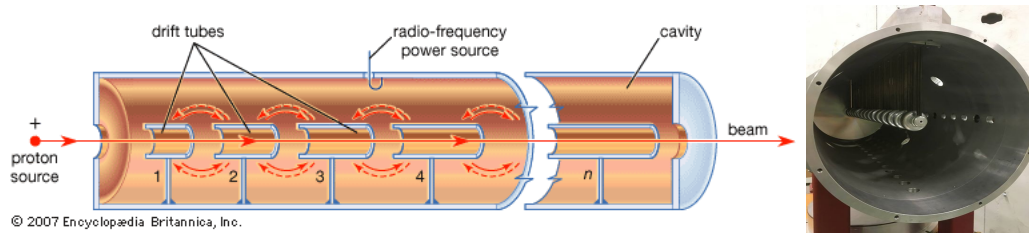


Figure 3.3: The LINAC2 accelerating system at CERN. Electric fields generated by radio frequency (RF) create acceleration and deceleration zones inside the cavity; deceleration zones are blocked by drift tubes where quadrupole magnets focus the proton beam. [59]

970 Proton bunches coming from the RFQ go to the linear accelerator 2 (LINAC2) where
 971 they are accelerated to reach 50 MeV energy. In the LINAC2 stage, acceleration
 972 is performed using electric fields generated by radio frequency which create zones
 973 of acceleration and deceleration as shown in figure 3.3. In the decelerations zones,
 974 the electric field is blocked using drift tubes where protons are free to drift while
 975 quadrupole magnets focus the beam.

976

977 The beam coming from LINAC2 is injected into the proton synchrotron booster
 978 (PSB) to reach 1.4 GeV in energy. The next acceleration is provided at the pro-
 979 ton synchrotron (PS) up to 26 GeV, followed by the injection into the super proton
 980 synchrotron (SPS) where protons are accelerated to 450 GeV. Finally, protons are
 981 injected into the LHC where they are accelerated to the target energy of 6.5 TeV.
 982 PSB, PS, SPS and LHC accelerate protons using the same RF acceleration technic
 983 described before.

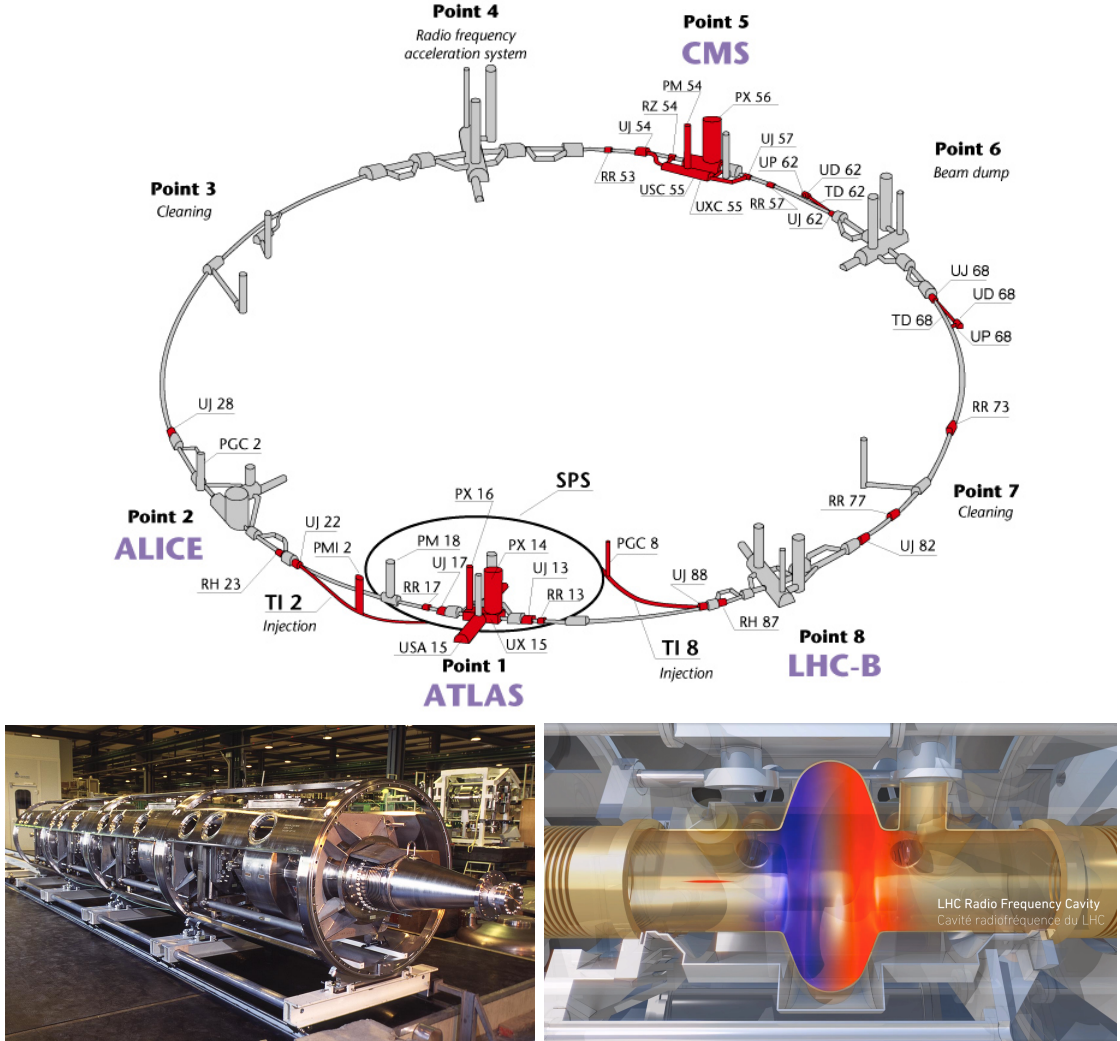


Figure 3.4: Top: LHC layout. The red zones indicate the infrastructure additions to the LEP installations, built to accomodate the ATLAS and CMS experiments which exceed the size of the former experiments located there [54]. Bottom: LHC RF cavities. A module accomodates 4 cavities that accelerate protons and preserve the bunch structure of the beam. [58, 60]

984 LHC has a system of 16 RF cavities located in the so-called point 4, as shown in
 985 figure 3.4 top, tunned at a frequency of 400 MHz and the protons are carefully timed
 986 so in addition to the acceleration effect the bunch structure of the beam is preserved.
 987 Bottom side of figure 3.4 shows a picture of a Rf module composed of 4 RF cavities
 988 working in a superconducting state at 4.5 K; also is showed a representation of the

989 accelerating electric field that accelerates the protons in the bunch.

990

991 While protons are accelerated in one section of the LHC ring, where the RF cavities
 992 are located, in the rest of their path they have to be kept in the curved trajectory
 993 defined by the LHC ring. Technically, LHC is not a perfect circle; RF, injection, beam
 994 dumping, beam cleaning and sections before and after the experimental points where
 995 protons collide are all straight sections. In total, there are 8 arcs 2.45 Km long each
 996 and 8 straight sections 545 m long each. In order to curve the proton's trajectory in
 997 the arc sections, superconducting dipole magnets are used.

998

999 Inside the LHC ring, there are two proton beams traveling in opposite directions in
 1000 two separated beam pipes; the beam pipes are kept at ultra-high vacuum ($\sim 10^{-9}$
 1001 Pa) to ensure that there are no particles that interact with the proton beams. The
 1002 superconducting dipole magnets used in LHC are made of a NbTi alloy, capable of
 1003 transporting currents of about 12000 A when cooled at a temperature below 2K using
 1004 liquid helium (see figure 3.5).

1005

1006 Protons in the arc sections of LHC feel a centripetal force exerted by the dipole
 1007 magnets which is perpendicular to the beam trajectory; The magnitude of magnetic
 1008 field needed can be found assuming that protons travel at $v \approx c$, using the standard
 1009 values for proton mass and charge and the LHC radius, as

$$F_m = \frac{mv^2}{r} = qBv \quad \rightarrow B = 8.33T \quad (3.1)$$

1010 which is about 100000 times the Earth's magnetic field. A representation of the mag-
 1011 netic field generated by the dipole magnets is shown on the bottom left side of figure

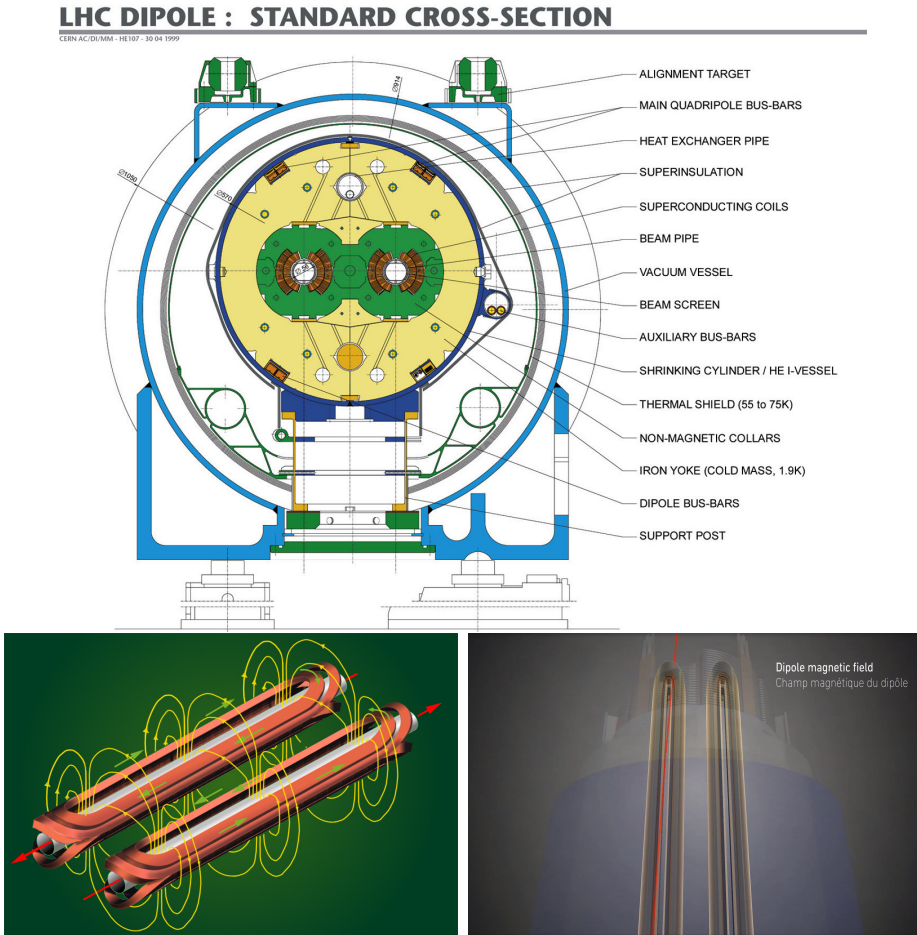


Figure 3.5: Top: LHC dipole magnet transversal view; cooling, shielding and mechanical support are indicated. Bottom left: Magnetic field generated by the dipole magnets; note that the direction of the field inside one beam pipe is opposite with respect to the other beam pipe which guarantee that both proton beams are curved in the same direction towards the center of the ring. The effect of the dipole magnetic field on the proton beam is represented on the bottom right side [58, 61, 62].

1012 3.5. The bending effect of the magnetic field on the proton beam is shown on the
 1013 bottom right side of figure 3.5. Note that the dipole magnets are not curved; the arc
 1014 section of the LHC ring is composed of straight dipole magnets of about 15 m. In
 1015 total there are 1232 dipole magnets along the LHC ring.

1016

1017 In addition to bending the beam trajectory, the beam has to be focused so it stays

1018 inside the beam pipe. The focusing is performed by quadrupole magnets installed in
 1019 a different straight section; in total 858 quadrupole magnets are installed along the
 1020 LHC ring. Other effects like electromagnetic interaction among bunches, interaction
 1021 with electron clouds from the beam pipe, the gravitational force on the protons, dif-
 1022 ferences in energy among protons in the same bunch, among others, are corrected
 1023 using sextupole and other magnetic multipoles.

1024

1025 The two proton beams inside the LHC ring are made of bunches with a cylindrical
 1026 shape of about 7.5 cm long and about 1 mm in diameter; when bunches are close
 1027 to the collision point (CP), the beam is focused up to a diameter of about 16 μm in
 1028 order to maximize the number of collisions per unit area and per second, known as
 1029 luminosity (L). Luminosity can be calculated using

$$L = fn \frac{N_1 N_2}{4\pi\sigma_x\sigma_y} \quad (3.2)$$

1030 where f is the revolution frequency, n is the number of bunches per beam, N_1 and
 1031 N_2 are the numbers of protons per bunch (1.5×10^{11}), σ_x and σ_y are the gaussian
 1032 transverse sizes of the bunches. The expected luminosity about

$$f = \frac{v}{2\pi r_{LHC}} \approx \frac{3 \times 10^8 \text{ m/s}}{27 \text{ km}} \approx 11.1 \text{ kHz},$$

$$n = 2808$$

$$N_1 = N_2 = 1.5 \times 10^{11}$$

$$\sigma_x = \sigma_y = 16 \mu\text{m}$$

1033

$$L = 1.28 \times 10^{34} \text{ cm}^{-2} \text{ s}^{-1} = 1.28 \times 10^{-5} \text{ fb}^{-1} \text{ s}^{-1} \quad (3.3)$$

1034 Luminosity is a fundamental aspect of LHC given that the bigger luminosity the bigger
 1035 number of collisions, which means that for processes with a very small cross section
 1036 the number of expected occurrences is increased and so the chances of being detected.
 1037 The integrated luminosity, i.e. the total luminosity, collected by the CMS experiment
 1038 during 2016 is shown in figure 3.6; the data analyzed in this thesis corresponds to an
 1039 integrated luminosity of 35.9 fb^{-1} at a center of mass-energy $\sqrt{s} = 13 \text{ TeV}$.
 1040 A way to increase L is increasing the number of bunches in the beam. Currently, the
 1041 separation between two consecutive bunches in the beam is 7.5 m which corresponds
 1042 to a time separation of 25 ns. In the full LHC ring the allowed number of bunches is
 1043 $n = 27\text{km}/7.5\text{m} = 3600$; however, there are some gaps in the bunch pattern intended
 1044 for preparing the dumping and injection of the beam, thus, the proton beams are
 1045 composed of 2808 bunches.

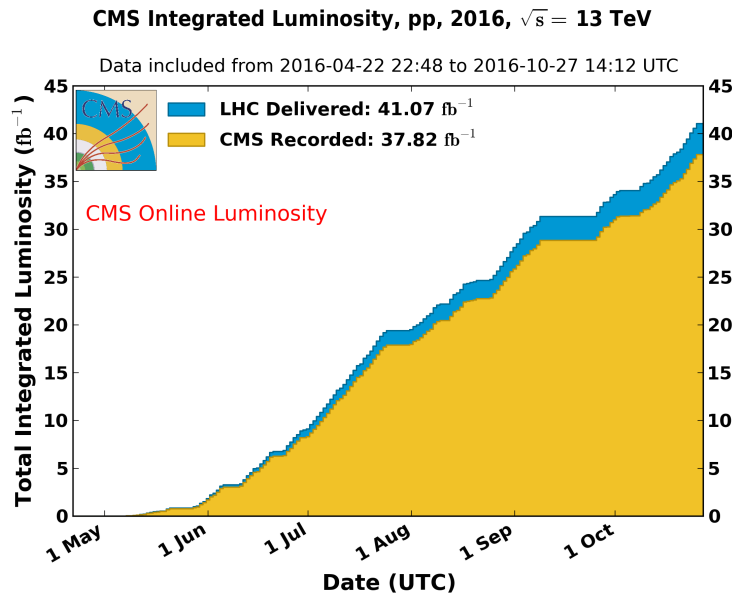


Figure 3.6: Integrated luminosity delivered by LHC and recorded by CMS during 2016. The difference between the delivered and the recorded luminosities is due to fails and issues occurred during the data taking in the CMS experiment [63].

1046 Once the proton beams reach the desired energy, they are brought to cross each other

1047 producing proton-proton collisions. The bunch crossing happens in precise places
 1048 where the four LHC experiments are located, as seen in figure 3.7 left. In 2008, the
 1049 first set of collisions involved protons with $\sqrt{s} = 7$ TeV; the energy was increased to
 1050 8 TeV in 2012 and to 13 TeV in 2015.

1051 CMS and ATLAS experiments, which are multi-purpose experiments, are enabled
 1052 to explore physics in any of the collision modes. LHCb experiment is optimized
 1053 to explore bottom quark physics, while ALICE is optimized for heavy ion collisions
 1054 searches; TOTEM and LHCf are dedicated to forward physics studies; MoEDAL (not
 1055 indicated in the figure) is intended for monopoles or massive pseudo stable particles
 1056 searches.

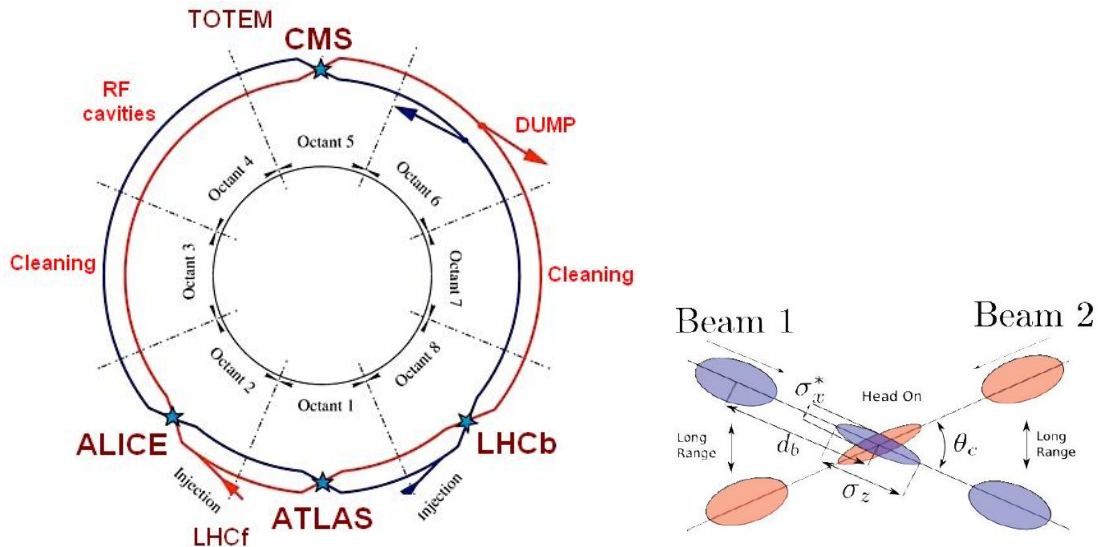


Figure 3.7: Left: LHC interaction points. Bunch crossing occurs where the LHC experiments are located [64]. Sections indicated as cleaning are dedicated to collimate the beam in order to protect the LHC ring from collisions with protons in very spreaded bunches. Right: bunch crossing scheme. Since the bunch crossing is not perfectly head-on, the luminosity is reduced in a factor of 17%.

1057 At the CP there are two interesting details that need to be addressed. The first
 1058 one is that the bunch crossing does not occur head-on but at a small crossing angle
 1059 ($280 \mu\text{rad}$ in CMS and ATLAS) as shown in the right side of figure 3.7, affecting the

1060 overlapping between bunches; the consequence is a reduction of about 17% in the
 1061 luminosity. The second one is the occurrence of multiple pp collisions in the same
 1062 bunch crossing; this effect is called pile-up (PU). A fairly simple estimation of the
 1063 PU follows from estimating the probability of collision between two protons, one from
 1064 each of the bunches in course of collision; it depends roughly on the ratio of proton
 1065 size and the cross section of the bunch in the interaction point, i.e.,

$$P(pp\text{-}collision) \sim \frac{d_{proton}^2}{\sigma_x \sigma_y} = \frac{(1\text{fm})^2}{(16\mu\text{m})^2} \sim 4 \times 10^{-21} \quad (3.4)$$

1066 however, there are $N = 1.15 \times 10^{11}$ protons in a bunch, thus the estimated number of
 1067 collisions in a bunch crossing is

$$PU = N^2 * P(pp\text{-}collision) \sim 50 \text{ pp-collision per bunch crossing}, \quad (3.5)$$

1068 about 20 of those pp collisions are inelastic. Each collision generates a vertex, but
 1069 only the most energetic is considered as a primary vertex; the rest are considered as
 1070 PU vertices. A multiple pp collision event in a bunch crossing at CMS is showed in
 1071 figure3.8. Unstable particles outgoing from the primary vertex will eventually decay;
 1072 this decay vertex is known as a secondary vertex.
 1073 Next section presents a description of the CMS detector which it is the detector used
 1074 to collect the data used in this thesis.

1075 3.3 The CMS experiment

1076 CMS is a general-purpose detector designed to conduct research in a wide range
 1077 of physics from the standard model to new physics like extra dimensions and dark

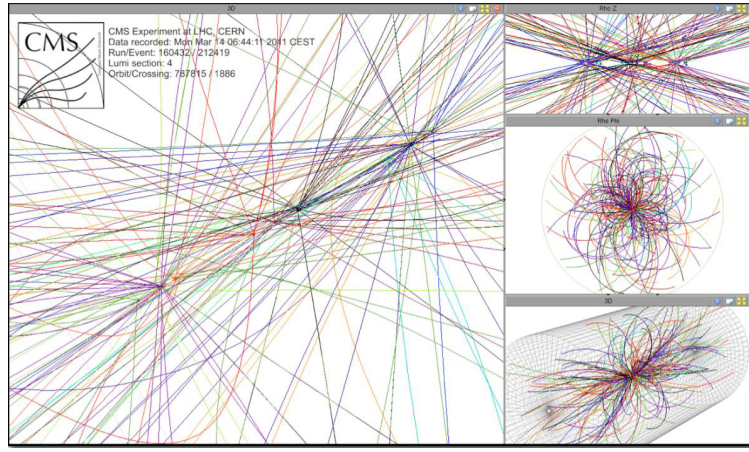


Figure 3.8: Multiple pp collision bunch crossing at CMS. Only the most energetic vertex is considered and the rets are cataloged as PU vertices [65].

matter. Located at the point 5 in the LHC layout as shown in figure 3.4, CMS is composed of several detection systems distributed in a cylindrical structure; in total, CMS weights about 12500 tons in a very compact 21.6 m long and 14.6 m diameter cylinder. It was built in 15 separate sections at the ground level and lowered to the cavern individually to be assembled. A complete and detailed description of the CMS detector and its components is given in reference [66] on which this section is based on.

1084

1085 Figure 3.9 shows the layout of the CMS detector. The design is driven by the requirements on the identification, momentum resolution and unambiguous charge determination of the muons; therefore, a large bending power is provided by the solenoid magnet made of superconducting cable capable to generate a 3.8 T magnetic field.
1088
1089 The detection system is composed of (from the innermost to the outermost)

- 1090 • Pixel detector.
1091 • Silicon strip tracker.
1092 • Preshower detector.

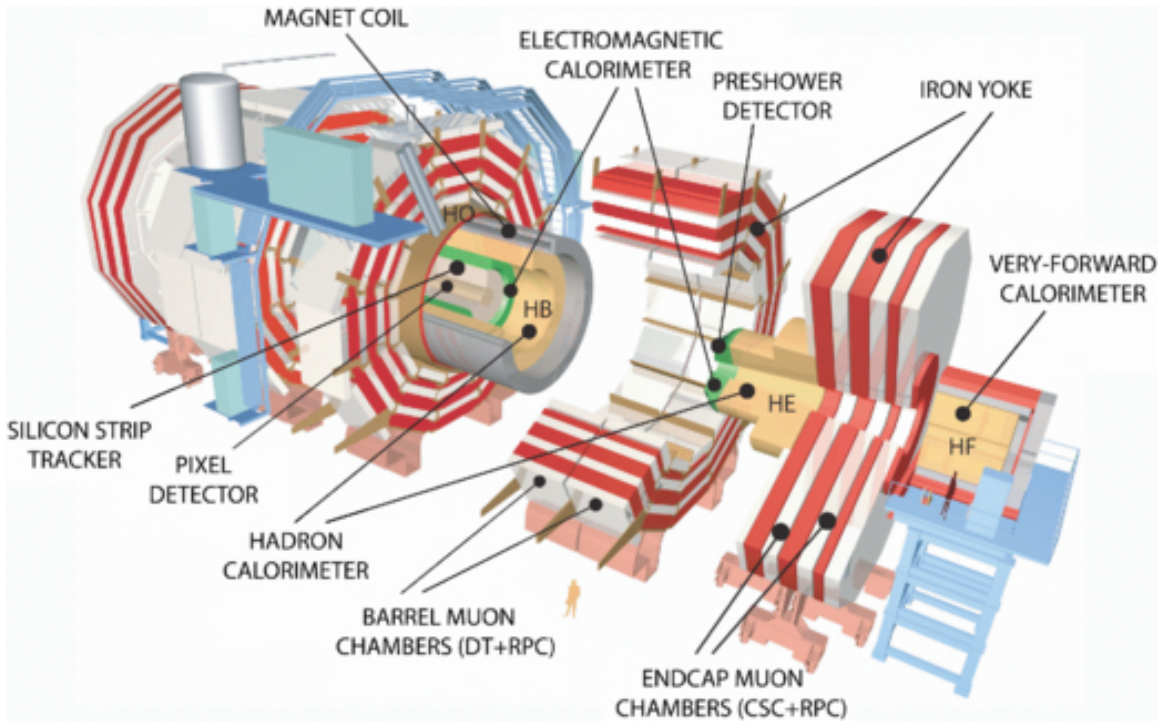


Figure 3.9: Layout of the CMS detector. The several subdetectors are indicated. The central region of the detector is referred as the Barrel section while the endcaps are referred as the forward sections. [67].

1093 • Electromagnetic calorimeter.

1094 • Hadronic calorimeter.

1095 • Muon chambers (Barrel and endcap)

1096 The central region of the detector is commonly referred as the barrel section while the
 1097 endcaps are referred as the forward sections of the detector; thus, each subdetector
 1098 is composed of a barrel section and a forward section.

1099 3.3.1 Coordinate system

1100 The coordinate system used by CMS is centered in the geometrical center of the
 1101 detector which is the same as the CP as shown in figure 3.10. The z -axis is parallel

1102 to the beam direction, while the Y -axis pointing vertically upward, and the X -axis
 1103 pointing radially inward toward the center of the LHC.

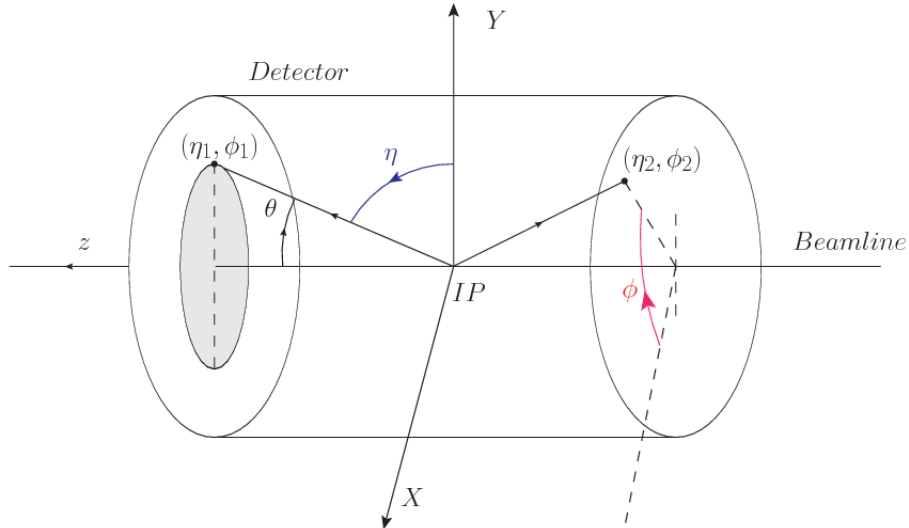


Figure 3.10: CMS detector coordinate system.

1104 In addition to the common cartesian and cylindrical coordinate systems, two coordi-
 1105 nates are of particular utility in particle physics: rapidity(y) and pseudorapidity(η),
 1106 defined in connection to the polar angle θ , energy and longitudinal momentum com-
 1107 ponent (momentum along the z -axis) according to

$$y = \frac{1}{2} \ln \frac{E + p_z}{E - p_z} \quad \eta = -\ln \left(\tan \frac{\theta}{2} \right) \quad (3.6)$$

1108 Rapidity is related to the angle between the XY -plane and the direction in which the
 1109 products of a collision are emitted; it has the nice property that the difference between
 1110 the rapidities of two particles is invariant with respect to Lorentz boosts along the z -
 1111 axis. Thus, data analysis becomes more simple when based on rapidity; however, it is
 1112 not simple to measure the rapidity of highly relativistic particles, as those produced
 1113 after pp collisions. Under the highly relativistic motion approximation, y can be
 1114 rewritten in terms of the polar angle, concluding that rapidity is approximately equal

1115 to the pseudorapidity defined above, i.e. $y \approx \eta$. Note that η is easier to measure than y
 1116 given the direct relationship between the former and the polar angle. Angular distance
 1117 between two objects in the detector (ΔR) is defined in terms of their coordinates
 1118 $(\eta_1, \phi_1), (\eta_2, \phi_2)$ as

$$\Delta R = \sqrt{(\Delta\eta)^2 - (\Delta\phi)^2} \quad (3.7)$$

1119 **3.3.2 Pixels detector**

1120 The CMS tracking system is designed to provide a precise measurement of the trajec-
 1121 tory followed by the charged particles created after the pp collisions; also, the precise
 1122 reconstruction of the primary and secondary vertices is expected in an environment
 1123 where, each 25 ns, the bunch crossing produce about 20 inelastic collisions and about
 1124 1000 particles. An increment in the luminosity is ongoing which implies that the PU
 1125 will increase accordingly.

1126

1127 The pixel detector was replaced during the 2016-2017 extended year-end technical
 1128 stop, due to the increasingly challenging operating conditions like the higher particle
 1129 flow and more radiation harsh environment, among others. The new one is respond-
 1130 ing as expected, reinforcing its crucial role in the successful way to fulfill the new
 1131 LHC physics objectives after the discovery of the Higgs boson. The last chapter of
 1132 this thesis is dedicated to describe my contribution to the “Forward Pixel Phase 1
 1133 upgrade”.

1134

1135 The current pixel detector is composed of 1856 silicon pixel detector modules orga-
 1136 nized in four-barrel layers in the central region and three disks in the forward region;
 1137 it is designed to record efficiently and with high precision, up to $10\mu\text{m}$ in the XY -

1138 plane and $20\mu\text{m}$ in the z -direction, the first four space-points near to the CP region
 1139 (see figure 3.11 left side) in the range $|\eta| \leq 2.5$. The first barrel layer is located at a
 1140 radius of 30 mm from the beamline, while the fourth layer is located at a radius of
 1141 160 mm closer to the strip tracker inner barrel layer (see section 3.3.3) in order to
 1142 reduce the rate of fake tracks. The high granularity of the detector is represented in
 1143 its about 123 Mpixels, each of size $100 \times 150\mu\text{m}^2$, which is almost twice the channels
 1144 of the old detector. The transverse momentum resolution of tracks can be measured
 1145 with a resolution of 1-2% for muons of $p_T = 100$ GeV.

1146

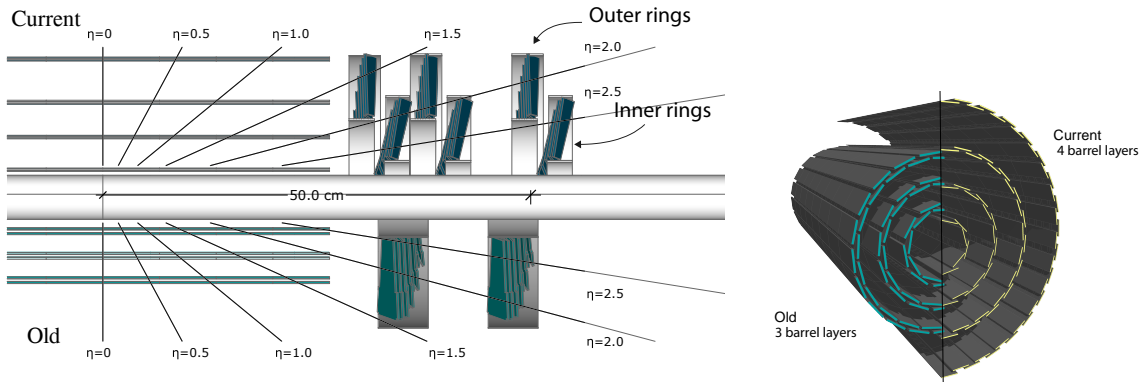


Figure 3.11: CMS pixel detector schematic view. Left: layout comparing the layers and disks in the old and current pixel detectors. Right: Transverse-oblique view comparing the pixel barrel layers in the two [69].

1147 Some of the improvements with respect to the previous pixel detector include a higher
 1148 average tracking efficiency and lower average fake rate as well as higher track impact
 1149 parameter resolution which is fundamental in order to increase the efficiency in the
 1150 identification of jets originating from b quarks (b-tagging). A significant source of
 1151 improvement comes from the overall reduction in the material budget of the detector
 1152 which results in fewer photon conversions and less multiple scattering from charged
 1153 particles.

1154 **3.3.3 Silicon strip tracker**

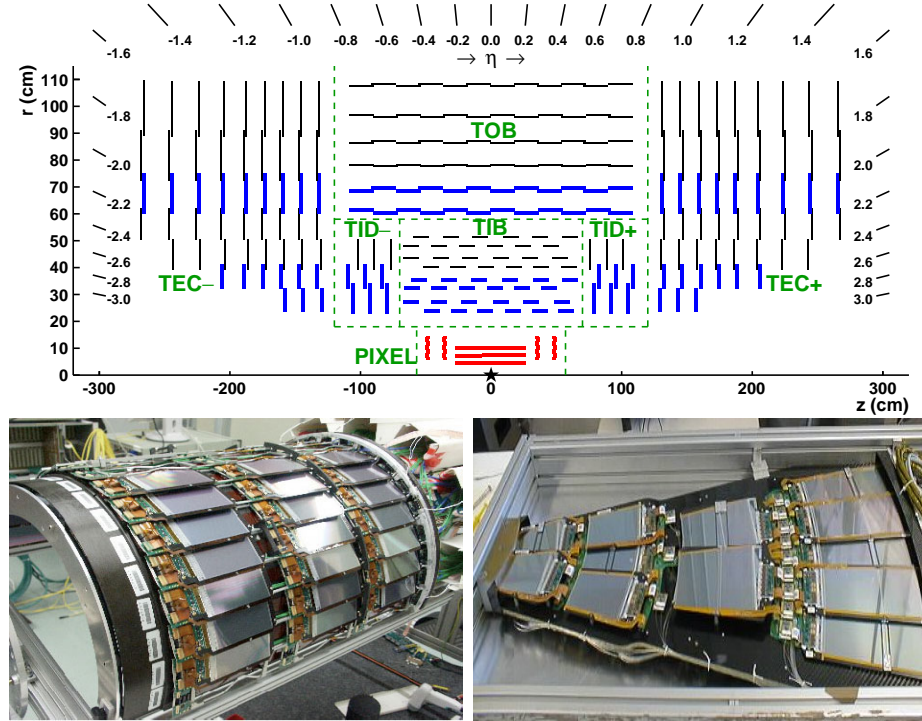


Figure 3.12: Top: CMS Silicon Strip Tracker (SST) schematic view. The SST is composed of the tracker inner barrel (TIB), the tracker inner disks (TID), the tracker outer barrel (TOB) and the tracker endcaps (TEC). Each part is made of silicon strip modules; the modules in blue represent two modules mounted back-to-back and rotated in the plane of the module by a stereo angle of 120 mrad in order to provide a 3-D reconstruction of the hit positions. Bottom: pictures of the TIB (left) and TEC (right) modules [70–72].

1155 The silicon strip tracker (SST) is the second stage in the CMS tracking system. The
 1156 top side of figure 3.12 shows a schematic of the SST. The inner tracker region is com-
 1157 posed of the tracker inner barrel (TIB) and the tracker inner disks (TID) covering the
 1158 region $r < 55$ cm and $|z| < 118$ cm. The TIB is composed of 4 layers while the TID
 1159 is composed of 3 disks at each end. The silicon sensors in the inner tracker are 320
 1160 μm thick, providing a resolution of about 13–38 μm in the $r\phi$ position measurement.
 1161
 1162 The modules indicated in blue in the schematic view of figure 3.12 are two modules

1163 mounted back-to-back and rotated in the plane of the module by a “stereo” angle of
 1164 100 mrad; the hits from these two modules, known as “stereo hits”, are combined to
 1165 provide a measurement of the second coordinate (z in the barrel and r on the disks)
 1166 allowing the reconstruction of hit positions in 3-D.

1167

1168 The outer tracker region is composed of the tracker outer barrel (TOB) and the
 1169 tracker endcaps (TEC). The six layers of the TOB offer coverage in the region $r > 55$
 1170 cm and $|z| < 118$ cm, while the 9 disks of the TEC cover the region $124 < |z| < 282$
 1171 cm. The resolution offered by the outer tracker is about 13-38 μm in the $r\phi$ position
 1172 measurement. The inner four TEC disks use silicon sensors 320 μm thick; those in
 1173 the TOB and the outer three TEC disks use silicon sensors of 500 μm thickness. The
 1174 silicon strips run parallel to the z -axis and the distance between strips varies from 80
 1175 μm in the inner TIB layers to 183 μm in the inner TOB layers; in the endcaps the
 1176 wedge-shaped sensors with radial strips, whose pitch range between 81 μm at small
 1177 radii and 205 μm at large radii.

1178

1179 The whole SST has 15148 silicon modules, 9.3 million silicon strips and cover a total
 1180 active area of about 198 m^2 .

1181 3.3.4 Electromagnetic calorimeter

1182 The CMS electromagnetic calorimeter (ECAL) is designed to measure the energy of
 1183 electrons and photons. It is composed of 75848 lead tungstate crystals which have a
 1184 short radiation length (0.89 cm) and fast response, since 80% of the light is emitted
 1185 within 25 ns; however, they are combined with Avalanche photodiodes (APDs) as
 1186 photodetectors given that crystals themselves have a low light yield ($30\gamma/\text{MeV}$). A

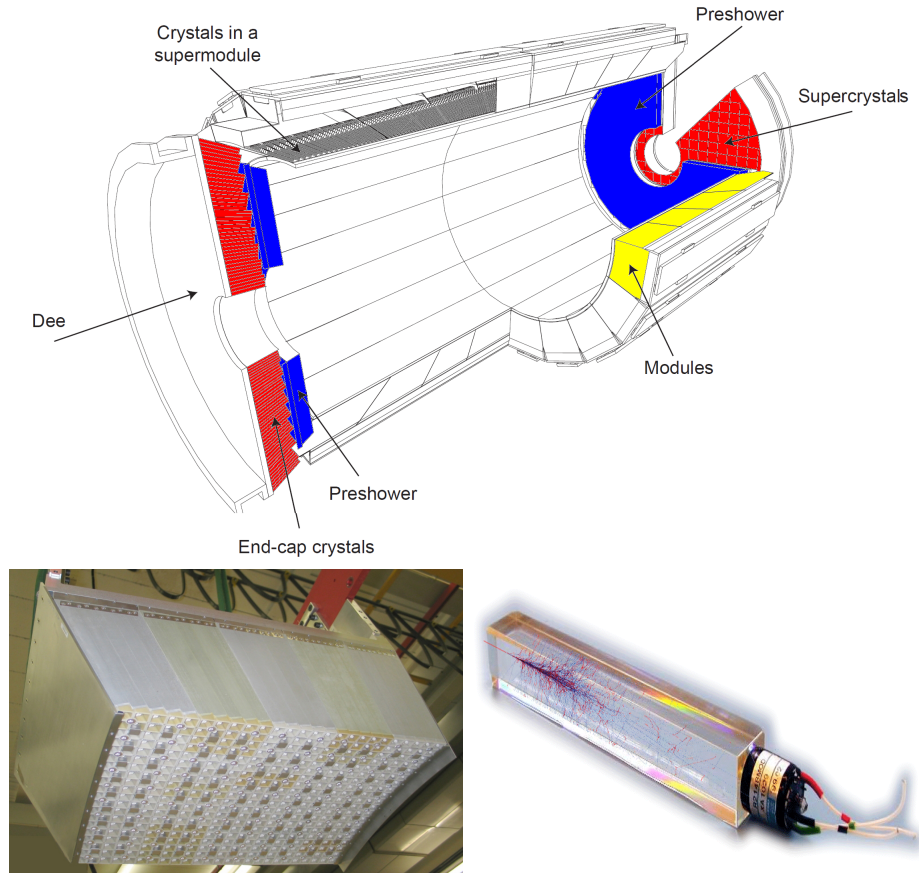


Figure 3.13: Top: CMS ECAL schematic view. Bottom: Module equipped with the crystals (left); ECAL crystal(right).

1187 schematic view of the ECAL is shown in figure 3.13.

1188

1189 Energy is measured by absorbing electrons and photons which generates an electro-
 1190 magnetic “shower”, as seen in bottom right picture of the figure3.13. The ECAL barrel
 1191 (EB) covers the region $|\eta| < 1.479$, using crystals of depth of 23 cm and $2.2 \times 2.2 \text{ cm}^2$
 1192 transverse section; the ECAL endcap (EE) covers the region $1.479 < |\eta| < 3.0$ using
 1193 crystals of depth 22 cm and transverse section of $2.86 \times 2.86 \text{ cm}^2$; the photodetectors
 1194 used are vacuum phototriodes (VPTs). Each EE is divided in two structures called
 1195 “Dees”.

1196

1197 In front of the EE, it is installed the preshower detector (ES) which covers the region
 1198 $1.653 < |\eta| < 2.6$. The ES provides a precise measurement of the position of electro-
 1199 magnetic showers, which allows to distinguish electrons and photons signals from π^0
 1200 decay signals. The ES is composed of a layer of lead absorber followed by a layer of
 1201 plastic scintillators

1202 **3.3.5 Hadronic calorimeter**

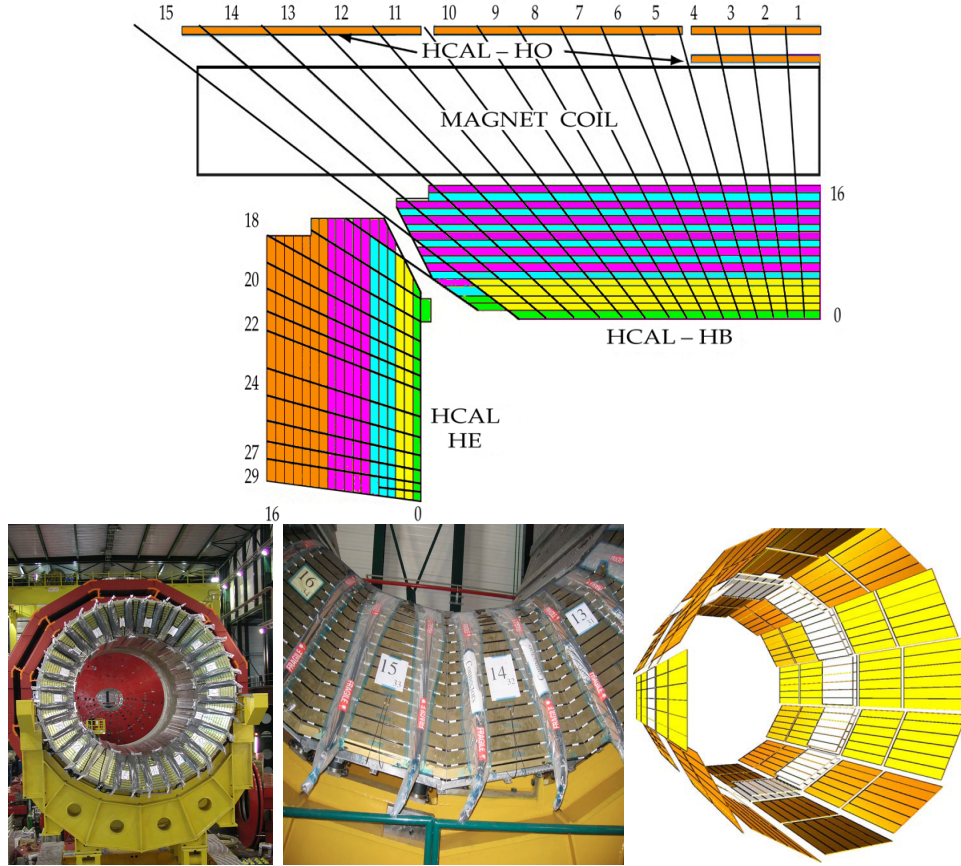


Figure 3.14: Top: CMS HCAL schematic view, the colors indicate the layers that are grouped into the same readout channels. Bottom: picture of a section of the HB; the absorber material is the golden region and scintillators are placed in between the absorber material (left and center). Schematic view of the HO (right). [73, 74]

1203 Hadrons are not absorbed by the ECAL but by the hadron calorimeter (HCAL),
 1204 which is made of a combination of alternating brass absorber layers and silicon photo-
 1205 multiplier(SiPM) layers; therefore, particles passing through the scintillator material
 1206 produce showers, as in the ECAL, as a result of the inelastic scattering of the hadrons
 1207 with the detector material. Since the particles are not absorbed in the scintillator,
 1208 their energy is sampled; therefore the total energy is not measured but estimated,
 1209 which reduce the resolution of the detector. Brass was chosen as the absorber mate-
 1210 rial due to its short interaction length ($\lambda_I = 16.42\text{cm}$) and its non-magnetivity. Figure
 1211 3.14 shows a schematic view of the CMS HCAL.

1212

1213 The HCAL is divided into four sections; the Hadron Barrel (HB), the Hadron Outer
 1214 (HO), the Hadron Endcap (HE) and the Hadron Forward (HF) sections. The HB
 1215 covers the region $0 < |\eta| < 1.4$, while the HE covers the region $1.3 < |\eta| < 3.0$. The HF,
 1216 made of quartz fiber scintillator and steel as absorption material, covers the forward
 1217 region $3.0 < |\eta| < 5.2$. Both the HB and HF are located inside the solenoid. The HO
 1218 is placed outside the magnet as an additional layer of scintillators with the purpose
 1219 of measure the energy tails of particles passing through the HB and the magnet (see
 1220 figure 3.14 top and bottom right). The upgrades made to the HCAL during the
 1221 technical stop 2016-2017 consisted in the replacement of the photo transducer, in
 1222 order to improve the efficiency.

1223 **3.3.6 Superconducting solenoid magnet**

1224 The superconducting magnet installed in the CMS detector is designed to provide
 1225 an intense and highly uniform magnetic field in the central part of the detector. In
 1226 fact, the tracking system takes advantage of the bending power of the magnetic field

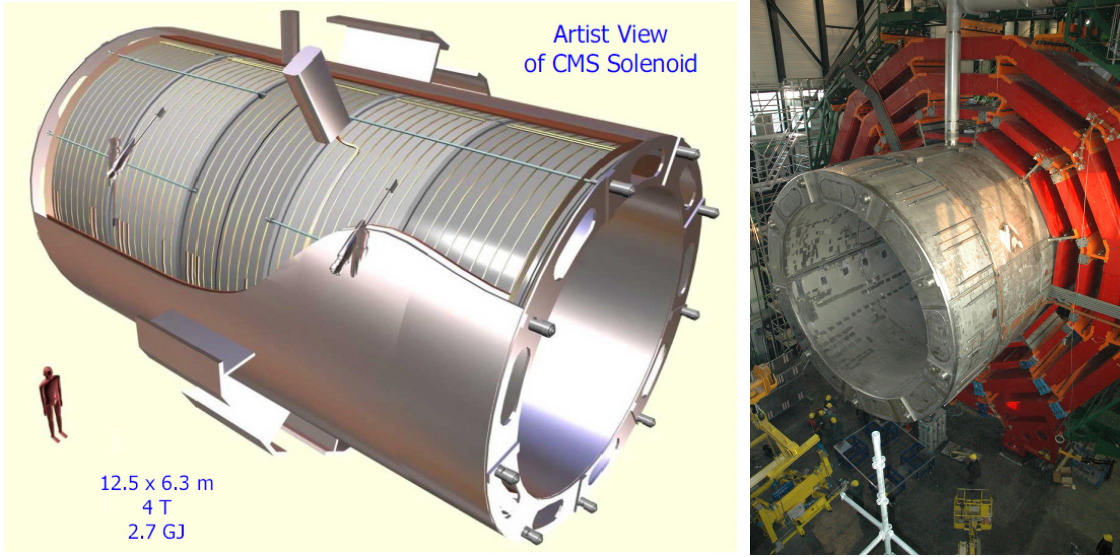


Figure 3.15: Artistic representation of the CMS solenoid magnet(left). The magnet is supported on an iron yoke (right) which also serves as the house of the muon detector and as mechanical support for the whole CMS detector [68].

1227 to measure with precision the momentum of the particles that traverse it; the unam-
 1228 biguous determination of the sign for high momentum muons was a driven principle
 1229 during the design of the magnet. The magnet has a diameter of 6.3 m, a length of 12.5
 1230 m and a cold mass of 220 t; the generated magnetic field reaches a strength of 3.8T.
 1231 Since it is made of Ni-Tb superconducting cable it has to operate at a temperature
 1232 of 4.7 K by using a helium cryogenic system; the current circulating in the cables
 1233 reaches 18800 A under normal running conditions. The left side of figure 3.15 shows
 1234 an artistic view of the CMS magnet, while the right side shows a transverse view of
 1235 the cold mass where the winding structure is visible.

1236
 1237 The yoke (see figure 3.15), composed of 5 barrel wheels and 6 endcap disks made
 1238 of iron, serves not only as the media for magnetic flux return but also provides the
 1239 house for the muon detector system and structural stability to the full detector.

1240 **3.3.7 Muon system**

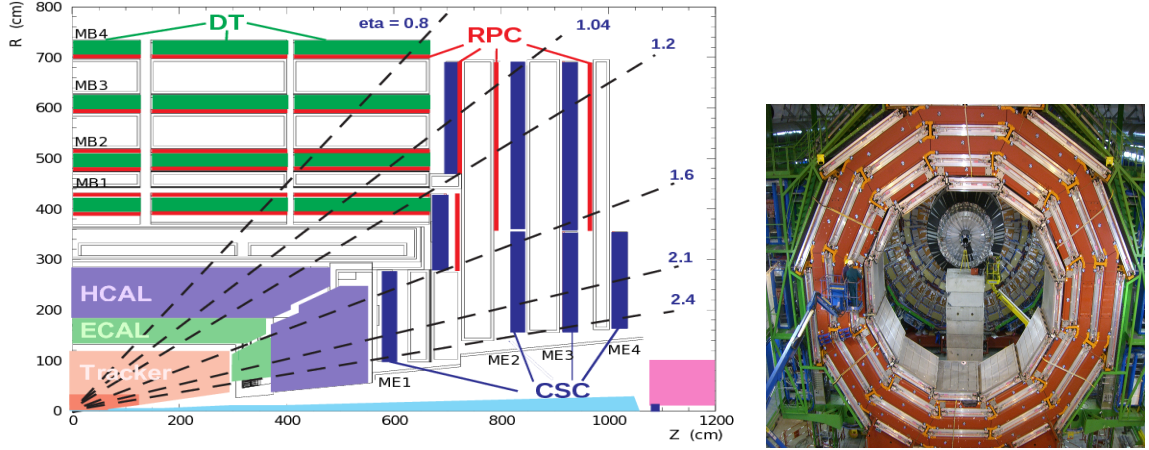


Figure 3.16: Left: CMS muon system schematic view; Right: one of the yoke rings with the muon DTs and RPCs installed; in the back it is possible to see the muon endcap [75].

1241 Muons are the only charged particles able to pass through all the CMS detector due
 1242 to their low ionization energy loss; thus, muons can be separated easily from the
 1243 high amount of particles produced in a pp collision. Also, muons are expected to be
 1244 produced in the decay of several new particles; therefore, a good detection of muons
 1245 was on the leading principles when designing the CMS detector.

1246

1247 The CMS muon detection system is embedded in the return yoke as seen in figure
 1248 3.16. It is composed of three different detector types, the drift tube chambers (DT),
 1249 Cathode strip chambers (CSC), and resistive plate chambers (RPC); DT are located
 1250 in the central region $\eta < 1.2$ arranged in four layers of drift chambers filled with an
 1251 Ar/CO₂ gas mixture.

1252

1253 The muon endcaps are made of CSCs covering the region $\eta < 2.4$ and filled with a
 1254 mixture of Ar/CO₂/CF₄. The reason behind using a different detector type lies on
 1255 the different conditions in the forward region like the high muon rate and high resid-

1256 ual magnetic field.

1257

1258 The third type of detector used in the muon system is a set of four disks of RPCs
 1259 working in avalanche mode. The RPCs provide good spatial and time resolutions.
 1260 The track of $high - p_T$ muon candidates is built combining information from the
 1261 tracking system and the signal from up to six RPCs and four DT chambers.

1262 **3.3.8 CMS trigger system**

1263 Under normal conditions, CMS expects pp collisions every 25 ns i.e. an interaction
 1264 rate of 40 MHz for which it is not possible to store the recorded data in full. In order
 1265 to handle this high event rate data, an online event selection, known as triggering, is
 1266 performed; triggering reduce the event rate to 100 Hz for storage and further offline
 1267 analysis.

1268

1269 The trigger system starts with a reduction of the event rate to 100 kHz in the so-called
 1270 “level 1 trigger (L1)”. L1 is based on dedicated programmable hardware like Field
 1271 Programmable Gate Arrays (FPGAs) and Application Specific Integrated Circuits
 1272 (ASICs), partly located in the detector itself; another portion is located in the CMS
 1273 under-ground cavern. Hit patterns information from the muon chambers and the en-
 1274 ergy deposits in the calorimeter are used to decide if an event is accepted or rejected,
 1275 according to selection requirements previously defined, which reflect the interesting
 1276 physics processes. Figure 3.17 shows the L1 trigger architecture

1277

1278 The second stage in the trigger system is called “ high-level trigger (HLT)”; events
 1279 accepted by L1 are passed to HLT in order to make an initial reconstruction of them.

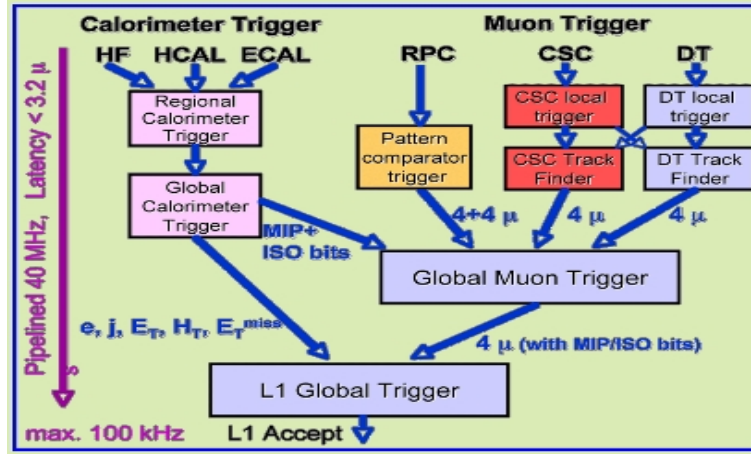


Figure 3.17: CMS Level-1 trigger architecture [76].

1280 HLT is software based and runs on a dedicated server farm, using selection algo-
 1281 rithms and high-level object definitions; the event rate at HLT is reduced to 100 Hz.

1282 The first HLT stage takes information from the muon detectors and the calorimeters
 1283 to make the initial object reconstruction; in the next HLT stage, information from
 1284 the pixel and strip detectors is used to do first fast-tracking and then full tracking
 1285 online. This initial object reconstruction is used in further steps of the trigger system.

1286

1287 Events and preliminary reconstructed physics objects from HLT are sent to be fully
 1288 reconstructed at the CERN computing center. Again, the pixel detector information
 1289 provides high-quality seeds for the track reconstruction algorithm offline, primary ver-
 1290 tex reconstruction, electron and photon identification, muon reconstruction, τ iden-
 1291 tification, and b-tagging. After full reconstruction, data sets are made available for
 1292 offline analyses.

1293

1294 During the 2016-2017 technical stop, the L1 system was updated in order to improve
 1295 the physics object identification by improving the algorithms and accounting for the
 1296 increasing pile-up scenario.

1297 3.3.9 CMS computing

1298 After the data, coming from the experiment, are processed at several levels, they have
 1299 to be stored and made available for further analysis; in order to cope all the tasks
 1300 implied in the offline data processing, like transfer, simulation, reconstruction and
 1301 reprocessing, among others, a big computing power is required. The CMS computing
 1302 system is based on the distributed architecture concept, where users of the system
 1303 and physical computer centers are distributed worldwide and interconnected by high-
 1304 speed networks.

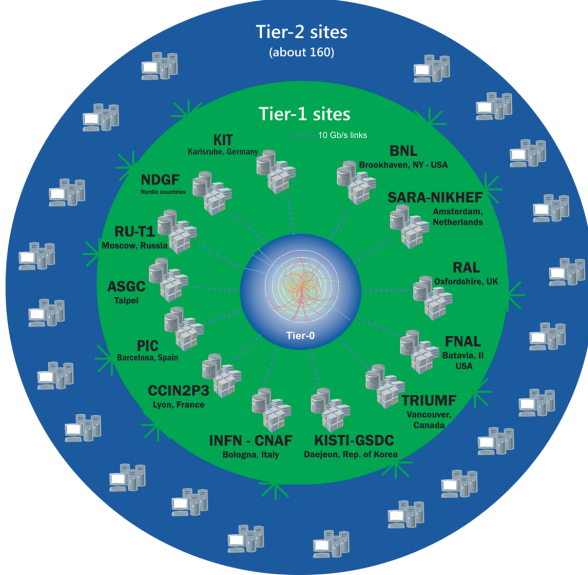


Figure 3.18: WLCG structure. The primary computer centers (Tier-0) are located at CERN (data center) and at the Wigner datacenter in Budapest. Tier-1 is composed of 13 centers and Tier-2 is composed of about 160 centers. [77].

1305 The worldwide LHC computing grid (WLCG) is the mechanism used to provide that
 1306 distributed environment. WLCG is a tiered structure connecting computing centers
 1307 around the world, which provides the necessary storage and computing facilities. The
 1308 primary computing centers of the WLCG are located at the CERN and the Wigner
 1309 datacenter in Budapest and are known as Tier-0 as shown in figure 3.18. The main

1310 responsibilities for each tier level are [77]

1311 • **Tier-0:** initial reconstruction of recorded events and storage of the resulting
1312 datasets, the distribution of raw data to the Tier-1 centers.

1313 • **Tier-1:** provide storage capacity, support for the Grid, safe-keeping of a pro-
1314 portional share of raw and reconstructed data, large-scale reprocessing and safe-
1315 keeping of corresponding output, generation of simulated events, distribution
1316 of data to Tier 2s, safe-keeping of a share of simulated data produced at these
1317 Tier 2s.

1318 • **Tier-2:** store sufficient data and provide adequate computing power for specific
1319 analysis tasks, provide analysis requirements and proportional share of simu-
1320 lated event production and reconstruction.

1321 Aside from the general computing strategy to manage the huge amount of data pro-
1322 duced by experiments, CMS uses a framework to perform a variety of processing,
1323 selection and analysis tasks. The central concept of the CMS data model referred to
1324 as “event data model” (EDM) is the “Event”; therefore, an event is the unit that con-
1325 tains the information from a single bunch crossing as well as any data derived from
1326 that information like the reconstructed objects, the details under which additional
1327 data are derived.

1328

1329 Events are passed as the input to the “physics modules” that obtain information from
1330 them and create new one; for instance, “event data producers” add new data into the
1331 events, “analyzers” produce an information summary from an event set, “filters” per-
1332 form selection and triggering.

1333

1334 CMS uses several event formats with different levels of detail and precision

1335 • **Raw format:** events in this format contain the full recorded information from
1336 the detector as well as trigger decision and other metadata. An extended version
1337 of raw data is used to store information from the CMS Monte Carlo simulation
1338 tools. Raw data are stored permanently, occupying about 2MB/event

1339 • **RECO format:** events in this format correspond to raw data that have been
1340 submitted to reconstruction algorithms like primary and secondary vertex re-
1341 construction, particle ID, track-finding. RECO events contain physical objects
1342 and all the information used to reconstruct them; average size is about 0.5
1343 MB/event.

1344 • **AOD format:** Analysis Object Data (AOD) is the data format used in the
1345 physics analyses given that it contains the parameters describing the high-level
1346 physics objects in addition to enough information to allow a kinematic refitting if
1347 needed. AOD events are filtered versions of the RECO events to which skimming
1348 or other kind processes have been applied. Requires about 100 kB/event.

1349 • **Non-event data** are data needed to interpret and reconstruct events. Some
1350 of the non-event data used by CMS contains information about the detector
1351 contraction and condition data like calibrations, alignment, and detector status.

1352 Figure 3.19 shows the data flow scheme between CMS detector and hardware tiers.

1353 The whole collection of software built as a framework is referred to as “CMSSW”. This
1354 framework provides the services needed by the simulation, calibration and alignment,
1355 and reconstruction modules that process event data, so that physicists can perform
1356 analysis. The CMSSW event processing model is composed of one executable, called

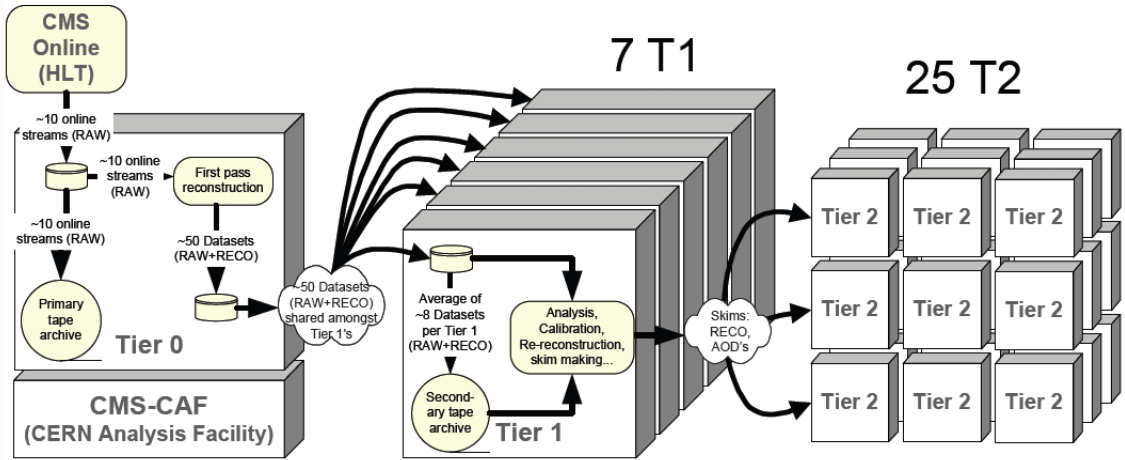


Figure 3.19: Data flow from CMS detector through hardware Tiers.

1357 cmsRun, and several plug-in modules which contains all the tools (calibration, recon-
 1358 struction algorithms) needed to process an event. The same executable is used for
 1359 both detector and Monte Carlo data [78].

1360 **Chapter 4**

1361 **Event generation, simulation and
1362 reconstruction**

1363 The process of analyzing the data recorded by the CMS experiment involves several
1364 stages where the data are processed in order to interpret the information provided by
1365 all the detection systems; in those stages the particles produced after the pp collision
1366 are identified by reconstructing their trajectories and measuring their features. In
1367 addition, the SM provides a set of predictions that have to be compared with the
1368 experimental results; however, in most of the cases, theoretical predictions are not
1369 directly comparable to experimental results due to the diverse source of uncertainties
1370 introduced by the experimental setup and theoretical approximations among others.

1371

1372 The strategy to face these conditions consist in using statistical methods implemented
1373 in computational algorithms to produce numerical results that can be contrasted with
1374 the experimental results. These computational algorithms are commonly known as
1375 Monte Carlo (MC) methods and, in the case of particle physics, they are designed to
1376 apply the SM rules and produce predictions about the physical observables measured

1377 in the experiments. Since particle physics is governed by quantum mechanics principles,
 1378 predictions are not allowed for single events; therefore, a high number of events
 1379 are “generated” and predictions are produced in the form of statistical distributions
 1380 for the observables. Effects of the detector presence are included in the predictions
 1381 by introducing simulations of the detector itself.

1382

1383 This chapter presents a description of the event generation strategy and the tools
 1384 used to perform the detector simulation and physics objects reconstruction. A comprehensive
 1385 review on event generators for LHC physics can be found in reference [79]
 1386 on which this chapter is based.

1387 4.1 Event generation

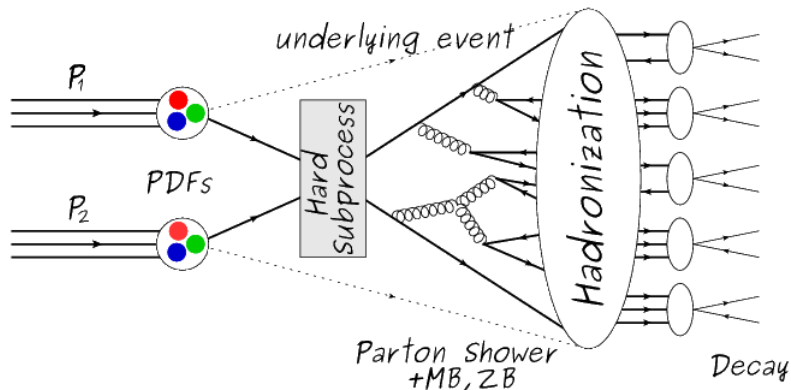


Figure 4.1: Event generation process. In the first step, the PDF of the colliding particles is considered so the specific interaction is described. The actual interaction is generated in the hard subprocess; the cross section of the process is calculated from the matrix element connecting the initial and final states. The parton shower describes the evolution of the partons from the hard subprocess according to the DGLAP equations. At this step the underlying event and PU effects are included in the generation. The resulting partons from the parton shower are recombined to form hadrons in the hadronization step; most of them are unstable, therefore, their decays are also generated in agreement to the known branching ratios. Modified from reference [80].

1388 The event generation is intended to create events that mimic the behavior of actual
 1389 events produced in the collisions; they obey a sequence of steps from the particles colli-
 1390 sion hard process to the decay process into the final state particles. Figure 4.1 shows
 1391 an schematic view of the event generation process; the fact that the full process can
 1392 be treated as several independent steps is based on the QCD factorization theorem.

1393

1394 Generation starts by taking into account the PDFs of the incoming particles. Event
 1395 generators offer the option to chose from several PDF sets depending on the partic-
 1396 ular process under simulation¹; in the following pp collisions will be considered. The
 1397 *hard subprocess* describes the actual interaction between partons from the incoming
 1398 protons; it is represented by the matrix element connecting the initial and final states
 1399 of the interaction. Normally, the matrix element can be written as a sum over Feyn-
 1400 man diagrams and consider interferences between terms in the summation. During
 1401 the generation of the hard subprocess, the production cross section is calculated.

1402

1403 The order to which the cross section is calculated depends on the order of the Feyn-
 1404 man diagrams involved in the calculation; therefore, radiative corrections are included
 1405 by considering a higher order Feynman diagrams where QCD radiation dominates.
 1406 Currently, cross sections calculated to LO do not offer a satisfactory description of the
 1407 processes, i.e., the results are only reliable for the shape of distributions; therefore,
 1408 NLO calculations have to be performed with the implication that the computing time
 1409 needed is highly increased.

1410

1411 The final parton content of the hard subprocess is subjected to the *parton shower*
 1412 which generates the gluon radiation. Parton shower evolves the partons; i.e., glouns

¹ Tool in Reference [81] allows to plot different PDF sets under customizable conditions.

1413 split into quark-antiquark pairs and quarks of enough energy radiate gluons giving rise
 1414 to further parton multiplication, following the DGLAP (Dokshitzer-Gribov-Lipatov-
 1415 Altarelli-Parisi) equations. Showering continues until the energy scale is low enough
 1416 to reach the non-perturbative limit.

1417

1418 In the simulation of LHC processes that involve b quarks like the single top quark or
 1419 Higgs associated production, it is needed to consider that the b quark is heavier than
 1420 the proton; in this sense, the QCD interaction description is made in two different
 1421 schemes [82]

1422 • four-flavor (4F) scheme. b quarks appears only in the final state because they
 1423 are heavier than the proton and therefore they can be produced only from the
 1424 splitting of a gluon into pairs or singly in association with a t quark in high
 1425 energy-scale interactions. During the simulation, the b -PDFs are set to zero
 1426 because it cannot be part of the proton. Calculation in this scheme are more
 1427 complicated due to the presence of the second b quark but the full kinematics is
 1428 considered already at LO and therefore the accuracy of the description is better.

1429 • five-flavor (5F) scheme. b quarks are considered massless, therefore they can
 1430 appear in both initial and final states since it can now be part of the proton; thus,
 1431 during the simulation b -PDFs are not set to zero. In this scheme, calculations
 1432 are simpler than in the 4F scheme and possible logarithmic divergences are
 1433 absorbed by the PDFs through the DGLAP evolution.

1434 In this thesis, the tHq events are generated using the 4F scheme in order to reduce
 1435 uncertainties, while the tHW events are generated using the 5F scheme to eliminate
 1436 LO interference with the $t\bar{t}H$ process [48].

1437

1438 Partons involved in the pp collision are the focus of the simulation, however, the rest
 1439 of the partons inside the incoming protons are also affected because the remnants are
 1440 colored objects; also, multiple parton interactions can occurs. The hadronization of
 1441 the remnants and multiple parton interactions are known as “underlying event” and
 1442 it has to be included in the simulation. In addition, multiple pp collisions in the same
 1443 bunch crossing (pile-up mentioned in 3.2) occurs, actually in two forms

- 1444 • *in-time PU* which refers to multiple pp collision in the bunch crossing but that
 1445 are not considered as primary vertices.
- 1446 • *Out-of-time PU* which refers to overlapping pp collisions from consecutive bunch
 1447 crossings; this can occurs due to the time-delays in the detection systems where
 1448 information from one bunch crossing is assigned to the next or previous one.

1449 While the underlying event effects are included in generation using generator-specific
 1450 tools, PU effects are added to the generation by overlying Minimum-bias (MB) and
 1451 Zero-bias (ZB) events to the generated events. MB events are inelastic events selected
 1452 by using a loose (minimum bias) trigger with as little bias as possible, therefore ac-
 1453 cepting a large fraction of the overall inelastic event; ZB events correspond to random
 1454 events recorded by the detector when collisions are likely. MB model in-time PU and
 1455 ZB model out-of-time PU.

1456

1457 The next step in the generation process is called “hadronization”. Since particles
 1458 with a net color charge are not allowed to exits isolated, they have recombine to form
 1459 bound states. This is precisely the process by which the partons resulting from the
 1460 parton shower arrange themselves as color singlets to form hadrons. At this step, the
 1461 energy-scale is low and the strong coupling constant is large, therefore hadronization
 1462 process is non-perturbative and phenomenological model are used to describe the

1463 parton’s evolution. Most of the baryons and mesons produced in the hadronization
 1464 are unstable and hence they will decay in the detector.

1465

1466 The last step in the generation process corresponds to the decay of the unstable
 1467 particles generated during hadronization; it is also simulated in the hadronization
 1468 step, based on the known branching ratios.

1469 4.2 Monte Carlo Event Generators.

1470 The event generation described in the previous section has been implemented in
 1471 several software packages for which a brief description is given.

- 1472 • **PYTHIA 8.** It is a program designed to perform the generation of high en-
 1473 ergy physics events which describe the collisions between particles such as elec-
 1474 trons, protons. Several theories and models are implemented in it, in order to
 1475 describe physical aspects like hard and soft interaction, parton distributions,
 1476 initial and final-state parton showers, multiple parton interactions, beam rem-
 1477 nants, hadronization² and particle decay. Thanks to extensive testing, several
 1478 optimized parametrizations known as “tunnings” have been defined in order
 1479 to improve the description of actual collisions to a high degree of precision; for
 1480 analysis at $\sqrt{s} = 13$ TeV, the underline event CUETP8M1 tune is employed [84].
 1481 The calculation of the matrix element is performed at LO which is not enough
 1482 for the current required level of precision; therefore, pythia is often used for
 1483 parton shower, hadronization, decays, while other event generators are used to
 1484 generate the matrix element at NLO.

² based in the Lund string model [83]

1485 • **MadGraph5_aMC@NLO.** MadGraph is a matrix element generator which
 1486 calculates the amplitudes for all contributing Feynman diagrams of a given pro-
 1487 cess but does not provide a parton shower while MC@NLO incorporate NLO
 1488 QCD matrix elements consistently into a parton shower framework; thus, Mad-
 1489 Graph5_aMC@NLO, as a merger of the two event generators MadGraph5 and
 1490 aMC@NLO, is an event generator capable to calculate tree-level and NLO cross
 1491 sections and perform the matching of those with the parton shower. It is one
 1492 of the most frequently used matrix element generators; however, it has as par-
 1493 ticular feature the presence of negative event weights which reduce the number
 1494 of events used to reproduce the the properties of the objects generated [85].

1495

1496 • **POWHEG.** It is an NLO matrix element generator where the hardest emis-
 1497 sion of color charged particles is generated in such a way that the negative event
 1498 weights issue of MadGraph5_aMC@NLO is overcome; however, the method re-
 1499 quires an interface with p_T -ordered parton shower or a parton shower generator
 1500 where this highest emission can be vetoed in order to avoid double counting of
 1501 this highest-energetic emission. PYTHIA is a commonly matched to POWHEG
 1502 event generator [86].

1503 Events resulting from the whole generation process are known as MC events.

1504 4.3 CMS detector simulation.

1505 After generation, MC events contain the physics of the collisions but they are not
 1506 ready to be compared to the events recorded by the experiment since these recorded
 1507 events correspond to the response of the detection systems to the interaction with the

1508 particles traversing them. The simulation of the CMS detector have to be applied on
1509 top of the event generation; it is simulated with Geant4, a MC toolkit for the simula-
1510 tion of particles passing though matter which is also able to simulates the electronic
1511 signals that would be measured by all detectors inside CMS.

1512

1513 The simulation takes the generated particles contained in the MC events as input,
1514 makes them to pass through the simulated geometry, and models physics processes
1515 that particles experience during their passage through matter. The full set of results
1516 from particle-matter interactions correspond to the simulated hit which contains in-
1517 formation about the energy loss, momentum, position. Particles of the input event
1518 are called “primary”, while the particles originating from GEANT4-modeled interac-
1519 tions of a primary particle with matter are called a “secondary”. Simulated hits are
1520 the input of subsequent modules that emulate the response of the detector readout
1521 system and triggers. The output from the emulated detection systems and triggers is
1522 known as digitization [87, 88].

1523

1524 The modeling of the CMS detector corresponds to the accurate modeling of the inter-
1525 action among particles, the detector material and the magnetic field. This simulation
1526 procedure includes the following standard steps

- 1527 • Modeling of the Interaction Region.
- 1528 • Modeling of the particle passage through the hierarchy of volumes that compose
1529 CMS detector and of the accompanying physics processes.
- 1530 • Modeling of the effect of multiple interactions per beam crossing and/or the
1531 effect of events overlay (Pile-Up simulation).

1532 • Modeling of the detector’s electronics response, signal shape, noise, calibration
 1533 constants (digitization).

1534 In addition to the full simulation which implies a detailed detector simulation, a
 1535 faster simulations (FastSim) have been developed, that may be used where much
 1536 larger statistics are required. In FastSim, detector material effects are parametrized
 1537 and included in the hits; those hits are used as input of the same higher-level algo-
 1538 rithms³ used to analyze the recorded events. In this way, comparisons between fast
 1539 and full simulations can be performed [90].

1540

1541 After the full detector simulation, the output events can be directly compared with
 1542 events actually recorded in the CMS detector. The collection of MC events that re-
 1543 produce the expected physics for a given process are known as MC samples.

1544

1545 **4.4 Event reconstruction.**

1546 CMS requires an offline first-pass full reconstruction of express line and all online
 1547 streams in quasi-realtime, which produces new reconstructed objects called RECO
 1548 data.

1549 particle flow algorithm, vertexing , muon reco, electron reco, photon and hadron
 1550 reco, jets reco, anti-kt algorithm, jet energy corrections, btagging, MET

1551 The Tier-0 offline reconstruction step processes all RAW events from the online
 1552 system following an adjustable set of priorities (the express-line, by definition has
 1553 very high priority). This step creates new higher-level physics objects such as tracks,

³ track fitting, calorimeter clustering, b tagging, electron identification, jet reconstruction and calibration, trigger algorithms which will be considered in the next sections

1554 vertices, and jets. These may improve or extend the set produced in the HLT pro-
1555 cessing step. It must run with minimal delay compared to the online in order to
1556 provide rapid feedback to the online operations, for example, identifying detector or
1557 trigger problems which can then be rectified dynamically during the same LHC fill.
1558 The offline reconstruction will normally perform the same reconstruction steps for
1559 each stream, with the possible exception of specialised calibration streams. In this
1560 way we ensure that they are all useful in principle for all analysis groups. We apply
1561 this same rule to later re-processings of the data, 2-3 times per year we expect to
1562 bring all datasets into consistent status as to applied calibrations and algorithms, as
1563 described below.

1564 **4.5 MVA methods, NN, BDT, boosting,
1565 overtraining, variable ranking**

1566 **4.6 statistical inference, likelihood
1567 parametrization**

1568 **4.7 nuisance paraeters**

1569 **4.8 exclusion limits**

1570 **4.9 asymptotic limits**

¹⁵⁷¹ **Chapter 5**

¹⁵⁷² **Search for production of a Higgs**

¹⁵⁷³ **boson and a single top quark in**

¹⁵⁷⁴ **multilepton final states in pp**

¹⁵⁷⁵ **collisions at $\sqrt{s} = 13$ TeV**

¹⁵⁷⁶ **5.1 Introduction**

¹⁵⁷⁷ Dont forget to mention previous constrains to ct check reference ?? and references

¹⁵⁷⁸ <https://link.springer.com/content/pdf/10.1007%2FJHEP01>

¹⁵⁷⁹ A. Azatov, R. Contino and J. Galloway, \rightarrow IJModel-Independent Bounds on a

¹⁵⁸⁰ Light Higgs, \rightarrow JHEP 1204 (2012) 127 [arXiv:1202.3415 [hep-ph]].

¹⁵⁸¹ J. R. Espinosa, C. Grojean, M. Muhlleitner and M. Trott, \rightarrow IJFingerprinting

¹⁵⁸² Higgs Suspects at the LHC, \rightarrow JHEP 1205 (2012) 097 [arXiv:1202.3697 [hep-ph]].

¹⁵⁸³ This chapter present the search for the associated production of a Higgs boson and

¹⁵⁸⁴ a single top quark events with three leptons in the final state, targeting Higgs decay

1585 modes to WW , ZZ , and $\tau\tau$. The analysis uses the 13 TeV dataset produced in 2016,
 1586 corresponding to an integrated luminosity of 35.9fb^{-1} . It is based on and expands
 1587 previous analyses at 8 TeV [91, 92] and searches for associated production of $t\bar{t}$ and
 1588 Higgs in the same channel [93], and complements searches in other decay channels
 1589 targeting $H \rightarrow b\bar{b}$ [94].

1590 As showed in section 2.4, the cross section of the associated production of a Higgs
 1591 boson and a single top quark (tHq) process is driven by a destructive interference of
 1592 two contributions (see Figure 5.1), where the Higgs couples to either the W boson or
 1593 the top quark. Any deviation from the standard model (SM) in the Higgs coupling
 1594 structure could therefore lead to a large enhancement of the cross section, making
 1595 this analysis sensitive to such deviations. A second process, where the Higgs and
 1596 top quark are accompanied by a W boson (tHW) has similar behavior, albeit with a
 1597 weaker interference pattern.

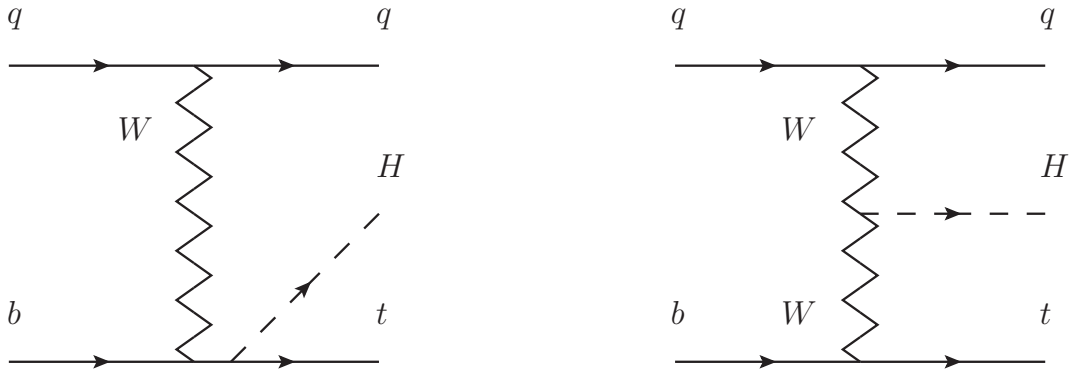


Figure 5.1: The two leading-order diagrams of tHq production.

1598 We selects events with three leptons and a b tagged jet in the final state. The tHq
 1599 signal contribution is then determined in a fit of the observed data to two multivariate
 1600 classifier outputs, each trained to discriminate against one of the two dominant back-
 1601 grounds of events with non-prompt leptons from $t\bar{t}$ and of associated production of $t\bar{t}$

1602 and vector bosons ($t\bar{t}W$, $t\bar{t}Z$). The fit result is then used to set an upper limit on the
 1603 combined $t\bar{t}H$, tHq and tHW production cross section, as a function of the relative
 1604 coupling strengths of Higgs and top quark and Higgs and W boson, respectively.

1605 5.2 Data and MC Samples

1606 The data considered in this analysis were collected by the CMS experiment dur-
 1607 ing 2016 and correspond to a total integrated luminosity of 35.9fb^{-1} . Only periods
 1608 when the CMS magnet was on were considered when selecting the data samples, that
 1609 corresponds to the 23 Sep 2016 (Run B to G) and PromptReco (Run H) versions
 1610 of the datasets. The MC samples used in this analysis correspond to the RunI-
 1611 ISummer16MiniAODv2 campaign produced with CMSSW 80X. The two signal sam-
 1612 ples (for tHq and tHW) were produced with MG5_aMC@NLO (version 5.222), in
 1613 leading-order mode, and are normalized to next-to-leading-order cross sections,
 1614 see Tab. 5.1. Each sample is generated with a set of event weights corresponding to
 1615 different values of κ_t and κ_V couplings as shown in Tab. 5.2.

1616 5.2.1 Full 2016 dataset and MC samples

Sample	σ [pb]	BF
/THQ_Hincl_13TeV-madgraph-pythia8_TuneCUETP8M1/	0.7927	0.324
/THW_Hincl_13TeV-madgraph-pythia8_TuneCUETP8M1/	0.1472	1.0

Table 5.1: Signal samples and their cross section and branching fraction used in this analysis. See Ref. [95] for more details.

1617 Different MC generators were used to generate the background processes. The
 1618 dominant sources ($t\bar{t}$, $t\bar{t}W$, $t\bar{t}Z$, $t\bar{t}H$) were produced using AMC@NLO interfaced
 1619 to PYTHIA8, and are scaled to NLO cross sections. Other processes are simulated

		<i>tHq</i>		<i>tHW</i>		
κ_V	κ_t	sum of weights	cross section [pb]	sum of weights	cross section [pb]	LHE weights
1.0	-3.0	35.700022	2.991	11.030445	0.6409	LHEweight_wgt[446]
1.0	-2.0	20.124298	1.706	5.967205	0.3458	LHEweight_wgt[447]
1.0	-1.5	14.043198	1.205	4.029093	0.2353	LHEweight_wgt[448]
1.0	-1.25	11.429338	0.9869	3.208415	0.1876	LHEweight_wgt[449]
1.0	-1.0		0.7927		0.1472	
1.0	-0.75	7.054998	0.6212	1.863811	0.1102	LHEweight_wgt[450]
1.0	-0.5	5.294518	0.4723	1.339886	0.07979	LHEweight_wgt[451]
1.0	-0.25	3.818499	0.3505	0.914880	0.05518	LHEweight_wgt[452]
1.0	0.0	2.627360	0.2482	0.588902	0.03881	LHEweight_wgt[453]
1.0	0.25	1.719841	0.1694	0.361621	0.02226	LHEweight_wgt[454]
1.0	0.5	1.097202	0.1133	0.233368	0.01444	LHEweight_wgt[455]
1.0	0.75	0.759024	0.08059	0.204034	0.01222	LHEweight_wgt[456]
1.0	1.0	0.705305	0.07096	0.273617	0.01561	LHEweight_wgt[457]
1.0	1.25	0.936047	0.0839	0.442119	0.02481	LHEweight_wgt[458]
1.0	1.5	1.451249	0.1199	0.709538	0.03935	LHEweight_wgt[459]
1.0	2.0	3.335034	0.2602	1.541132	0.08605	LHEweight_wgt[460]
1.0	3.0	10.516125	0.8210	4.391335	0.2465	LHEweight_wgt[461]
1.5	-3.0	45.281492	3.845	13.426212	0.7825	LHEweight_wgt[462]
1.5	-2.0	27.606715	2.371	7.809713	0.4574	LHEweight_wgt[463]
1.5	-1.5	20.476088	1.784	5.594971	0.3290	LHEweight_wgt[464]
1.5	-1.25	17.337465	1.518	4.635978	0.2749	LHEweight_wgt[465]
1.5	-1.0	14.483302	1.287	3.775902	0.2244	LHEweight_wgt[466]
1.5	-0.75	11.913599	1.067	3.014744	0.1799	LHEweight_wgt[467]
1.5	-0.5	9.628357	0.874	2.352505	0.1410	LHEweight_wgt[468]
1.5	-0.25	7.627574	0.702	1.789184	0.1081	LHEweight_wgt[469]
1.5	0.0	5.911882	0.5577	1.324946	0.08056	LHEweight_wgt[470]
1.5	0.25	4.479390	0.4365	0.959295	0.05893	LHEweight_wgt[471]
1.5	0.5	3.331988	0.3343	0.692727	0.04277	LHEweight_wgt[472]
1.5	0.75	2.469046	0.2558	0.525078	0.03263	LHEweight_wgt[473]
1.5	1.0	1.890565	0.2003	0.456347	0.02768	LHEweight_wgt[474]
1.5	1.25	1.596544	0.1689	0.486534	0.02864	LHEweight_wgt[475]
1.5	1.5	1.586983	0.1594	0.615638	0.03509	LHEweight_wgt[476]
1.5	2.0	2.421241	0.2105	1.170602	0.06515	LHEweight_wgt[477]
1.5	3.0	7.503280	0.5889	3.467546	0.1930	LHEweight_wgt[478]
0.5	-3.0	27.432685	2.260	8.929074	0.5136	LHEweight_wgt[479]
0.5	-2.0	13.956013	1.160	4.419093	0.2547	LHEweight_wgt[480]
0.5	-1.5	8.924438	0.7478	2.757611	0.1591	LHEweight_wgt[481]
0.5	-1.25	6.835341	0.5726	2.075247	0.1204	LHEweight_wgt[482]
0.5	-1.0	5.030704	0.4273	1.491801	0.08696	LHEweight_wgt[483]
0.5	-0.75	3.510528	0.2999	1.007273	0.05885	LHEweight_wgt[484]
0.5	-0.5	2.274811	0.1982	0.621663	0.03658	LHEweight_wgt[485]
0.5	-0.25	1.323555	0.1189	0.334972	0.01996	LHEweight_wgt[486]
0.5	0.0	0.656969	0.06223	0.147253	0.008986	LHEweight_wgt[487]
0.5	0.25	0.274423	0.02830	0.058342	0.003608	LHEweight_wgt[488]
0.5	0.5	0.176548	0.01778	0.068404	0.003902	LHEweight_wgt[489]
0.5	0.75	0.363132	0.03008	0.177385	0.009854	LHEweight_wgt[490]
0.5	1.0	0.834177	0.06550	0.385283	0.02145	LHEweight_wgt[491]
0.5	1.25	1.589682	0.1241	0.692099	0.03848	LHEweight_wgt[492]
0.5	1.5	2.629647	0.2047	1.097834	0.06136	LHEweight_wgt[493]
0.5	2.0	5.562958	0.4358	2.206057	0.1246	LHEweight_wgt[494]
0.5	3.0	14.843102	1.177	5.609519	0.3172	LHEweight_wgt[495]

Table 5.2: κ_V and κ_t combinations generated for the two signal samples and their NLO cross sections. The *tHq* cross section is multiplied by the branching fraction of the enforced leptonic decay of the top quark (0.324). See also Ref. [95].

Sample	σ [pb]
TTWJetsToLNu_TuneCUETP8M1_13TeV-amcatnloFXFX-madspin-pythia8	0.2043
TTZToLLNuNu_M-10_TuneCUETP8M1_13TeV-amcatnlo-pythia8	0.2529
tthJetToNonbb_M125_13TeV_amcatnloFXFX_madspin_pythia8_mWCutfix /store/cmst3/group/susy/gpetrucc/13TeV/u/TTLL_m1to10_L0_NoMS_for76X/	0.2151 0.0283
WGToLNuG_TuneCUETP8M1_13TeV-madgraphMLM-pythia8	585.8
ZGTo2LG_TuneCUETP8M1_13TeV-amcatnloFXFX-pythia8	131.3
TGJets_TuneCUETP8M1_13TeV_amcatnlo_madspin_pythia8	2.967
TGJets_TuneCUETP8M1_13TeV_amcatnlo_madspin_pythia8	2.967
TTGJets_TuneCUETP8M1_13TeV-amcatnloFXFX-madspin-pythia8	3.697
WpWpJJ_EWK_QCD_TuneCUETP8M1_13TeV-madgraph-pythia8	0.03711
ZZZ_TuneCUETP8M1_13TeV-amcatnlo-pythia8	0.01398
WWZ_TuneCUETP8M1_13TeV-amcatnlo-pythia8	0.1651
WZZ_TuneCUETP8M1_13TeV-amcatnlo-pythia8	0.05565
WW_DoubleScattering_13TeV-pythia8	1.64
tZq_ll_4f_13TeV-amcatnlo-pythia8_TuneCUETP8M1	0.0758
ST_tWll_5f_LO_13TeV-MadGraph-pythia8	0.01123
TTTT_TuneCUETP8M1_13TeV-amcatnlo-pythia8	0.009103
WZTo3LNu_TuneCUETP8M1_13TeV-powheg-pythia8	4.4296
ZZTo4L_13TeV_powheg_pythia8	1.256
TTJets_SingleLeptFromTbar_TuneCUETP8M1_13TeV-madgraphMLM-pythia8	182.1754
TTJets_SingleLeptFromT_TuneCUETP8M1_13TeV-madgraphMLM-pythia8	182.1754
TTJets_DiLept_TuneCUETP8M1_13TeV-madgraphMLM-pythia8	87.3
DYJetsToLL_M-10to50_TuneCUETP8M1_13TeV-amcatnloFXFX-pythia8	18610
DYJetsToLL_M-50_TuneCUETP8M1_13TeV-madgraphMLM-pythia8	6024
WJetsToLNu_TuneCUETP8M1_13TeV-amcatnloFXFX-pythia8	61526.7
ST_tW_top_5f_inclusiveDecays_13TeV-powheg-pythia8_TuneCUETP8M1	35.6
ST_tW_antitop_5f_inclusiveDecays_13TeV-powheg-pythia8_TuneCUETP8M1	35.6
ST_t-channel_4f_leptonDecays_13TeV-amcatnlo-pythia8_TuneCUETP8M1	70.3144
ST_t-channel_antitop_4f_leptonDecays_13TeV-powheg-pythia8_TuneCUETP8M1	26.2278
ST_s-channel_4f_leptonDecays_13TeV-amcatnlo-pythia8_TuneCUETP8M1	3.68064
WWTo2L2Nu_13TeV-powheg	10.481

Table 5.3: List of background samples used in this analysis (CMSSW 80X). In the first section of the table are listed the samples of the processes for which we use the simulation to extract the final yields and shapes, in the second section the samples of the processes we will estimate from data. The MC simulation is used to design the data driven methods and derive the associated systematics.

Sample	σ [pb]
ttWJets_13TeV_madgraphMLM	0.6105
ttZJets_13TeV_madgraphMLM	0.5297/0.692

Table 5.4: Leading-order $t\bar{t}W$ and $t\bar{t}Z$ samples used in the signal BDT training.

1620 using POWHEG interfaced to PYTHIA, or bare PYTHIA (see table 5.3 and [93]
1621 for more details).

Three lepton and Four lepton
HLT_DiMu9_Ele9_CaloIdL_TrackIdL_v*
HLT_Mu8_DiEle12_CaloIdL_TrackIdL_v*
HLT_TripleMu_12_10_5_v*
HLT_Ele16_Ele12_Ele8_CaloIdL_TrackIdL_v*
HLT_Mu23_TrkIsoVVL_Ele8_CaloIdL_TrackIdL_IsoVL_v*
HLT_Mu23_TrkIsoVVL_Ele8_CaloIdL_TrackIdL_IsoVL_DZ_v*
HLT_Mu8_TrkIsoVVL_Ele23_CaloIdL_TrackIdL_IsoVL_v*
HLT_Mu8_TrkIsoVVL_Ele23_CaloIdL_TrackIdL_IsoVL_DZ_v*
HLT_Ele23_Ele12_CaloIdL_TrackIdL_IsoVL_DZ_v*
HLT_Mu17_TrkIsoVVL_Mu8_TrkIsoVVL_DZ_v*
HLT_Mu17_TrkIsoVVL_TkMu8_TrkIsoVVL_DZ_v*
HLT_IsoMu22_v*
HLT_IsoTkMu22_v*
HLT_IsoMu22_eta2p1_v*
HLT_IsoTkMu22_eta2p1_v*
HLT_IsoMu24_v*
HLT_IsoTkMu24_v*
HLT_Ele27_WPTight_Gsf_v*
HLT_Ele25_eta2p1_WPTight_Gsf_v*
HLT_Ele27_eta2p1_WPLoose_Gsf_v*

Table 5.5: Table of high-level triggers that we consider in the analysis.

1622 5.2.2 Triggers

1623 We consider online-reconstructed events triggered by one, two, or three leptons.
 1624 Single-lepton triggers are included to boost the acceptance of events where the p_T of
 1625 the sub-leading lepton falls below the threshold of the double-lepton triggers. Ad-
 1626 ditionally, by including double-lepton triggers in the ≥ 3 lepton category, as well
 1627 as single-lepton triggers in all categories, we increase the efficiency, considering the
 1628 logical “or” of the trigger decisions of all the individual triggers in a given category.
 1629 Tab. 5.5 shows the lowest-threshold non-prescaled triggers present in the High-Level
 1630 Trigger (HLT) menus for both Monte-Carlo and data in 2016.

1631 5.2.2.1 Trigger efficiency scale factors

1632 The efficiency of events to pass the trigger is measured in simulation (trivially using
 1633 generator information) and in the data (using event collected by an uncorrelated

Category	Scale Factor
ee	1.01 ± 0.02
e μ	1.01 ± 0.01
$\mu\mu$	1.00 ± 0.01
3l	1.00 ± 0.03

Table 5.6: Trigger efficiency scale factors and associated uncertainties, shown here rounded to the nearest percent.

1634 MET trigger). Small differences between the data and MC efficiencies are corrected
 1635 by applying scale factors as shown in Tab. 5.6. The exact procedure and control plots
 1636 are documented in [96] for the current analysis.

1637 5.3 Object Identification and event selection

1638 5.3.1 Jets and b tagging

1639 The analysis uses anti- k_t (0.4) particle-flow (PF) jets, corrected for charged hadrons
 1640 not coming from the primary vertex (charged hadron subtraction), and having jet
 1641 energy corrections (`Summer16_23Sep2016V3`) applied as a function of the jet E_T and
 1642 η . Jets are only considered if they have a transverse energy above 25GeV.

1643 In addition, they are required to be separated from any lepton candidates passing
 1644 the fakeable object selections (see Tables 5.7 and 5.8) by $\Delta R > 0.4$.

1645 The loose and medium working points of the CSV b-tagging algorithm are used to
 1646 identify b jets. Data/simulation differences in the b tagging performance are corrected
 1647 by applying per-jet weights to the simulation, dependent on the jet p_T , eta, b tagging
 1648 discriminator, and flavor (from simulation truth) [97]. The per-event weight is taken
 1649 as the product of the per-jet weights, including those of the jets associated to the
 1650 leptons. More details can be found in the corresponding $t\bar{t}H$ documentation [93, 96].

1651 **5.3.2 Lepton selection**

Cut	Loose	Fakeable object	Tight
$ \eta < 2.4$	✓	✓	✓
p_T	$> 5\text{GeV}$	$> 15\text{GeV}$	$> 15\text{GeV}$
$ d_{xy} < 0.05 \text{ (cm)}$	✓	✓	✓
$ d_z < 0.1 \text{ (cm)}$	✓	✓	✓
$\text{SIP}_{3D} < 8$	✓	✓	✓
$I_{\text{mini}} < 0.4$	✓	✓	✓
is Loose Muon	✓	✓	✓
jet CSV	—	< 0.8484	< 0.8484
is Medium Muon	—	—	✓
tight-charge	—	—	✓
lepMVA > 0.90	—	—	✓

Table 5.7: Requirements on each of the three muon selections. In the cases where the cut values change between the selections, those values are listed in the table. Otherwise, whether the cut is applied is indicated. For the two p_T^{ratio} and CSV rows, the cuts marked with a † are applied to leptons that fail the lepton MVA cut, while the loose cut value is applied to those that pass the lepton MVA cut.

1652 The lepton reconstruction and selection is identical to that used in the $t\bar{t}H$ mul-
 1653 tilepton analysis, as documented in Refs. [93, 96]. For details on the reconstruction
 1654 algorithms, isolation, pileup mitigation, and a description of the lepton MVA discrim-
 1655 inator and validation plots thereof, we refer to that document since they are out of
 1656 the scope of this thesis. Three different selections are defined both for the electron
 1657 and muon object identification: the *Loose*, *Fakeable Object*, and *Tight* selection. As
 1658 described in more detail later, these are used for event level vetoes, the fake rate
 1659 estimation application region, and the final signal selection, respectively. The p_T of
 1660 fakeable objects is defined as $0.85 \times p_T(\text{jet})$, where the jet is the one associated to the
 1661 lepton object. This mitigates the dependence of the fake rate on the momentum of
 1662 the fakeable object and thereby improves the precision of the method.

1663 Tables 5.7 and 5.8 list the full criteria for the different selections of muons and
 1664 electrons.

Cut	Loose	Fakeable Object	Tight
$ \eta < 2.5$	✓	✓	✓
p_T	$> 7\text{GeV}$	$> 15\text{GeV}$	$> 15\text{GeV}$
$ d_{xy} < 0.05 \text{ (cm)}$	✓	✓	✓
$ d_z < 0.1 \text{ (cm)}$	✓	✓	✓
$\text{SIP}_{3D} < 8$	✓	✓	✓
$I_{\text{mini}} < 0.4$	✓	✓	✓
MVA ID $> (0.0, 0.0, 0.7)$	✓	✓	✓
$\sigma_{in\eta} < (0.011, 0.011, 0.030)$	—	✓	✓
$\text{H/E} < (0.10, 0.10, 0.07)$	—	✓	✓
$\Delta\eta_{in} < (0.01, 0.01, 0.008)$	—	✓	✓
$\Delta\phi_{in} < (0.04, 0.04, 0.07)$	—	✓	✓
$-0.05 < 1/E - 1/p < (0.010, 0.010, 0.005)$	—	✓	✓
p_T^{ratio}	—	$> 0.5^\dagger / -$	—
jet CSV	—	$< 0.3^\dagger / < 0.8484$	< 0.8484
tight-charge	—	—	✓
conversion rejection	—	—	✓
Number of missing hits	< 2	$== 0$	$== 0$
lepMVA > 0.90	—	—	✓

Table 5.8: Criteria for each of the three electron selections. In cases where the cut values change between selections, those values are listed in the table. Otherwise, whether the cut is applied is indicated. In some cases, the cut values change for different η ranges. These ranges are $0 < |\eta| < 0.8$, $0.8 < |\eta| < 1.479$, and $1.479 < |\eta| < 2.5$ and the respective cut values are given in the form (value₁, value₂, value₃).

1665 5.3.3 Lepton selection efficiency

1666 Efficiencies of reconstruction and selecting loose leptons are measured both for muons
 1667 and electrons using a tag and probe method on both data and MC, using $Z \rightarrow \ell^+ \ell^-$.
 1668 Corresponding scale factors are derived from the ratio of efficiencies and applied to the
 1669 selected These. Events are produced for the leptonic SUSY analyses using equivalent
 1670 lepton selections and recycled for the $t\bar{t}H$ analysis as well as for this analysis. The
 1671 efficiencies of applying the tight selection as defined in Tables 5.7 and 5.8, on the
 1672 loose leptons are determined again by using a tag and probe method on a sample of
 1673 DY-enriched events. They are documented for the $t\bar{t}H$ analysis in Ref. [96] and are
 1674 exactly equivalent for this analysis.

1675 5.4 Background predictions

1676 The modeling of reducible and irreducible backgrounds in this analysis uses the exact
 1677 methods, analysis code, and ROOT trees used for the $t\bar{t}H$ multilepton analysis. We
 1678 give a brief description of the methods and refer to the documentation of that analysis
 1679 in Refs. [93, 96] for any details.

1680 The backgrounds in three-lepton final states can be split in two broad categories:
 1681 irreducible backgrounds with genuine prompt leptons (i.e. from on-shell W and Z
 1682 boson decays); and reducible backgrounds where at least one of the leptons is “non-
 1683 prompt”, i.e. produced within a hadronic jet, either a genuine lepton from heavy
 1684 flavor decays, or simply mis-reconstructed jets.

1685 Irreducible backgrounds can be reliably estimated directly from Monte-Carlo sim-
 1686 ulated events, using higher-order cross sections or data control regions for the overall
 1687 normalization. This is done in this analysis for all backgrounds involving prompt lep-
 1688 tons: $t\bar{t}W$, $t\bar{t}Z$, $t\bar{t}H$, WZ , ZZ , $W^\pm W^\pm qq$, $t\bar{t}t\bar{t}$, tZq , tZW , WWW , WWZ , WZZ ,
 1689 ZZZ .

1690 Reducible backgrounds, on the other hand, are not well predicted by simulation,
 1691 and are estimated using data-driven methods. In the case of non-prompt leptons, a
 1692 fake rate method is used, where the contribution to the final selection is estimated by
 1693 extrapolating from a sideband (or “application region”) with a looser lepton definition
 1694 (the fakeable object definitions in Tabs. 5.7 and 5.8) to the signal selection. The tight-
 1695 to-loose ratios (or “fake rates”) are measured in several background dominated data
 1696 events with dedicated triggers, subtracting the residual prompt lepton contribution
 1697 using MC. Non-prompt leptons in our signal regions are predominantly produced in $t\bar{t}$
 1698 events, with a much smaller contribution, from Drell–Yan production. The systematic
 1699 uncertainty on the normalization of the non-prompt background estimation is on the

1700 order of 50%, and thereby one of the dominant limitations on the performance of
 1701 multilepton analyses in general and this analysis in particular. It consists of several
 1702 individual sources, such as the result of closure tests of the method using simulated
 1703 events, limited statistics in the data control regions due to necessary prescaling of
 1704 lepton triggers, and the uncertainty in the subtraction of residual prompt leptons
 1705 from the control region.

1706 The fake background where the leptons pass the looser selection are weighted
 1707 according to how many of them fail the tight criteria. Events with a single failing
 1708 lepton are weighted with the factor $f/(1-f)$ for the estimate to the tight selection
 1709 region, where f is the fake rate. Events with two failing leptons are given the negative
 1710 weight $-f_i f_j / (1 - f_i)(1 - f_j)$, and for three leptons the weight is positive and equal
 1711 to the product of $f/(1-f)$ factor evaluated for each failing lepton.

1712 Figures 5.2 show the distributions of some relevant kinematic variables, normalized
 1713 to the cross section of the respective processes and to the integrated luminosity.

1714 5.5 Signal discrimination

1715 The tHq signal is separated from the main backgrounds using a boosted decision
 1716 tree (BDT) classifier, trained on simulated signal and background events. A set of
 1717 discriminating variables are given as input to the BDT which produces a output
 1718 distribution maximizing the discrimination power. Table 5.9 lists the input variables
 1719 used while Figures 5.3 show their distributions for the relevant signal and background
 1720 samples, for the three lepton channel. Two BDT classifiers are trained for the two
 1721 main backgrounds expected in the analysis: events with prompt leptons from $t\bar{t}W$ and
 1722 $t\bar{t}Z$ (also referred to as $t\bar{t}V$), and events with non-prompt leptons from $t\bar{t}$. The datasets
 1723 used in the training are the tHq signal (see Tab. 5.1), and LO MADGRAPH samples

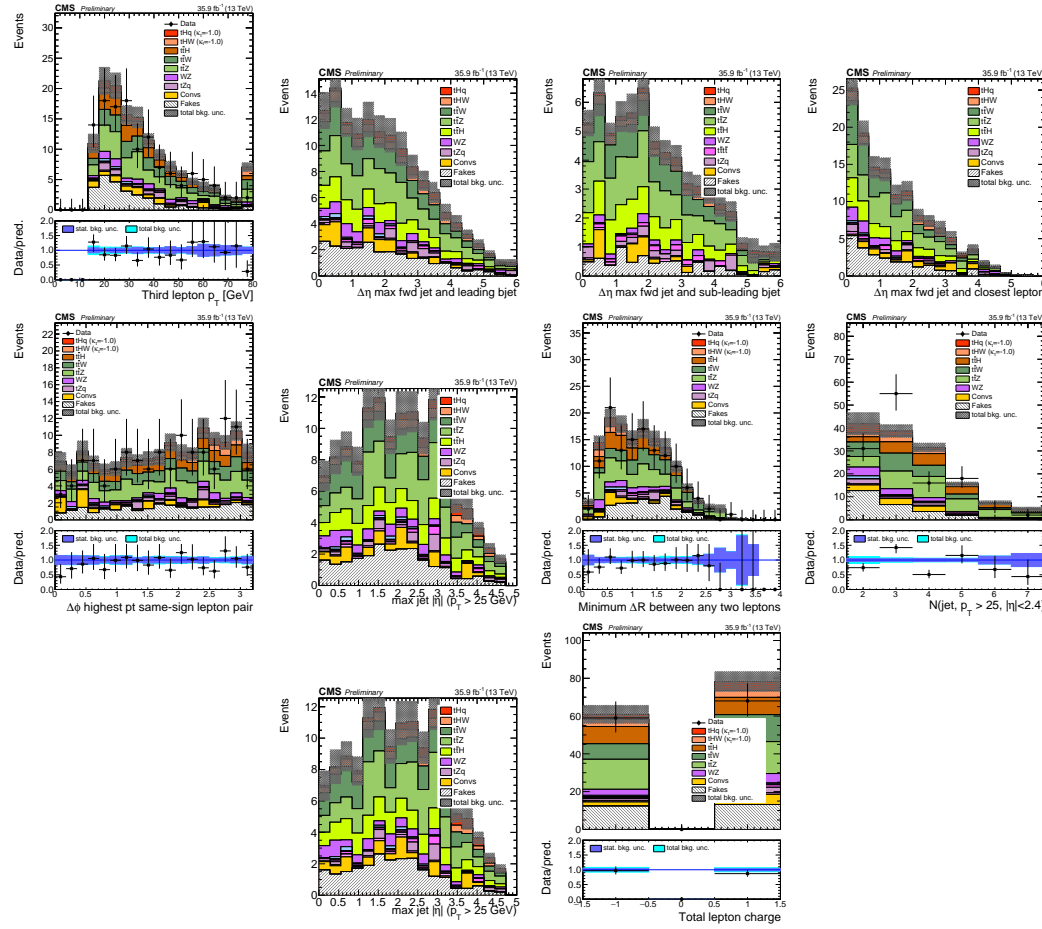


Figure 5.2: Distributions of input variables to the BDT for signal discrimination, three lepton channel, normalized to their cross section and to 35.9fb^{-1} .

of $t\bar{t}W$ and $t\bar{t}Z$, in an admixture proportional to their respective cross sections (see Tab. 5.4).

The MVA analysis consist of two stages: first a “training” where the MVA method is trained to discriminate between simulated signal and background events, then a “test” stage where the trained algorithm is used to classify different events from the samples. The sample is obtained from a pre-selection (see Tab. ?? with pre-selection cuts). Figures 5.4 show the input variables distributions as seen by the MVA algorithm. Note that in contrast to the distributions in Fig. 5.3 only the main backgrounds ($t\bar{t}$ from simulation, $t\bar{t}V$) are included.

Variable name	Description
nJet25	Number of jets with $p_T > 25$ GeV, $ \eta < 2.4$
MaxEtaJet25	Maximum $ \eta $ of any (non-CSV-loose) jet with $p_T > 25$ GeV
totCharge	Sum of lepton charges
nJetEta1	Number of jets with $ \eta > 1.0$, non-CSV-loose
detaFwdJetBJet	$\Delta\eta$ between forward light jet and hardest CSV loose jet
detaFwdJet2BJet	$\Delta\eta$ between forward light jet and second hardest CSV loose jet (defaults to -1 in events with only one CSV loose jet)
detaFwdJetClosestLep	$\Delta\eta$ between forward light jet and closest lepton
dphiHighestPtSSPair	$\Delta\phi$ of highest p_T same-sign lepton pair
minDRll	minimum ΔR between any two leptons
Lep3Pt/Lep2Pt	p_T of the 3 rd lepton (2 nd for ss2l)

Table 5.9: MVA input discriminating variables

1733 Note that splitting the training in two groups reveals that some variables show
 1734 opposite behavior for the two background sources; potentially screening the discrimi-
 1735 nation power if they were to be used in a single discriminant. For some other variables
 1736 the distributions are similar in both background cases.

1737 From table 5.9, it is clear that the input variables are correlated to some extend.
 1738 These correlations play an important role for some MVA methods like the Fisher
 1739 discriminant method in which the first step consist of performing a linear transfor-
 1740 mation to an phase space where the correlations between variables are removed. In
 1741 case a boosted decision tree (BDT) method however, correlations do not affect the
 1742 performance. Figure 5.6 show the linear correlation coefficients for signal and back-
 1743 ground for the two training cases (the signal values are identical by construction). As
 1744 expected, strong correlations appears for variables related to the forward jet activity.
 1745 Same trend is seen in case of the same sign dilepton channel in Figure ??.

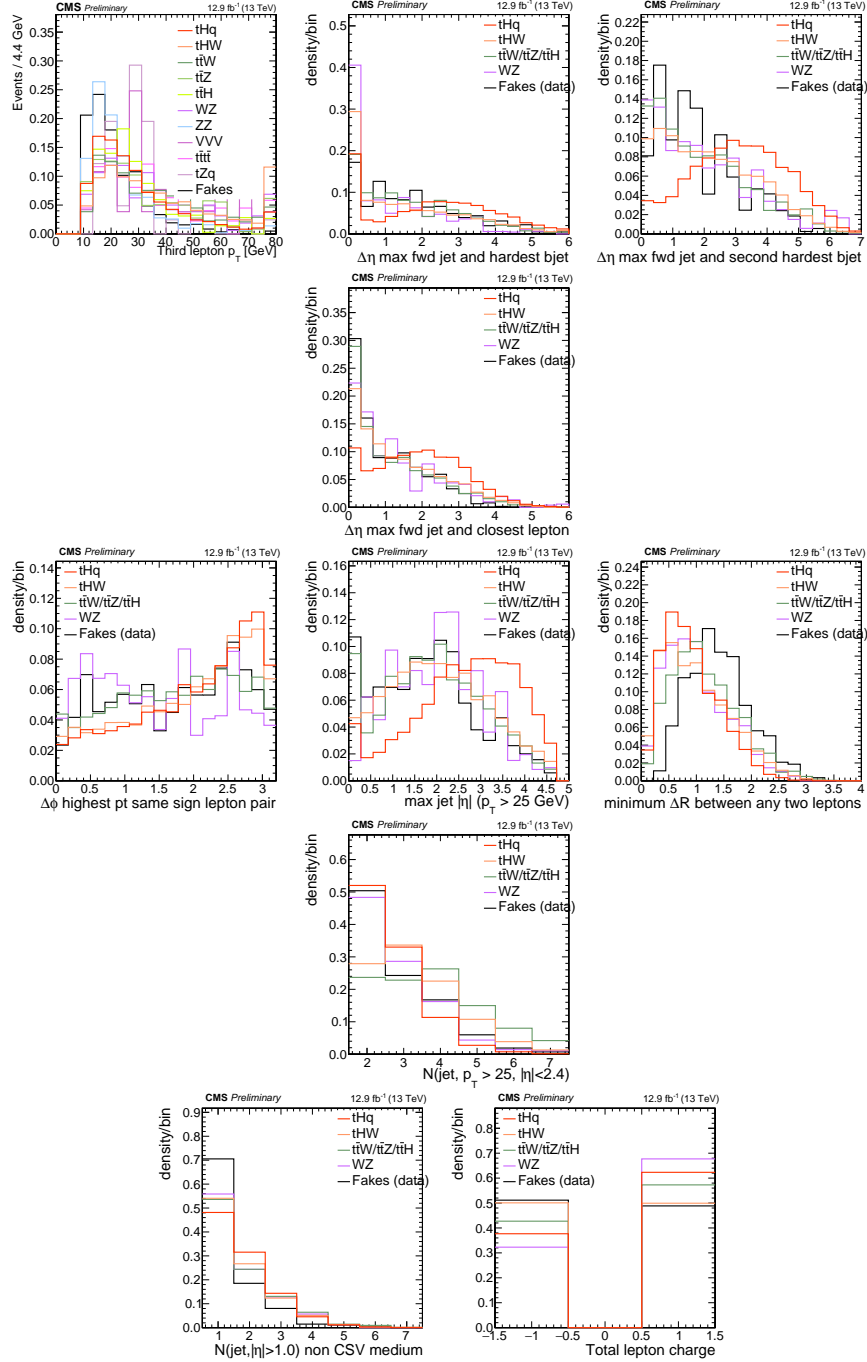


Figure 5.3: Distributions of input variables to the BDT for signal discrimination, three lepton channel.

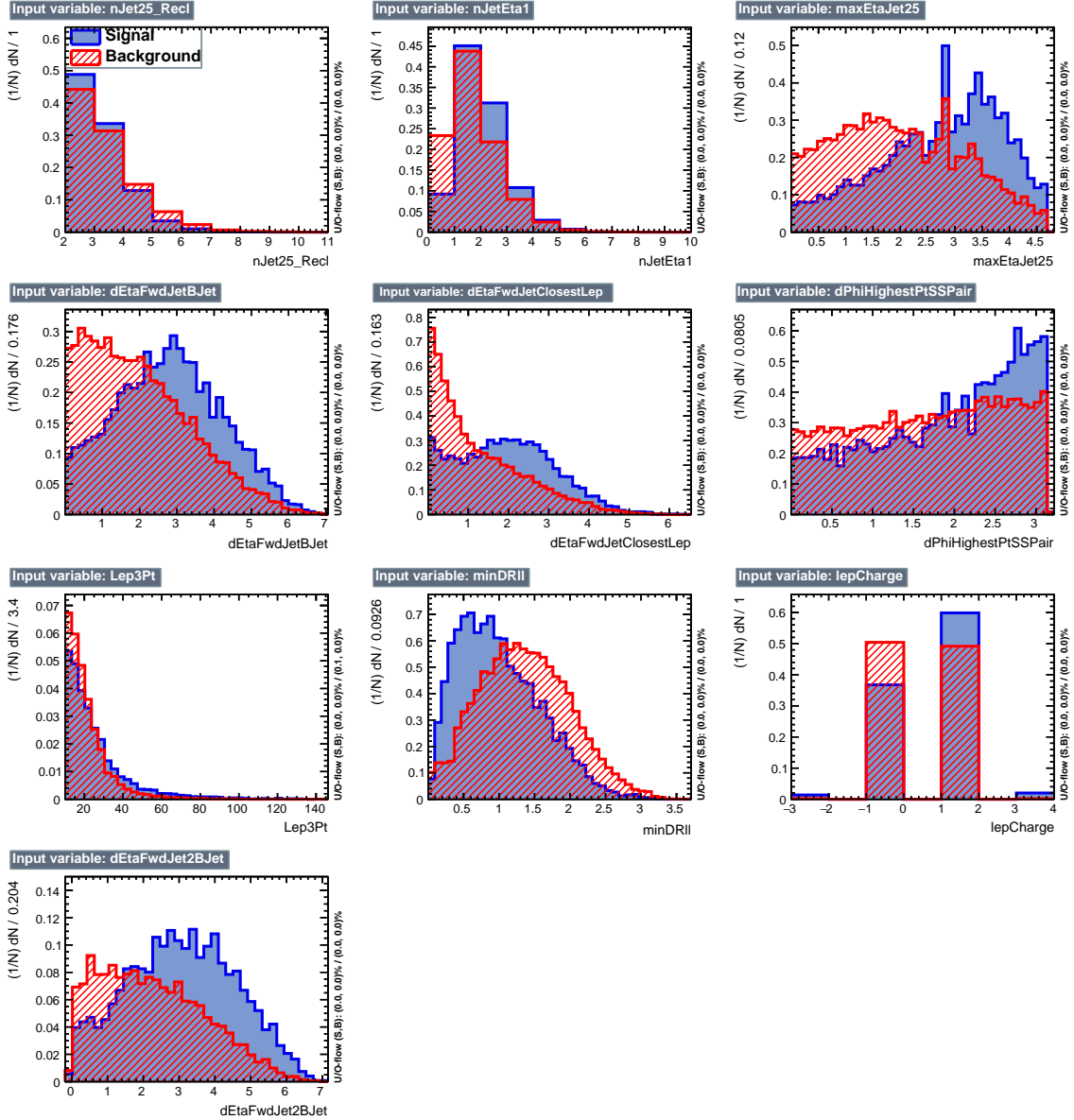


Figure 5.4: BDT inputs as seen by TMVA (signal, in blue, is tHq , background, in red, is $t\bar{t}$) for the three lepton channel, discriminated against $t\bar{t}$ (fakes) background.

1746 5.5.1 Classifiers response

1747 Several MVA algorithms were evaluated to determine the most appropriate method
 1748 for this analysis. The plots in Fig. 5.7 (top) show the background rejection as a
 1749 function of the signal efficiency for $t\bar{t}$ and $t\bar{t}V$ trainings (ROC curves) for the different

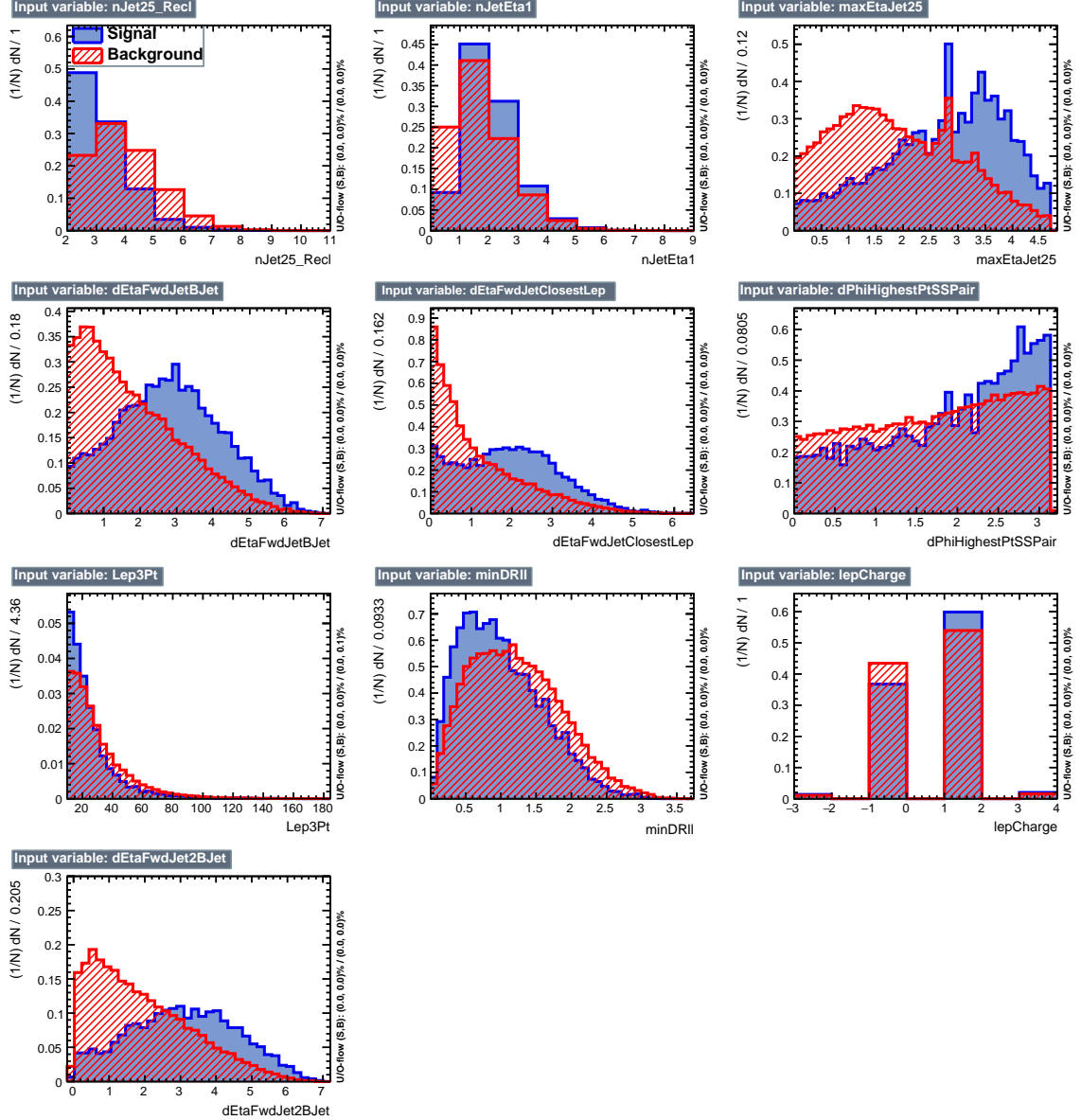


Figure 5.5: BDT inputs as seen by TMVA (signal, in blue, is tHq , background, in red, is $t\bar{t}W+t\bar{t}Z$) for the three lepton channel, discriminated against $t\bar{t}V$ background.

1750 algorithms that were evaluated.

1751 In both cases the gradient boosted decision tree (“BDTA_GRAD”) classifier offers
 1752 the best results, followed by an adaptive BDT classifier (“BDTA”). The BDTA_GRAD
 1753 classifier output distributions for signal and backgrounds are shown on the bottom of
 1754 Fig. 5.7. As expected, a good discrimination power is obtained using default discrim-

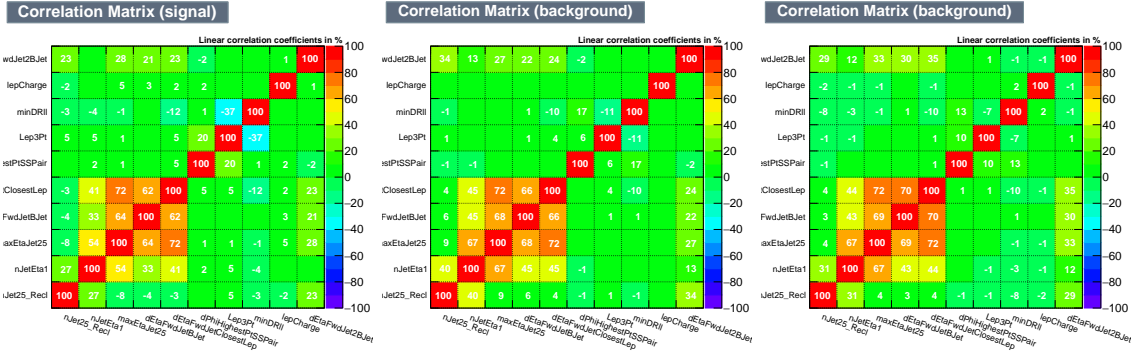


Figure 5.6: Signal (left), $t\bar{t}$ background (middle), and $t\bar{t}V$ background (right.) correlation matrices for the input variables in the TMVA analysis for the three lepton channel.

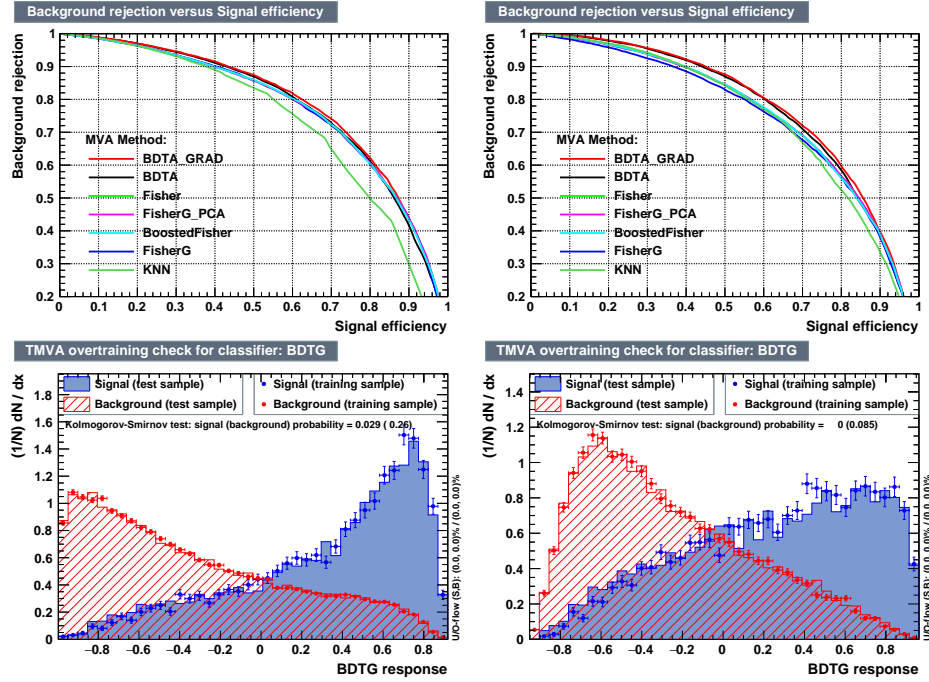


Figure 5.7: Top: background rejection vs signal efficiency (ROC curves) for various MVA classifiers (top) in the three lepton channel against $t\bar{t}V$ (left) and $t\bar{t}$ (right). Bottom: classifier output distributions for the gradient boosted decision trees, for training against $t\bar{t}V$ (left) and against $t\bar{t}$ (right).

1755 inator parameter values, with minimal overtraining. TMVA provides a ranking of the
 1756 input variables by their importance in the classification process, shown in Tab. 5.10.
 1757 The TMVA settings used in the BDT training are shown in Tab. 5.11.

ttbar training			ttV training		
Rank	Variable	Importance	Variable	Importance	
1	minDRll	1.329e-01	dEtaFwdJetBJet	1.264e-01	
2	dEtaFwdJetClosestLep	1.294e-01	Lep3Pt	1.224e-01	
3	dEtaFwdJetBJet	1.209e-01	maxEtaJet25	1.221e-01	
4	dPhiHighestPtSSPair	1.192e-01	dEtaFwdJet2BJet	1.204e-01	
5	Lep3Pt	1.158e-01	dEtaFwdJetClosestLep	1.177e-01	
6	maxEtaJet25	1.121e-01	minDRll	1.143e-01	
7	dEtaFwdJet2BJet	9.363e-02	dPhiHighestPtSSPair	9.777e-02	
8	nJetEta1	6.730e-02	nJet25_Recl	9.034e-02	
9	nJet25_Recl	6.178e-02	nJetEta1	4.749e-02	
10	lepCharge	4.701e-02	lepCharge	4.116e-02	

Table 5.10: TMVA input variables ranking for BDTA_GRAD method for the trainings in the three lepton channel. For both trainings the rankings show almost the same 5 variables in the first places.

```

TMVA.Types.kBDT
NTrees=800
BoostType=Grad
Shrinkage=0.10
!UseBaggedGrad
nCuts=50
MaxDepth=3
NegWeightTreatment=PairNegWeightsGlobal
CreateMVAPdfs

```

Table 5.11: TMVA configuration used in the BDT training.

1758 5.6 Additional discriminating variables

1759 Two additional discriminating variables were tested considering the fact that the
 1760 forward jet in the background could come from the pileup; since we have a real
 1761 forward jet in the signal, it could give some improvement in the discriminating power.
 1762 The additional variables describe the forward jet momentum (fwdJetPt25) and the
 1763 forward jet identification(fwdJetPUID). Distributions for these variables in the three
 1764 lepton channel are shown in the figure 5.8. The forward jet identification distribution
 1765 show that for both, signal and background, jets are mostly real jets.

1766 The testing was made including in the MVA input one variable at a time, so we

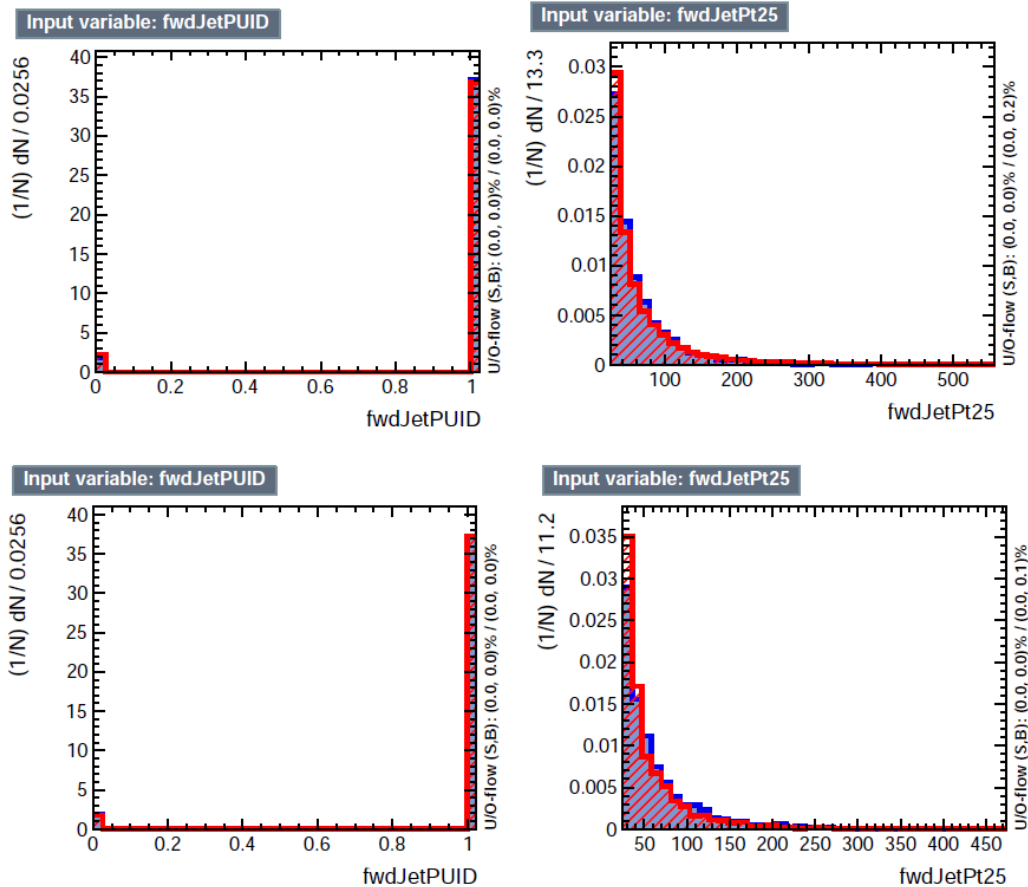


Figure 5.8: Additional discriminating variables distributions for ttV training (Top row) and tt training (bottom row) in the three lepton channel. The origin of the jets in the forward jet identification distribution is tagged as 0 for “pileup jets” while “real jets” are tagged as 1.

1767 can evaluate the discrimination power of each variable, and then both simultaneously.
 1768 `fwdJetPUID` was ranked in the last place in importance (11) in both training (ttV
 1769 and tt) while `fwdJetPt25` was ranked 3 in the ttV training and 7 in the tt training.
 1770 When training using 12 variables, `fwdJetPt25` was ranked 5 and 7 in the ttV and tt
 1771 trainings respectively, while `fwdJetPUID` was ranked 12 in both cases.

1772 The improvement in the discrimination performance provided by the additional
 1773 variables is about 1%, so it was decided not to include them in the procedure. Table
 1774 5.12 show the ROC-integral for all the testing cases we made.

ROC-integral	
base 10 var ttv	0.848
+ fwdJetPUID ttv	0.849
+ fwdJetPt25 ttv	0.856
12 var ttv	0.856
<hr/>	
base 10 var tt	0.777
+ fwdJetPUID tt	0.777
+ fwdJetPt25 tt	0.787
12 var	0.787

Table 5.12: ROC-integral for all the testing cases we made in the evaluation of the additional variables discriminating power. The improvement in the discrimination performance provided by the additional variables is about 1%

₁₇₇₅ **References**

- ₁₇₇₆ [1] J. Schwinger. "Quantum Electrodynamics. I. A Covariant Formulation". Physical Review. 74 (10): 1439-61, (1948).
- ₁₇₇₇
- ₁₇₇₈ [2] R. P. Feynman. "Space-Time Approach to Quantum Electrodynamics". Physical Review. 76 (6): 769-89, (1949).
- ₁₇₇₉
- ₁₇₈₀ [3] S. Tomonaga. "On a Relativistically Invariant Formulation of the Quantum Theory of Wave Fields". Progress of Theoretical Physics. 1 (2): 27-42, (1946).
- ₁₇₈₁
- ₁₇₈₂ [4] D.J. Griffiths, "Introduction to electrodynamics". 4th ed. Pearson, (2013).
- ₁₇₈₃ [5] F. Mandl, G. Shaw. "Quantum field theory." Chichester: Wiley (2009).
- ₁₇₈₄ [6] F. Halzen, and A.D. Martin, "Quarks and leptons: An introductory course in modern particle physics". New York: Wiley, (1984) .
- ₁₇₈₅
- ₁₇₈₆ [7] File: Standard_Model_of_Elementary_Particle_dark.svg. (2017, June 12) Wikimedia Commons, the free media repository. Retrieved November 27, 2017 from <https://www.collegiate-advanced-electricity.com/single-post/2017/04/10/The-Standard-Model-of-Particle-Physics>.
- ₁₇₈₇
- ₁₇₈₈
- ₁₇₈₉
- ₁₇₉₀ [8] E. Noether, "Invariante Variationsprobleme", Nachrichten von der Gesellschaft der Wissenschaften zu Göttingen, mathematisch-physikalische Klasse, vol. 1918, pp. 235-257, (1918).
- ₁₇₉₁
- ₁₇₉₂

- 1793 [9] C. Patrignani et al. (Particle Data Group), Chin. Phys. C, 40, 100001 (2016)
1794 and 2017 update.
- 1795 [10] M. Goldhaber, L. Grodzins, A.W. Sunyar “Helicity of Neutrinos”, Phys. Rev.
1796 109, 1015 (1958).
- 1797 [11] Palanque-Delabrouille N et al. “Neutrino masses and cosmology with Lyman-
1798 alpha forest power spectrum”, JCAP 11 011 (2015).
- 1799 [12] M. Gell-Mann. “A Schematic Model of Baryons and Mesons”. Physics Letters.
1800 8 (3): 214-215 (1964).
- 1801 [13] G. Zweig. “An SU(3) Model for Strong Interaction Symmetry and its Breaking”
1802 (PDF). CERN Report No.8182/TH.401 (1964).
- 1803 [14] G. Zweig. “An SU(3) Model for Strong Interaction Symmetry and its Breaking:
1804 II” (PDF). CERN Report No.8419/TH.412(1964).
- 1805 [15] M. Gell-Mann. “The Interpretation of the New Particles as Displaced Charged
1806 Multiplets”. Il Nuovo Cimento 4: 848. (1956).
- 1807 [16] T. Nakano, K, Nishijima. “Charge Independence for V-particles”. Progress of
1808 Theoretical Physics 10 (5): 581-582. (1953).
- 1809 [17] N. Cabibbo, “Unitary symmetry and leptonic decays” Physical Review Letters,
1810 vol. 10, no. 12, p. 531, (1963).
- 1811 [18] M.Kobayashi, T.Maskawa, “CP-violation in the renormalizable theory of weak
1812 interaction,” Progress of Theoretical Physics, vol. 49, no. 2, pp. 652-657, (1973).
- 1813 [19] File: Weak Decay (flipped).svg. (2017, June 12). Wikimedia Com-
1814 mons, the free media repository. Retrieved November 27, 2017 from

- 1815 https://commons.wikimedia.org/w/index.php?title=File:Weak_Decay_(flipped)
1816 .svg&oldid=247498592.
- 1817 [20] Georgia Tech University. Coupling Constants for the Fundamental
1818 Forces(2005). Retrieved January 10, 2018, from http://hyperphysics.phy-
1819 astr.gsu.edu/hbase/Forces/couple.html#c2
- 1820 [21] M. Strassler. (May 31, 2013).The Strengths of the Known Forces. Retrieved Jan-
1821 uary 10, 2018, from https://profmattstrassler.com/articles-and-posts/particle-
1822 physics-basics/the-known-forces-of-nature/the-strength-of-the-known-forces/
- 1823 [22] S.L. Glashow. “Partial symmetries of weak interactions”, Nucl. Phys. 22 579-
1824 588, (1961).
- 1825 [23] A. Salam, J.C. Ward. “Electromagnetic and weak interactions”, Physics Letters
1826 13 168-171, (1964).
- 1827 [24] S. Weinberg, “A model of leptons”, Physical Review Letters, vol. 19, no. 21, p.
1828 1264, (1967).
- 1829 [25] M. Peskin, D. Schroeder, “An introduction to quantum field theory”. Perseus
1830 Books Publishing L.L.C., (1995).
- 1831 [26] A. Pich. “The Standard Model of Electroweak Interactions”
1832 https://arxiv.org/abs/1201.0537
- 1833 [27] F.Bellaiche. (2012, 2 September). “What’s this Higgs boson anyway?”. Retrieved
1834 from: https://www.quantum-bits.org/?p=233
- 1835 [28] M. Endres et al. Nature 487, 454-458 (2012) doi:10.1038/nature11255

- 1836 [29] F. Englert, R. Brout. “Broken Symmetry and the Mass of Gauge
 1837 Vector Mesons”. Physical Review Letters. 13 (9): 321-23.(1964)
 1838 doi:10.1103/PhysRevLett.13.321
- 1839 [30] P.Higgs. “Broken Symmetries and the Masses of Gauge Bosons”. Physical Re-
 1840 view Letters. 13 (16): 508-509,(1964). doi:10.1103/PhysRevLett.13.508.
- 1841 [31] G.Guralnik, C.R. Hagen and T.W.B. Kibble. “Global Conservation Laws
 1842 and Massless Particles”. Physical Review Letters. 13 (20): 585-587, (1964).
 1843 doi:10.1103/PhysRevLett.13.585.
- 1844 [32] CMS collaboration. “Observation of a new boson at a mass of 125 GeV with
 1845 the CMS experiment at the LHC”. Physics Letters B. 716 (1): 30-61 (2012).
 1846 arXiv:1207.7235. doi:10.1016/j.physletb.2012.08.021
- 1847 [33] ATLAS collaboration. “Observation of a New Particle in the Search for the Stan-
 1848 dard Model Higgs Boson with the ATLAS Detector at the LHC”. Physics Letters
 1849 B. 716 (1): 1-29 (2012). arXiv:1207.7214. doi:10.1016/j.physletb.2012.08.020.
- 1850 [34] ATLAS collaboration; CMS collaboration (26 March 2015). “Combined Mea-
 1851 surement of the Higgs Boson Mass in pp Collisions at $\sqrt{s}=7$ and 8 TeV with
 1852 the ATLAS and CMS Experiments”. Physical Review Letters. 114 (19): 191803.
 1853 arXiv:1503.07589. doi:10.1103/PhysRevLett.114.191803.
- 1854 [35] LHC InternationalMasterclasses“When protons collide”. Retrieved from
 1855 http://atlas.physicsmasterclasses.org/en/zpath_protoncollisions.htm
- 1856 [36] CMS Collaboration, “SM Higgs Branching Ratios and To-
 1857 tal Decay Widths (up-date in CERN Report4 2016)”).

- 1858 https://twiki.cern.ch/twiki/bin/view/LHCPhysics/CERNYellowReportPageBR
 1859 , last accessed on 17.12.2017.
- 1860 [37] R.Grant V. “Determination of Higgs branching ratios in $H \rightarrow W^+W^- \rightarrow l\nu jj$ and $H \rightarrow ZZ \rightarrow l^+l^-jj$ channels”. Physics Department, University of Tennessee (Dated: October 31, 2012). Retrieved from http://aesop.phys.utk.edu/ph611/2012/projects/Riley.pdf
- 1864 [38] LHC Higgs Cross Section Working Group, Denner, A., Heinemeyer, S. et al.
 1865 “Standard model Higgs-boson branching ratios with uncertainties”. Eur. Phys.
 1866 J. C (2011) 71: 1753. <https://doi.org/10.1140/epjc/s10052-011-1753-8>
- 1867 [39] F. Maltoni, K. Paul, T. Stelzer, and S. Willenbrock, “Associated production
 1868 of Higgs and single top at hadron colliders”, Phys.Rev. D64 (2001) 094023,
 1869 [hep-ph/0106293].
- 1870 [40] S. Biswas, E. Gabrielli, F. Margaroli, and B. Mele, “Direct constraints on the
 1871 top-Higgs coupling from the 8 TeV LHC data,” Journal of High Energy Physics,
 1872 vol. 07, p. 073, (2013).
- 1873 [41] M. Farina, C. Grojean, F. Maltoni, E. Salvioni, and A. Thamm, “Lifting de-
 1874 generacies in Higgs couplings using single top production in association with a
 1875 Higgs boson,” Journal of High Energy Physics, vol. 05, p. 022, (2013).
- 1876 [42] T.M. Tait and C.-P. Yuan, “Single top quark production as a window to physics
 1877 beyond the standard model”, Phys. Rev. D 63 (2000) 014018 [hep-ph/0007298].
- 1878 [43] F. Demartin, F. Maltoni, K. Mawatari, and M. Zaro, “Higgs production in
 1879 association with a single top quark at the LHC,” European Physical Journal C,
 1880 vol. 75, p. 267, (2015).

- 1881 [44] CMS Collaboration, “Modelling of the single top-quark pro-
 1882 duction in association with the Higgs boson at 13 TeV.”
 1883 <https://twiki.cern.ch/twiki/bin/viewauth/CMS/SingleTopHiggsGeneration13TeV>,
 1884 last accessed on 16.01.2018.
- 1885 [45] CMS Collaboration, “SM Higgs production cross sections at $\sqrt{s} = 13$ TeV.”
 1886 <https://twiki.cern.ch/twiki/bin/view/LHCPhysics/CERNYellowReportPageAt13TeV>, last
 1887 accessed on 16.01.2018.
- 1888 [46] S. Dawson, The effective W approximation, Nucl. Phys. B 249 (1985) 42.
- 1889 [47] S. Biswas, E. Gabrielli and B. Mele, JHEP 1301 (2013) 088 [[arXiv:1211.0499](https://arxiv.org/abs/1211.0499)
 1890 [hep-ph]].
- 1891 [48] F. Demartin, B. Maier, F. Maltoni, K. Mawatari, and M. Zaro, “tWH associated
 1892 production at the LHC”, European Physical Journal C, vol. 77, p. 34, (2017).
 1893 [arXiv:1607.05862](https://arxiv.org/abs/1607.05862)
- 1894 [49] LHC Higgs Cross Section Working Group, “Handbook of LHC Higgs Cross
 1895 Sections: 4.Deciphering the Nature of the Higgs Sector”, [arXiv:1610.07922](https://arxiv.org/abs/1610.07922).
- 1896 [50] J. Ellis, D. S. Hwang, K. Sakurai, and M. Takeuchi.“Disentangling Higgs-Top
 1897 Couplings in Associated Production”, JHEP 1404 (2014) 004, [[arXiv:1312.5736](https://arxiv.org/abs/1312.5736)].
- 1898 [51] CMS Collaboration, V. Khachatryan et al., “Precise determination of the mass
 1899 of the Higgs boson and tests of compatibility of its couplings with the standard
 1900 model predictions using proton collisions at 7 and 8 TeV,” [arXiv:1412.8662](https://arxiv.org/abs/1412.8662).
- 1901 [52] ATLAS and CMS Collaborations, “Measurements of the Higgs boson produc-
 1902 tion and decay rates and constraints on its couplings from a combined ATLAS

- 1903 and CMS analysis of the LHC pp collision data at $sqrts = 7$ and 8 TeV,” (2016).
- 1904 CERN-EP-2016-100, ATLAS-HIGG-2015-07, CMS-HIG-15-002.
- 1905 [53] File:Cern-accelerator-complex.svg. Wikimedia Commons,
- 1906 the free media repository. Retrieved January, 2018 from
- 1907 <https://commons.wikimedia.org/wiki/File:Cern-accelerator-complex.svg>
- 1908 [54] J.L. Caron , “Layout of the LEP tunnel including future LHC infrastructures.”,
- 1909 (Nov, 1993). A C Collection. Legacy of AC. Pictures from 1992 to 2002. Re-
- 1910 trieval from <https://cds.cern.ch/record/841542>
- 1911 [55] M. Vretenar, “The radio-frequency quadrupole”. CERN Yellow Report CERN-
- 1912 2013-001, pp.207-223 DOI:10.5170/CERN-2013-001.207. arXiv:1303.6762
- 1913 [56] L.Evans. P. Bryant (editors). “LHC Machine”. JINST 3 S08001 (2008).
- 1914 [57] CERN Photographic Service.“Radio-frequency quadrupole, RFQ-1”, March
- 1915 1983, CERN-AC-8303511. Retrieved from <https://cds.cern.ch/record/615852>.
- 1916 [58] CERN Photographic Service “Animation of CERN’s accelerator net-
- 1917 work”, 14 October 2013. DOI: 10.17181/cds.1610170 Retrieved from
- 1918 <https://videos.cern.ch/record/1610170>
- 1919 [59] C.Sutton. “Particle accelerator”.Encyclopedia Britannica. July 17, 2013. Re-
- 1920 trieval from <https://www.britannica.com/technology/particle-accelerator>.
- 1921 [60] L.Guiraud. “Installation of LHC cavity in vacuum tank.”. July 27 2000. CERN-
- 1922 AC-0007016. Retrieved from <https://cds.cern.ch/record/41567>.
- 1923 [61] J.L. Caron, “Magnetic field induced by the LHC dipole’s superconducting coils”.
- 1924 March 1998. AC Collection. Legacy of AC. Pictures from 1992 to 2002. LHC-
- 1925 PHO-1998-325. Retrieved from <https://cds.cern.ch/record/841511>

- 1926 [62] AC Team. “Diagram of an LHC dipole magnet”. June 1999. CERN-DI-9906025
 1927 retrieved from <https://cds.cern.ch/record/40524>.
- 1928 [63] CMS Collaboration “Public CMS Luminosity Information”.
 1929 <https://twiki.cern.ch/twiki/bin/view/CMSPublic/LumiPublicResults#2016>
 1930 _proton_proton_13_TeV_collis, last accessed 24.01.2018
- 1931 [64] J.L Caron. “LHC Layout” AC Collection. Legacy of AC. Pictures
 1932 from 1992 to 2002. September 1997, LHC-PHO-1997-060. Retrieved from
 1933 <https://cds.cern.ch/record/841573>.
- 1934 [65] J.A. Coarasa. “The CMS Online Cluster: Setup, Operation and Maintenance
 1935 of an Evolving Cluster”. ISGC 2012, 26 February - 2 March 2012, Academia
 1936 Sinica, Taipei, Taiwan.
- 1937 [66] CMS Collaboration. “The CMS experiment at the CERN LHC” JINST 3 S08004
 1938 (2008).
- 1939 [67] CMS Collaboration. “CMS detector drawings 2012” CMS-PHO-GEN-2012-002.
 1940 Retrieved from <http://cds.cern.ch/record/1433717>.
- 1941 [68] R. Breedon. “View through the CMS detector during the cooldown of the
 1942 solenoid on February 2006. CMS Collection”, February 2006, CMS-PHO-
 1943 OREACH-2005-004, Retrieved from <https://cds.cern.ch/record/930094>.
- 1944 [69] A. Dominguez et. al. “CMS Technical Design Report for the Pixel Detector
 1945 Upgrade”, CERN-LHCC-2012-016. CMS-TDR-11.
- 1946 [70] CMS Collaboration. “Description and performance of track and primary-vertex
 1947 reconstruction with the CMS tracker,” Journal of Instrumentation, vol. 9, no.
 1948 10, p. P10009,(2014).

- 1949 [71] CMS Collaboration and M. Brice. “Images of the CMS Tracker Inner
 1950 Barrel”, November 2008, CMS-PHO-TRACKER-2008-002. Retrieved from
 1951 <https://cds.cern.ch/record/1431467>.
- 1952 [72] M. Weber. “The CMS tracker”. 6th international conference on hyperons, charm
 1953 and beauty hadrons Chicago, June 28-July 3 2004.
- 1954 [73] CMS Collaboration. “Projected Performance of an Upgraded CMS Detector at
 1955 the LHC and HL-LHC: Contribution to the Snowmass Process”. Jul 26, 2013.
 1956 arXiv:1307.7135
- 1957 [74] L. Veillet. “End assembly of HB with EB rails and rotation in-
 1958 side SX ”,January 2002. CMS-PHO-HCAL-2002-002. Retrieved from
 1959 <https://cds.cern.ch/record/42594>.
- 1960 [75] J. Puerta-Pelayo.“First DT+RPC chambers installation round in the
 1961 UX5 cavern.”. January 2007, CMS-PHO-OREACH-2007-001. Retrieved from
 1962 <https://cds.cern.ch/record/1019185>
- 1963 [76] X. Cid Vidal and R. Cid Manzano. “CMS Global Muon Trigger” web
 1964 site: Taking a closer look at LHC. Retrieved from https://www.lhc-closer.es/taking_a_closer_look_at_lhc/0.lhc_trigger
 1965
- 1966 [77] WLCG Project Office, “Documents & Reference - Tiers - Structure,” (2014).
 1967 <http://wlcg.web.cern.ch/documents-reference> , last accessed on 30.01.2018.
- 1968 [78] CMS Collaboration. “CMSSW Application Framework”,
 1969 <https://twiki.cern.ch/twiki/bin/view/CMSPublic/WorkBookCMSSWFFramework>,
 1970 last accesses 06.02.2018

- 1971 [79] A. Buckleya, J. Butterworthb, S. Giesekec, et. al. “General-purpose event gen-
1972 erators for LHC physics”. arXiv:1101.2599v1 [hep-ph] 13 Jan 2011
- 1973 [80] A. Quadt. “Top Quark Physics at Hadron Colliders”. Advances in the Physics
1974 of Particles and Nuclei. Springer-Verlag Berlin Heidelberg. DOI: 10.1007/978-
1975 3-540-71060-8 (2007)
- 1976 [81] DurhamHep Data Project, “The Durham HepData Project - PDF Plotter.”
1977 <http://hepdata.cedar.ac.uk/pdf/pdf3.html> , last accessed on 02.02.2018.
- 1978 [82] F. Maltoni, G. Ridolfi, and M. Ubiali, “b-initiated processes at the LHC: a
1979 reappraisal,” Journal of High Energy Physics, vol. 07, p. 022, (2012).
- 1980 [83] B. Andersson, G. Gustafson, G. Ingelman and T. Sjostrand, “Parton fragmen-
1981 tation and string dynamics”, Physics Reports, Vol. 97, No. 2-3, pp. 31-145,
1982 1983.
- 1983 [84] CMS Collaboration, “Event generator tunes obtained from underlying event
1984 and multiparton scattering measurements;” European Physical Journal C, vol.
1985 76, no. 3, p. 155, (2016).
- 1986 [85] J. Alwall et. al., “The automated computation of tree-level and next-to-leading
1987 order differential cross sections, and their matching to parton shower simula-
1988 tions,” Journal of High Energy Physics, vol. 07, p. 079, (2014).
- 1989 [86] S. Frixione, P. Nason, and C. Oleari, “Matching NLO QCD computations with
1990 Parton Shower simulations: the POWHEG method,” Journal of High Energy
1991 Physics, vol. 11, p. 070, (2007).
- 1992 [87] S. Agostinelli et al., “GEANT4: A Simulation toolkit,” Nuclear Instruments
1993 and Methods in Physics, vol. A506, pp. 250–303, (2003).

- 1994 [88] J.Allison et.al.,“Recent developments in Geant4”, Nuclear Instruments and
1995 Methods in Physics Research A 835 (2016) 186-225.
- 1996 [89] CMS Collaboration “Full Simulation Offline Guide”,
1997 <https://twiki.cern.ch/twiki/bin/view/CMSPublic/SWGuideSimulation>, last
1998 accessed 04.02.2018
- 1999 [90] A. Giammanco. “The Fast Simulation of the CMS Experiment” J. Phys.: Conf.
2000 Ser. 513 022012 (2014)
- 2001 [91] CMS Collaboration, “Search for the associated production of a Higgs boson
2002 with a single top quark in proton-proton collisions at $\sqrt{s} = 8$ TeV”, JHEP 06
2003 (2016) 177,doi:10.1007/JHEP06(2016)177, arXiv:1509.08159.
- 2004 [92] B. Stieger, C. Jorda Lope et al., “Search for Associated Production of a Single
2005 Top Quark and a Higgs Boson in Leptonic Channels”, CMS Analysis Note CMS
2006 AN-14-140, 2014.
- 2007 [93] M. Peruzzi, C. Mueller, B. Stieger et al., “Search for ttH in multilepton final
2008 states at $\sqrt{s} = 13$ TeV”, CMS Analysis Note CMS AN-16-211, 2016.
- 2009 [94] CMS Collaboration, “Search for H to bbar in association with a single top quark
2010 as a test of Higgs boson couplings at $\sqrt{s} = 13$ TeV”, CMS Physics Analysis
2011 Summary CMS-PAS-HIG-16-019, 2016.
- 2012 [95] B. Maier, “SingleTopHiggProduction13TeV”, February, 2016.
2013 <https://twiki.cern.ch/twiki/bin/viewauth/CMS/SingleTopHiggsGeneration13TeV>.
- 2014 [96] M. Peruzzi, F. Romeo, B. Stieger et al., “Search for ttH in multilepton final1
2015 states at $\sqrt{s} = 13$ TeV”, CMS Analysis Note CMS AN-17-029, 2017.

2016 [97] B. WG, “BtagRecommendation80XReReco”, February, 2017.
2017 <https://twiki.cern.ch/twiki/bin/view/CMS/BtagRecommendation80XReReco>.